UNIVERSITÀ DI PARMA

UNIVERSITÀ DEGLI STUDI DI PARMA

DOTTORATO DI RICERCA IN

Scienze e Tecnologie dei Materiali

CICLO XXXVII

Magnetic Heusler and High Entropy Alloys for magnetic refrigeration and low-grade heat harvesting

COORDINATORE:

Chiar.mo Prof. Enrico Dal Canale

TUTORE:

Dott.ssa Franca Albertini

Dott. Simone Fabbrici

Dottorando: Lorenzo Gallo

Anni Accademici 2021/2022 – 2023/2024

"Svakoga dana u svakom pogledu

sve više napredujem"

Do you remember Dolly Bell?
E. Kusturica (1981)

1 Abstract

Energy plays a fundamental role in modern society, significantly impacting daily activities. Moreover, the increasing demand for energy, driven by new technologies, contributes to a profound impact on the environment and society. The high energy consumption becomes even more concerning considering that over 70% of the energy is lost during the transformation processes required to convert primary energy carriers into energy services. Furthermore, most energy losses occur in the form of heat emitted at temperatures below 100°C. The necessity for more efficient energy conversion solutions and the exploration of methods to recover waste energy is becoming increasingly crucial for the scientific community.

Two promising fields within materials science addressing this challenge are magnetic refrigeration, which focuses on the development of more energy-efficient cooling technologies (magnetocaloric applications), and waste low-grade heat recovery (thermomagnetic applications).

This thesis aims to contribute to address these issues by synthesizing NiMn-based Heusler alloys and High Entropy Alloys, composed of elements considered environmentally and economically non-critical. The magnetic transitions in the synthesized alloys are all second-order, ensuring full reversibility of the phenomena under investigation.

The first part of the work focuses on the synthesis and magnetic characterization of various NiMnSn-based Heusler alloys, examining how the most relevant magnetic characteristics for magnetocaloric and thermomagnetic applications vary with changes in alloy composition. This analysis demonstrates the optimal applicability of NiMnSn-based Heusler alloys, as their Curie transitions cover a temperature range between 300 K and 350 K.

Additionally, the thesis presents the development and application of a thermomagnetic device that converts controlled heat into easily measurable mechanical energy, enabling comprehensive thermomagnetic analysis of the materials under operando conditions for the first time. This device was initially employed to test the thermomagnetic properties of three representative Heusler alloys: NiMnSn, NiMnIn, and NiMnCuGa. The results demonstrated, firstly, the potential of the thermomagnetic motor prototype as an effective testing platform for thermomagnetic generation designs, as well as the promise of NiMn-based second-order Heusler compounds for low-grade heat energy harvesting applications.

Notably, the NiMnIn alloy could generate an electric power of 2.6 W/kg (20.4 mW/cm^3), which significantly exceeds the power generated by other devices presented in the literature.

Subsequently, 3D-printed additive manufacturing rotors based on NiMnSn and NiMnIn with varying thicknesses were developed to evaluate their thermomagnetic properties. A straightforward composite filament production method enabled uniform dispersion of magnetic powders within a polymer matrix, allowing for the fabrication of rotors with different thicknesses. The findings indicated that an increased rotor surface-to-volume ratio correlated with higher power peaks, confirming previous observations. Notably, the power peak curves of the 3D-printed rotors exhibited a sharp peak near the alloy's transition temperature, reflecting a temperature dependence that aligned with simulated trends. The study underscored a promising relationship between rotor geometry and thermomagnetic performance.

Finally, two new high-entropy alloys, FeNiGaMnSi-based, were synthesized. Magnetic characterizations identified two second-order magnetic transitions near room temperature for both compositions, indicating the alloys' suitability for potential magnetocaloric and thermomagnetic applications. The magnetic entropy changes and the magnetic work generated in an ideal thermomagnetic cycle (W_m) were calculated for both alloys. The $\mathbf{\Delta S}$ values were comparable to the highest reported values for rare-earth-free HEAs across the Curie transition, demonstrating strong magnetocaloric application potential for these synthesized HEAs. Additionally, the calculated W_m values were similar to those obtained for NiMn-based Heuslers, further suggesting promise for TM applications. Characterizations performed with the TM device confirmed these findings, showing for the first time that the synthesized HEAs are promising candidates for waste energy recovery, which enhances interest in this novel class of functional materials.

In conclusion, this work aims to present new and effective solutions for magnetic energy conversion applications, starting with the synthesis of functional materials with magnetic properties that can be easily tuned and concluding with the evaluation of their performance under operational conditions. This approach addresses the existing gap between the functional study of magnetic alloys and their practical applications.

The work has been carried out primarily at the Institute of Materials for Electronics and Magnetism of the National Research Council (IMEM-CNR), where all the activity on synthesis and fundamental characterization of the thermomagnetic

materials has been realized. Thanks to the strong collaboration with the Department of Physics of the University of Parma it has been possible to characterize the magnetic properties of the materials produced, and to test their functional behaviour and application potential in a thermomagnetic prototype developed there. A stage at the University of Sevilla, Spain, allowed for the realization of composite filaments containing the thermomagnetic materials and their use for 3D printing thermomagnetic rotors that were tested in the prototype.

CONTENTS

2 Introduction and motivations

Energy is the cornerstone of modern society, permeating every aspect of our daily lives and driving economic growth, technological advancement, and overall quality of life. From the electricity that powers our homes and industries to the fuel that propels our transportation systems, energy is fundamental to the functioning of contemporary civilization. As the global population continues to grow and urbanize, the demand for energy is escalating, placing unprecedented strain on our resources and infrastructure[1], [2].

Energy is integral to nearly all human activities, providing the power necessary for basic needs such as heating, cooling, lighting, and cooking, as well as for more complex industrial processes and technological applications. It is essential for the operation of hospitals, schools, and businesses, and is a key enabler of economic productivity and growth. The reliable and affordable supply of energy is a prerequisite for social and economic development, and disparities in energy access are closely linked to inequalities in income, health, and education.

The relationship between energy consumption and economic development is well-documented [3]. Historically, periods of significant economic growth have been accompanied by increases in energy use, as industries expand, and new technologies emerge. Energy is a vital input for industrial production, transportation, and commerce, and its availability directly impacts the competitiveness of economies. Developing countries, in particular, face a dual challenge: they must increase their energy consumption to achieve economic development while also managing the environmental impacts of this increased energy use.

Technological innovation is both a driver and a consequence of energy use. Advances in energy technology, such as the development of more efficient engines, renewable energy sources, and smart grid systems, have the potential to significantly reduce energy consumption and greenhouse gas emissions [4]. Conversely, new technologies often require substantial amounts of energy to develop, manufacture, and operate. The pursuit of cleaner, more efficient energy technologies is therefore critical to achieving a sustainable energy future.

The extraction, production, and consumption of energy have profound environmental and social impacts. Fossil fuels, which currently dominate the global energy mix, are a major source of air and water pollution, habitat destruction, and climate change. The burning of coal, oil, and natural gas releases large quantities of

carbon dioxide and other greenhouse gases, contributing to global warming and climate-related disasters. Moreover, energy infrastructure projects can lead to the displacement of communities, loss of biodiversity, and other social issues [5].

Transitioning to renewable energy sources such as solar, wind, and hydroelectric power can mitigate many of these negative impacts. However, the transition itself poses challenges, including the need for significant investment, technological innovation, and policy support. Ensuring a just and equitable transition is crucial to avoid exacerbating existing social inequalities [6].

The urgent need for sustainable energy solutions is perhaps the most compelling motivation for this research. Sustainable energy systems are those that meet the needs of the present without compromising the ability of future generations to meet their own needs [7]. This involves balancing economic, environmental, and social objectives, and requires a multifaceted approach that includes policy measures, technological innovation, and changes in consumer behavior [8].

A major issue in our current energy systems is the inefficiency and associated waste. In 2016, C. Forman et al. estimated the amount of energy lost during the various stages of energy conversion, starting from different primary energy sources (such as oil, coal, nuclear, etc.) and calculating the losses observed across different applications (including transportation, industrial, residential, and commercial sectors). The ratio of lost energy to energy effectively utilized in service well highlights the significant issue of energy loss, with approximately 72% of primary energy being rejected [9].

The situation worsens when analysing electricity generation alone: a study by the U.S. Energy Information Administration (EIA) revealed that approximately 80% of the primary energy carriers used for electricity generation is lost as heat [10]. In this amount of wasted energy industries contribute about 44%, commercial and residential about 36% and transportation 20% [11]. The inefficiency is particularly pronounced in older coal-fired power plants where losses necessitate the burning of more fuel to meet energy demands, thus amplifying the environmental footprint. Innovations in combined heat and power systems, which capture and utilize waste heat, can significantly improve efficiency and reduce emissions.

When discussing waste heat, defined as energy lost during conversion processes in the form of heat, it's important to consider the temperature at which this heat is emitted. Waste heat can be classified into three categories based on temperature: high-grade heat ($T > 300°C$), medium-grade heat ($100°C < T < 300°C$), and low-grade

heat (T < 100°C). These categories account for approximately 21%, 16%, and 63% of the total waste heat typically generated annually in energy conversion processes, respectively [9]. Understanding this classification is essential for devising strategies and developing technologies to effectively recover significant portions of waste heat across these different temperature ranges. For example, one promising solution to address the issue of wasted energy in the form of low-grade heat is thermomagnetic applications.

Thermomagnetic materials can convert thermal energy into a more usable form of energy (such as mechanical or electrical). The conversion process is carried out through a thermodynamic cycle consisting of two transformations at a constant applied magnetic field and two transformations at a constant temperature. This specific cycle is known as the thermomagnetic cycle and will be examined in greater detail in Section 3.2.1.

This application has several notable features, among which the most important is its effectiveness even with a small temperature gradient, making it particularly well-suited for low-grade heat recovery. Moreover, the energy recovery process occurs without any emissions, making it an entirely green solution in terms of environmental impact. Generally, this technology has the potential to harness waste heat from industrial processes and power generation, converting it into usable electricity and thereby improving overall energy efficiency [12].

The problem is further compounded by the energy demands of cooling systems, which are critical for maintaining comfortable living conditions, preserving food and medicine, and ensuring the optimal operation of electronic devices and industrial processes. Cooling systems, especially air conditioners and refrigerators, are significant energy consumers. As global temperatures rise and living standards improve, the demand for cooling is expected to surge, leading to a paradoxical increase in energy consumption and greenhouse gas emissions.

Global cooling energy demand is projected to increase by 150% by 2050, driven largely by rising temperatures and economic growth in developing countries [13]. Air conditioning, while vital for health and comfort, poses a major challenge due to its high energy consumption and the greenhouse gases emitted by some refrigerants. Moreover, urban heat islands (UHIs), where urban areas experience higher temperatures than their rural surroundings due to human activities and the concentration of heat-absorbing materials, exacerbate the cooling challenge. UHIs increase the demand for air conditioning, further straining energy resources and

infrastructure [14]. To address this, the development of more energy-efficient cooling technologies, such as magnetocaloric refrigeration, is essential.

Magnetocaloric materials exhibit a temperature change when exposed to a changing magnetic field, enabling efficient refrigeration cycles without the need for traditional refrigerants [15]. This technology promises significant reductions in energy consumption and CO_2 emissions for small-scale cooling applications, making it a highly attractive solution in the context of rising global temperatures and increasing energy demands [16].

This dual challenge of reducing energy waste and managing the growing energy demands of cooling systems underscores the need for innovative solutions. Advances in thermomagnetic and magnetocaloric technologies can play a vital role. Thermomagnetic materials, for instance, can convert waste heat into electricity, providing a potential means to recover energy lost during industrial processes and power generation. Research into magnetocaloric materials also offers promising pathways for reducing energy consumption in cooling applications [17], [18].

In this context, the importance of materials science cannot be overstated. The field of materials science is pivotal in the discovery and development of new magnetic materials that can be utilized in thermomagnetic and magnetocaloric applications. These advanced materials are key to improving the efficiency and effectiveness of energy conversion and cooling technologies.

Thermomagnetic and magnetocaloric materials require specific magnetic and thermal properties to function effectively. For thermomagnetic applications, materials must exhibit a strong thermomagnetic effect, where a temperature gradient in the presence of a magnetic field induces an electrical current. This requires materials with high values of magnetic moment change across their magnetic transition. Advanced materials, such as Heusler, LaFe-based or MnFe-based alloys, are being explored for their promising thermomagnetic properties [19], [17].

Similarly, magnetocaloric materials need to have a significant magnetocaloric effect, which involves a reversible temperature change when subjected to a changing magnetic field. This effect is typically pronounced near the material's magnetic phase transition temperature. Researchers are investigating materials such as gadolinium and its alloys, which exhibit large magnetocaloric effects near room temperature. However, Gd is less economically competitive due to its high cost, the requirement for ultra-pure material, and its tendency to oxidize. In this case as well,

the scientific community is exploring new compositions such as LaFe-based, MnFe-based, and Heusler alloys. However, none of these currently achieve the same level of temperature change in the system to be cooled as Gd [20], [21].

Scientific collaboration is crucial for the synthesis of new magnetic materials, as it brings together diverse expertise, resources, and perspectives, accelerating innovation and enabling the discovery of advanced materials with enhanced properties. Furthermore, collaboration between materials scientists, physicists, and engineers is essential to translate these discoveries into practical technologies. Interdisciplinary research efforts are fostering the development of prototypes and pilot systems that utilize advanced magnetic materials for energy conversion and cooling. These collaborative projects are paving the way for the commercialization of efficient thermomagnetic and magnetocaloric devices, which have the potential to revolutionize energy management and cooling solutions.

The advancement of thermomagnetic and magnetocaloric technologies relies on the discovery and development of new magnetic materials. Materials science is essential in this effort, offering the expertise and tools to engineer materials with the necessary properties for efficient energy conversion and cooling. Investment in materials research and the promotion of interdisciplinary collaboration are crucial for driving innovation in energy technologies, ultimately contributing to a sustainable and resilient energy future.

The development of materials for magnetic refrigeration and thermomagnetic energy recovery, though promising, encounters several significant challenges that impede their widespread application. A primary concern is the efficiency of magnetocaloric materials in generating sufficient temperature changes for practical use. As mentioned previously, Gd remains one of the most effective materials, but its high cost and the need for ultra-pure forms limit broader adoption. Alternative materials, such as LaFe-based and MnFe-based, offer potential, yet they still fall short of Gd in terms of thermal performance. Additionally, these materials often suffer from chemical instability, with many prone to oxidation and degradation over time, leading to diminished efficiency and operational lifespan. This highlights the need for more durable materials.

Moreover, the environmental impact and sustainability of producing and utilizing these materials present additional concerns. The dependence on critical resources or environmentally harmful production methods could affect the long-term viability of magnetocaloric and thermomagnetic technologies. Therefore, it is essential to

pursue solutions that minimize environmental impact while maintaining the effectiveness of these applications.

Compounding these issues are the challenges associated with leveraging the magnetocaloric effect during first-order magnetic transitions. While first-order transitions can yield large entropy changes and substantial temperature shifts, they are frequently accompanied by hysteresis, phase coexistence, and latent heat effects. These phenomena, as will be explained later (Section 3), can reduce the reversibility and overall efficiency of the process, complicating the practical application of such materials in both magnetic refrigeration and thermomagnetic energy recovery systems.

Finally, the figures of merit typically used to evaluate thermomagnetic materials often prove inconclusive and fail to accurately reflect their true thermomagnetic properties. This inadequacy underscores the necessity for more precise and representative metrics to assess material performance under real-world conditions.

This thesis aims to contribute to solving the outlined issues by synthesizing NiMn-based Heusler and high-entropy alloys, both composed of elements deemed environmentally and economically non-critical. The magnetic transitions in the synthesized alloys are all second-order, ensuring full reversibility of the phenomena under investigation. Additionally, the thesis presents the development and application of a thermomagnetic device that converts controlled heat into easily measurable energy (mechanical or electrical). This device enables a comprehensive thermomagnetic analysis of the materials under operating conditions for the first time.

3 Fundamentals

3.1 MagnetoCaloric Effect (MCE)

The Magnetocaloric Effect (MCE), first discovered by Weiss and Picard in [22], is a phenomenon that belongs to all magnetic materials. This effect appears as either a change in entropy (ΔS_T) or a change in temperature (ΔT_{ad}) of a magnetic material in response to a variation in the applied magnetic field, under isothermal or adiabatic conditions, respectively [23]. These two physical quantities describe the magnetocaloric effect and, considering a variation in the magnetic field $\Delta H = H_2 - H_1$, are defined as follows:

$$\Delta S_T(T, \Delta H) = S(T, H_2) - S(T, H_1) \qquad (3.1)$$

$$\Delta T_{ad}(S, \Delta H) = T(S, H_2) - T(S, H_1) \qquad (3.2)$$

From a phenomenological perspective, and focusing on the second equation, it is observed that applying or removing a magnetic field to a magnetic material adiabatically induces a change in the system's temperature. This phenomenon can be exploited within a thermodynamic cycle to achieve controlled variations in a system. This specific cycle is referred to as the magnetocaloric cycle.

3.1.1 Magnetocaloric Cycle

In a typical magnetic refrigeration cycle, illustrated in figure 3-1, a magnetic material can be analysed as comprising two subsystems: the magnetic moments and the lattice. Without an external magnetic field applied, the magnetic moments exhibit fluctuating orientations while the lattice undergoes temperature-dependent vibrations. Upon application of an external magnetic field (I), the magnetic moments align parallel to it, leading to a reduction in entropy within the magnetic subsystem. Adiabatic magnetization results in a compensatory increase in lattice entropy, thereby elevating the sample temperature. Subsequently, a heat transfer fluid can be utilized to restore the magnetic material to its initial temperature (II). Adiabatic demagnetization reverses the process, enhancing the magnetic entropy of the sample and consequently reducing its lattice entropy and temperature (III). Temperature is then restored by passing a heat transfer fluid through the material (IV). By cyclically executing these four steps, a magnetic refrigerator can be constructed [24].

The MCE can be correlated with the magnetic moment of the magnetic material under consideration by employing the following Maxwell relation [25]:

$$\left(\frac{\partial S(T,H)}{\partial H}\right)_T = \left(\frac{\partial M(T,H)}{\partial T}\right)_H \qquad (3.3)$$

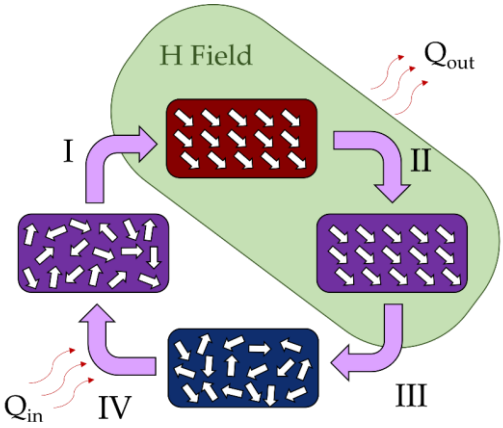

***Figure 3-1**: Conceptual scheme of the magnetocaloric cycle. The magnetocaloric material is subjected to an adiabatic change in magnetic field, resulting in a change in its temperature. The red rectangles represent the material at the T_{hot} temperature, the blue rectangles at the T_{cold} temperature and the purple rectangles at a temperature $T_{cold} < T < T_{hot}$. The green region represents the presence of an applied magnetic field H. Each thermodynamical transformation is enumerated in roman numbers and represented as purple arrows.*

In isothermal conditions and integrating between H_1 and H_2 the relation between the magnetic entropy changes and the magnetic moment is obtained:

$$\Delta S_T(T, \Delta H) = \int_{H_1}^{H_2} \left(\frac{\partial M(T,H)}{\partial T}\right)_H \qquad (3.4)$$

Equation (3.4) demonstrates that the change in magnetic entropy is directly proportional to the derivative of magnetic moment with respect to temperature at a constant magnetic field, as well as to the change in the magnetic field. By integrating Equation (3.3) with the corresponding TdS equation, it can be easily shown that the adiabatic temperature increase for a reversible adiabatic-isobaric process is equal to

$$\Delta T_{ad}(T, \Delta H) = -\int_{H_1}^{H_2} \left(\frac{T}{C(T,H)}\right)_H \left(\frac{\partial M(T,H)}{\partial T}\right)_H dH. \qquad (3.5)$$

The ΔT_{ad} is linked to ΔS_T but its values are determined by the specific heat C(T,H) and the transition temperature, as illustrated by the following approximate relation:

$$\Delta T_{ad}(T, \Delta H) \cong -\frac{T}{C(T,H)} \Delta S_T(T, \Delta H). \qquad (3.6)$$

By examining equations 3.4, and 3.5, it is evident that a significant MCE will occur at temperatures where the first-order temperature derivative of magnetic moment

is higher, and the heat capacity is highly affected by the magnetic field. This typically takes place near magnetic phase transitions.

In Figures 3-2 the temperature-dependent changes in magnetization (a) and magnetic entropy (b) of a magnetic material around an ideal Curie transition between the ferromagnetic and paramagnetic states are schematized. Both magnetic moment and entropy change smoothly at the transition temperature. Applying a magnetic field raises the magnetic moment at the transition point and reduces the entropy, with the largest change in entropy (ΔS_T) occurring at the Curie temperature (T_C). When the increase of the external magnetic field outcomes with the heating up of the material ($\Delta T_{ad} > 0$) and the decrease of the magnetic entropy ($\Delta S_T < 0$), if the change of magnetic fields occurs adiabatically and isothermally respectively, the MCE is classified as direct.

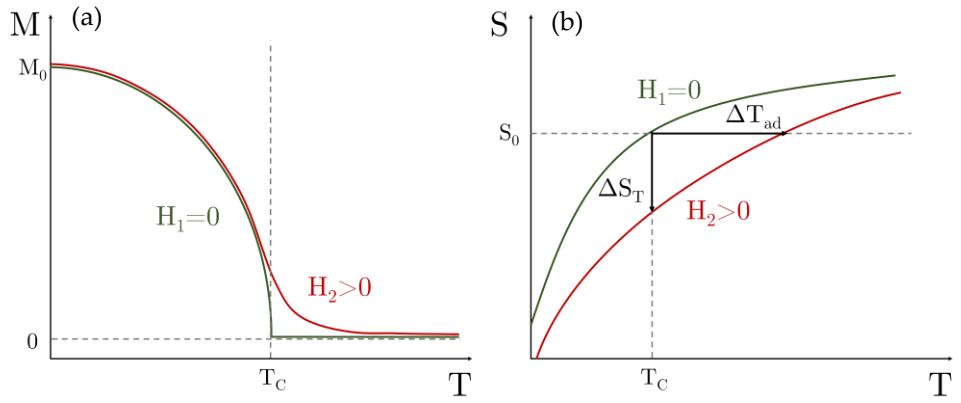

***Figure 3-2**: Schematic of MCE during a second-order phase transition. (a) Magnetization as a function of temperature, shown with (pink line) and without (green line) an applied magnetic field. (b) The associated entropy behavior. The MCE is illustrated by black arrows, indicating the adiabatic temperature change (ΔT_{ad}, horizontal) and the isothermal entropy change (ΔS_T, vertical).*

A significant MCE can also occur near first-order magnetic transitions. This scenario is illustrated in Figures 3-3. The magnetic moment and entropy curves exhibit a jump discontinuity, indicating the nature of the transition. When a magnetic field (H_2) is applied, it adds to the total energy and favors the phase with higher magnetization, resulting in a shift of the transition temperature (T_t from T_1 to T_2). This shift has a positive rate with the magnetic field ($dT_t/dH > 0$, Figure 3-3 (a) and 3-3.(b)) if the low-temperature phase has higher magnetization than the high-temperature phase

and also in this case the MCE is labelled as direct; otherwise, the rate is negative ($dT_t/dH < 0$, Figure 3-3 (c) and 3-3 (d)) and the MCE is considered inverse.

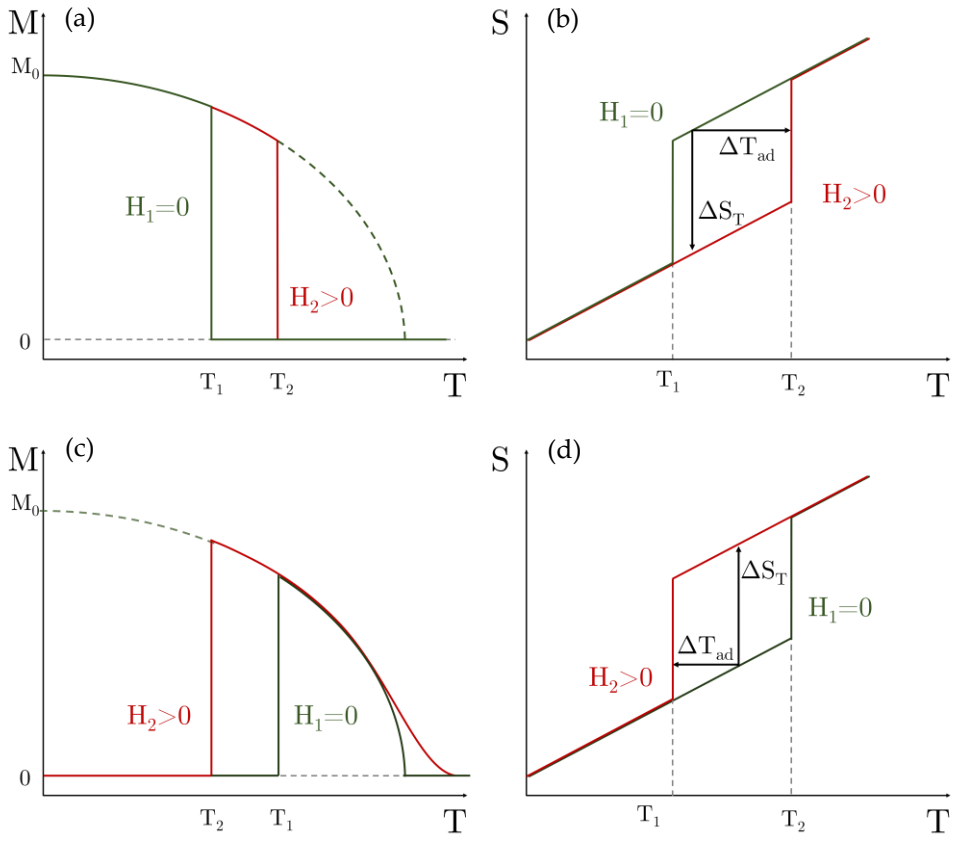

***Figure 3-3**: Schematic of the MCE during a conventional (a and b) and inverse (b and c) first-order transition. (a-c) Temperature-dependent magnetization with (red line) and without (green line) an applied magnetic field. (b-d) The corresponding entropy behavior. The MCE is indicated by black arrows.*

When the transition is induced by a magnetic field within the temperature range between T_1 and T_2, either an isothermal entropy change or an adiabatic temperature change occurs. In both scenarios, the total entropy change is composed of two parts: the enthalpy of the phase transformation and the magnetic entropy change due to the alignment of magnetic moments with the field [26]. When the enthalpy term,

derived from the latent heat of transformation (L), dominates, the entropy change can be approximated as $\Delta S_T \approx L/T_t$ [27], [23].

Using the magnetic Clausius-Clapeyron equation $\mu_0\, dH/dT = -\Delta S_T/\Delta M$, the entropy change for a complete phase transformation can be related to the magnetization difference between the two phases (ΔM) [28].

$$\Delta S_T = -\mu_0 \frac{dH}{dT} \Delta M \qquad (3.7)$$

Regarding ΔT_{ad} across a complete phase transformation, it can be obtained from eq. 3.6 and 3.7:

$$\Delta T_{ad} \cong \mu_0 \frac{T}{C(T,H)} \frac{\partial H}{\partial T} \Delta M \qquad (3.8)$$

ΔS_T and ΔT_{ad} seen during first-order transitions are often significantly larger than those observed during second-order transitions. This is due to the abrupt alteration in the magnetization and the addition of latent heat. However, these changes are limited to a narrow temperature range between T_1 and T_2. Additionally, the inherent irreversibility of first-order transitions influences the reversibility of the magnetocaloric effect (MCE) when a magnetic field is applied repeatedly [29].

The transition during a heating process and during a cooling process is separated by a hysteresis (Fig. 3-4). This hysteresis is defined as $\Delta T_{hyst} = T_{t\,h} - T_{t\,c}$, where $T_{t\,h}$ and $T_{t\,c}$ are the transition temperatures during heating and cooling, respectively. Similarly, the magnetic field hysteresis is defined as $\Delta H_{hyst} = H_{t\,c} - H_{t\,h}$, where $H_{t\,c}$ and $H_{t\,h}$ are the magnetic field values that trigger the transitions.

Generally, the thermal hysteresis is proportional to the field hysteresis and the coefficient of proportionality describe the shift of the transition temperature varying the external magnetic field:

$$\Delta T_{Hyst} = \frac{dT_t}{dH} \Delta H_{Hyst} \qquad (3.9)$$

The irreversible nature of a first order magnetic transition drastically affects the cyclability of the system and makes the thermal hysteresis the primary barrier to the efficient use of materials that undergoe on first-order transitions in magnetic cooling devices.

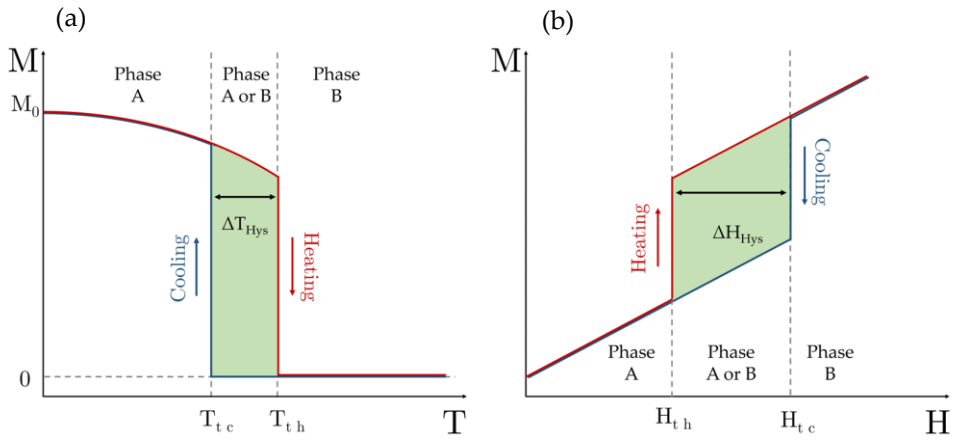

***Figure 3-4**: Schematic of the thermal (a) and magnetic (b) hysteresis across a first-order transition between the phase A and B.*

3.1.2 Magnetocaloric Materials

Magnetocaloric materials are the core of magnetic refrigeration, serving as the active element analogous to refrigerant gas in traditional systems. Effective magnetic refrigerators require materials with a high MCE near room temperature [30]. However, high adiabatic temperature change and entropy change alone do not guarantee efficiency or power. The MCE must be highly reversible, as hysteresis, often seen in first-order transitions, can significantly reduce efficiency. For optimal performance, ΔT_{ad} and ΔS_T should remain high across the entire operating temperature range, achievable through second-order transitions or layered regenerators with varied transition temperatures. Additionally, thermal conductivity and diffusivity are critical, as efficient heat transfer is necessary for high-frequency magnetocaloric (and thermomagnetic) cycles.

In commercial production, factors such as material abundance, cost, and manufacturing properties are crucial, alongside mechanical stability to avoid degradation over the refrigerator's lifecycle. Now, let's briefly explore the most promising MC materials for room-temperature refrigeration.

The MCE was first studied near second-order transitions in ferromagnetic materials, with gadolinium being the first used in a room-temperature magnetic refrigeration prototype due to its Curie transition at around 294 K [31]. Gadolinium exhibits a significant MCE (ΔT_{ad} = 3.3 K and ΔS_T= 3.1 $Jkg^{-1}K^{-1}$ for a polycrystalline sample in a $\mu_0\Delta H$ of 1 T [32]) over a broad temperature range near its Curie point, attributed to its high magnetic moment from 4f electrons (Ms = 7.5 μB per atom). Despite being widely used in prototypes and considered a benchmark for room-temperature MC materials, gadolinium's criticality and the need for high purity limit its marketability.

The cubic $LaFe_{13-x}Si_x$ ($x < 2.5$) compound exhibits a magnetic transition that shifts from a weak first-order magneto-elastic transition at low Si content ($Si \leq 1.6$) to a second-order transition [33]. The first-order transition involves a significant volume change without altering structural symmetry and has minimal intrinsic hysteresis with a large MCE observed with the field-induced transition [34]. Adding interstitial H or partially substituting Al, Co, or Mn alters the transition temperature, the transition order, and MCE intensity. H insertion expands the crystalline lattice, modifies the electronic structure, and raises the critical temperature while preserving the weak first-order transition [33], [35]. High MCE values, low hysteresis, and the abundance and low cost of constituent elements make these materials promising for energy conversion. However, significant volume changes and interstitial hydrogen pose challenges for long-term stability.

Fe_2P-based $(Mn,Fe)_2(P,X)$ compounds, where X=As, Ge, Si, or B, are also notable MC materials. These compounds can exhibit a weak first-order magneto-elastic transition with a change in lattice parameters while maintaining a hexagonal crystal structure, characterized by low volume change and thermal hysteresis. The $MnFeP_{0.45}As_{0.55}$ compound was initially noted for its GMCE [36]. Substituting As with Si or Ge addresses toxicity issues but may increase thermal hysteresis and degrade mechanical properties [37], [38]. The transition is highly sensitive to changes in Si/P ratios or non-magnetic substitutions. For instance, adding B shifts the transition towards a second-order type, reduces thermal hysteresis, and improves transition temperature sensitivity and mechanical stability [39]. High reversible MCE values, tunable transition temperatures, and good mechanical stability make these compounds promising for refrigeration applications.

Heusler alloys are a diverse class of multi-functional materials with various properties (e.g., conductive, magnetic, thermoelectric) and applications (e.g., magnetic refrigeration, spintronics, shape-memory materials) [40]. In terms of MCE, a GMCE was first observed in Ni_2MnGa near its first-order martensitic transition [41]. This transition involves a cubic (austenite) to low-symmetry (martensite) phase change, which can be induced by an external magnetic field [42]. Off-stoichiometric Mn-rich Heuslers like $Ni_2Mn_{1+x}Y_x$ (Y=Ga, In, Sn, Sb) also show GMCE [43]. However, large thermal hysteresis, caused by lattice mismatch and symmetry changes, limits the efficiency with low magnetic fields ($\mu_0 H \leq 1$ T). MCE near the Curie transition in Heusler alloys is fully reversible but less intense compared to structural transitions. Co-rich alloys (e.g., Co_2FeSi) have high magnetization but high Curie temperatures, making them unsuitable for room-temperature applications. Excess Mn can increase magnetization without significantly affecting the Curie temperature, though the formation of an AFM phase limits achievable magnetization to around 6 μB per formula unit for $Ni_2Mn_{1.4}In_{0.6}$ [44]. Despite some challenges, the absence of rare earths and the versatility in composition make Heusler alloys promising for magnetic refrigeration and other applications. A more comprehensive discussion on Heusler compounds will be provided later (Section 3.3.1)

3.1.3 Magnetocaloric Devices

Magnetic refrigerators that utilize the magnetocaloric effect typically consist of three primary components: the magnetic field source, the magnetocaloric material, and the heat exchange system [45]. A conveniently designed apparatus must take care of varying the magnetic field applied on the MC material, also through the relative motion between magnetic field source and MC material, and the displacement of the heat exchange fluid between the MC material and the hot and cold ends.

In this section, the main parameters to consider in magnetic refrigerators are briefly outlined and a comprehensive list of devices based on the magnetocaloric effect are provided.

There are various methods to achieve magnetization/demagnetization of MCE materials, which usually define the type of magnetic refrigerator: static (Fig. 3-5 (a)), where the magnetic field intensity changes over time; reciprocating (Fig. 3-5 (b)), where the magnetic field source or the MCE material moves linearly to create a varying magnetic field on the material; rotary (Fig. 3-5 (c)), where the magnetic field source (or the regenerator) moves circularly around the regenerator (or the magnetic source). Different types of magnets are used for the magnetic field source, including superconducting magnets for low-temperature applications, while arrays of permanent magnets are preferred to conventional electromagnets for room temperature devices because of their capability of generating a magnetic field without the need for electric current supply. While the permanent magnets completely remove the need for energy supply in the generation of the magnetic field, on the other hand they introduce a cap to the maximum field available, effectively reducing the temperature change available to the machine. This will require the introduction of specific operative configurations in the design of thermal machines, as described below.

Regarding the MCE materials employed in these devices, gadolinium gallium garnet ($Gd_3Ga_5O_{12}$) has been extensively used in the development of magnetic refrigerators operating at cryogenic temperatures [46], while gadolinium metal has been considered the benchmark material for those functioning near room temperature [18]. In recent years, an increasing number of room temperature devices incorporate $La(Fe,Si)_{13}$-type materials.

Heat is continuously absorbed and released in the heat exchangers, with a heat transfer fluid transporting the heat between exchangers. Helium gas is commonly used as the heat transfer fluid to reach low temperatures for helium or hydrogen liquefaction or even lower temperatures, while water with some antifreeze additives is generally used in the development of room temperature prototypes. Liquid nitrogen can be found in applications at intermediate temperatures (oxygen or air liquefaction) or as an additional step for cryogenic temperatures.

Since the purpose of this thesis is the study of materials for magnetocaloric and thermomagnetic applications operating at room temperature, this section will not cover devices that operate at cryogenic temperatures.

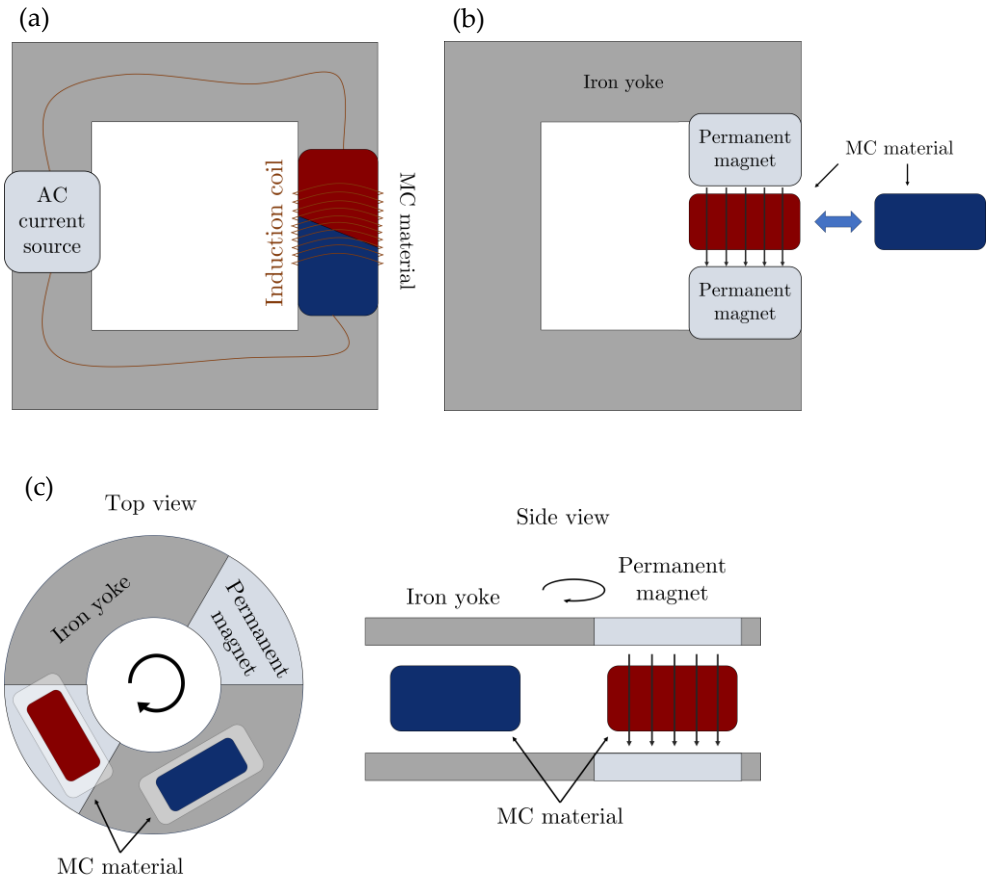

***Figure 3-5**: Sketches of MC static generator (a), MC reciprocator (b) and MC rotor (c) (top view on the left and side view on the right) for the magnetic refrigeration. The MC material is coloured in red or blue depending on its temperature.*

Brown's initial device utilized Gd disks suspended in a water-ethyl alcohol mixture within a reciprocating mechanism. Operating in a superconducting magnet's field of 7 T, it achieved a notable temperature span of 47 K after fifty cycles [47]. This marked the beginning of magnetocaloric refrigeration's exploration for near room temperature applications.

Following Brown's work, Steyert introduced the concept of Active Magnetic Regeneration (AMR) in 1978, revolutionizing the design with a rotary configuration. Gd placed on a rotating wheel interacting with magnetic fields achieved a 14 K temperature span at a frequency of 1 Hz [48]. This rotary approach offered advantages in continuous operation and efficiency over reciprocating designs. The AMR design is another pivotal improvement for magnetic refrigeration: the

magnetocaloric material itself is deployed in a high surface-to-volume fashion along the direction of fluid flow, allowing for a fast heat exchange with the heat conducting fluid and at the same time for the onset of a temperature gradient within the material itself. In this way it is possible to overcome the limited temperature jump achieved by the single magnetocaloric event and reach temperature jumps within the two ends of the machine that are meaningful for practical applications (a few tens of degrees).

In 1987, Kirol and Dacus presented a rotary heat pump employing 125 coaxial Gd disks in an Ericsson-type cycle, generating an 11 K temperature span under a 0.9 T magnetic field from Fe-Nd-B permanent magnets [49]. This configuration demonstrated improved thermal performance and marked the transition towards more complex geometries and materials.

By 1990, Green et al. further advanced the technology with a reciprocating magnetic refrigerator using Gd and Tb beds coupled with nitrogen gas. Their device, operated under a 7 T magnetic field, achieved a temperature span of approximately 24 K after extensive cycling [50]. This development underscored the versatility of magnetocaloric materials and their application in diverse refrigeration scenarios.

The late 1990s saw significant refinements in design and operational longevity. Zimm et al. introduced a reciprocating refrigerator utilizing Gd spheres in bed configurations under a 5 T superconducting magnet. This device demonstrated robustness and longevity, operating effectively for 18 months with a cooling power of 600 W and a temperature span of 10 K [51].

Further innovations continued into the 21st century. Rowe and Barkley (2001) from the University of Victoria introduced a reciprocating device using layered Gd and $Gd_{1-x}Tb_x$ alloys, achieving a 14 K span under a 2 T magnetic field [52]. Simultaneously, Astronautics Corporation of America patented a rotating refrigerator employing Gd, Gd-Er alloys, and $La(Fe_{0.88}Si_{0.12})_{13}H_1$, achieving temperature spans of up to 27 K under varying conditions of magnetic field strength and frequency [53], [54].

The following year, Canadian teams from the Universities of Victoria and Quebec advanced reciprocating refrigeration using permanent magnets, achieving temperature spans ranging from 16 K to 51 K under various configurations of Gd and Gd-based alloys [55]. These developments underscored the ongoing evolution towards higher efficiency, broader temperature ranges, and practical applications of magnetocaloric refrigeration technologies.

In 2006, the University of Applied Sciences of Western Switzerland showcased a rotary magnetic refrigerator at Hannover's industrial fair, integrating air as the working fluid and Gd-containing magnetic fluid within a rotating bed. This setup, operated under a 0.8 T magnetic field, was recognized with the Swiss Technology Award [56].

The following year, Astronautics Corporation of America developed a rotary magnetic refrigerator featuring twelve static beds filled with Gd, rotating under the influence of permanent magnets generating a 1.5 T magnetic field. Experimental trials with water and inhibitors as heat transfer fluids demonstrated a maximum temperature span of 12 K and a cooling power of 220 W at 4 Hz [57]. Additionally, Chelyabinsk State University introduced a rotary magnetic refrigerator employing Gd and NiMnGa alloys under a 1 T magnetic field, anticipating a cooling power of 40 W [58].

By 2009, Cooltech Applications in France developed another reciprocating AMR prototype with an array of parallel Gd plates and Halbach-type magnets, achieving a 16.1 K temperature span under optimized conditions [59]. Also in 2009, researchers from the Korea Advanced Institute of Science and Technology developed a reciprocating magnetic refrigerator using Gd particles. Their device employed sixteen segments of permanent magnets in a cylindrical configuration, achieving a magnetic field of 1.58 T. Operating frequencies up to 1 Hz yielded a maximum temperature span of 16 K using helium gas as the heat transfer fluid [60].

In 2011, the Technical University of Denmark introduced a reciprocating AMR utilizing a Halbach cylinder configuration of permanent magnets generating up to 1.03 T in the gap. The regenerator contained magnetocaloric material in a bed of parallel plates, achieving temperature spans of approximately 10 K with Gd, 7 K with La(Fe,Co,Si)13, and 10 K with two different Curie temperature $La(Fe,Co,Si)_{13}$ compounds [61].

In 2012, Park et al. from Korea Advanced Institute of Science and Technology developed a reciprocating AMR refrigerator with a static Halbach array providing 1.4 T. The regenerator included 0.186 kg of Gd and achieved a temperature span of 26.8 K and cooling power of 33 W using deionized water [62].

In 2015, Technical University of Denmark introduced a rotary AMR prototype utilizing concentric cylindrical magnets generating up to 1.2 T. The device achieved a temperature span of 10.2 K and 103 W cooling power using a mixture of demineralized water and ethylene glycol [63]. In the following year, Benedict et al. presented a rotary AMR refrigerator with cylindrical beds filled with Gd and Halbach array magnets providing fields from 0.05 to 1.5 T. The device achieved a

maximum temperature span of 21 K using a mixture of water and ethylene glycol [64].

In 2017, C. Aprea at al. [65] proposed a study in which a control technique designed to enhance the performance of a rotary permanent magnet magnetic refrigerator is discussed. The approach utilizes artificial neural networks to accurately predict the energy performance of such a refrigerator, achieving strong alignment with experimental results. This method enables the creation of a working map, which, through an optimization process, allows for the identification of the optimal operational parameters, specifically the rotational speed of the magnets and the volumetric flow rate of the regenerating fluid. The optimization can be tailored to either maximize the coefficient of performance, focusing on energy efficiency, or to enhance the cooling capacity, prioritizing time efficiency. As a demonstration, the study provides an example application of this method and suggests new avenues for the use of artificial neural networks in the field of magnetic refrigeration.

In 2018, Chaudron [66] described the development of the largest rotary magnetic refrigerator device, designed to provide 15 kW of cooling power with a 20 K temperature differential between the heat source and sink. The device featured 32 compartments for active magnetic regenerators, though initial testing was conducted with two regenerators utilizing five different Gd and Gd alloy materials with varying Curie temperatures. A rotating four-pole magnet assembly was driven by an external motor via a shaft, while fluid flow was managed by a circulation pump and cycle synchronization was controlled using custom mechanical valves. The authors reported achieving 60% second-law efficiency during preliminary testing.

In 2019, Krautz et al. [67] developed a rotary magnetic refrigerator designed as an air conditioning system, capable of achieving magnetic flux densities exceeding 1.4 T. The device featured an inner rotor with eight iron teeth, a stator equipped with four-pole permanent magnets, and an outer iron yoke. Magnetocaloric material chambers were positioned within the stator, comprising epoxy-bonded plates containing 55 vol% $LaFe_{11.4}Si_{1.2}Mn_{0.3}H_{1.8}$ produced, via tape casting. Additionally, Huang et al. [68] reported another rotary magnetic refrigeration prototype in 2019, incorporating a rotary magnetic field source generating an average magnetic field of 0.875 T. This device employed seven asymmetrically arranged packed-bed Gd regenerators weighing 1.18 kg in total. A real-time-controlled programmable solenoid valve system was utilized to synchronize fluid flow. The authors reported

achieving a maximum cooling power of 162.4 W at zero-temperature-span, with a zero-power temperature span of 11.6 K.

Recent advances in magnetocaloric cooling and heat pumping near room temperature have led to several studies that enhance prototype devices or apply them to new areas [69]. Research primarily focuses on the optimization of permanent magnets, with notable contributions from Wieshou et al. [70] and Almeida et al. [71]. Additionally, efforts in the processing and recycling of permanent magnets, such as the work by Benke et al. [72] and Schäfer et al. [73], are noteworthy.

Recent developments in hybrid electro-permanent magnets have shown the potential for achieving energy efficiencies over 70–80% at frequencies above 15 Hz, while concerns regarding electromagnetic overheating have been addressed [74], [75]. The integration of thermal switches and thermal diodes presents significant opportunities to enhance the power density of caloric devices, as explored by Silva et al. [76].

Research on magnetocaloric prototype devices has examined the rotation of permanent magnet assemblies and the performance of larger-scale cooling systems, including wine coolers and air conditioners. Studies have also investigated the feasibility of utilizing liquid metal propulsion in magnetocaloric devices and the innovative approach of sandwiching magnetocaloric materials between thermoelectric modules [77].

These advancements underscore the continuous evolution and maturation of AMR technology over the past decade. Researchers have successfully tackled challenges related to magnet design, regenerator optimization, and fluid dynamics to enhance cooling efficiency and expand the potential applications of magnetic refrigeration in various industries. As AMR devices become more efficient and scalable, they hold significant promise for future environmentally friendly refrigeration technologies.

3.2 Thermomagnetic energy harvesting

Although the thermomagnetic effect was first discovered in the 19th century, it remained largely overshadowed by other magnetically driven phenomena due to the low efficiency of the materials employed in its early applications. At the time, the thermomagnetic materials available exhibited limited performance, which hindered the practical exploitation of the effect. However, recent advances in the study of magnetic materials, particularly those investigated for their magnetocaloric properties, have led to a resurgence of interest in the thermomagnetic effect. This revival is closely linked to the fact that many of the magnetic compounds optimized for magnetocaloric applications have demonstrated similarly promising characteristics for thermomagnetic systems. The renewed focus on the thermomagnetic effect is particularly significant in the context of sustainable technologies, especially in the efficient recovery of low-grade waste heat. Thus, what was once considered a somewhat historical area of research has now reemerged at the forefront of materials science, driven by the need to explore novel multifunctional materials capable of harnessing thermomagnetic effects for modern energy applications.

3.2.1 Thermomagnetic Cycle

This section will describe the thermodynamic cycle that exploit the thermomagnetic effect of a magnetic material to convert thermal energy into a more useful kind of energy, such as mechanical or electrical energy. This cycle is referred to as the thermomagnetic cycle (Fig.3-6). The following treatment is based on the approximation whereby the system achieves thermodynamic equilibrium at each step of the thermomagnetic cycle; however, this approach allows each type of thermomagnetic conversion devices to be well described by this cycle and each step to be evident in the principle of operation of these [17]. Generally, the thermomagnetic cycle consists in two isothermal transformations (I-III) where the device produces work and two isofield transformations (II-IV) where the system exchanges heat with thermal sources.

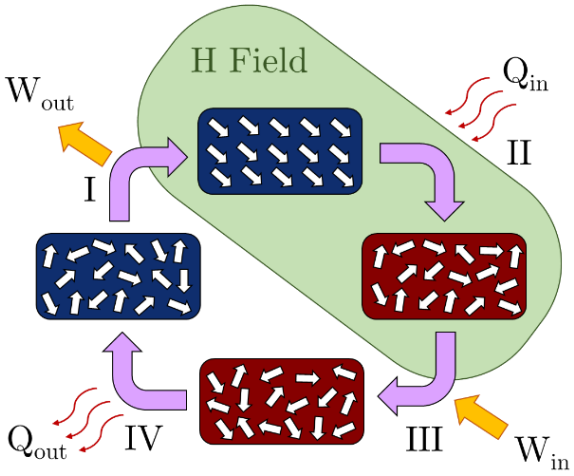

***Figure 3-6**: Conceptual scheme of the thermomagnetic cycle. The thermomagnetic material is subject to a change in temperature and a change in the magnetic field. The red rectangles represent the material at the T_{hot} temperature and the blue rectangles at the T_{cold} temperature. The green region represents the presence of an applied magnetic field H. Each thermodynamical transformation is enumerated in roman numbers and represented as purple arrows.*

Let's consider a magnetic material with transition temperature T_t between the two thermal sources temperature $T_{cold} < T_t < T_{hot}$. For energy harvesting of low-grade heat application, the temperature of the hot source T_{hot} is generally lower than 100°C while T_{cold} should correspond with the room temperature. The magnetic material in analysis has a magnetic moment dependent on the magnetic field and the temperature M(H,T), where M_{cold} and M_{hot} refer to the magnetic moment values of the material in the presence of a field H at the temperature of respectively T_{cold} and T_{hot} (where in this example $M_{cold} > M_{hot}$).

For the description of all steps of the thermomagnetic cycle, we will use the differential of the Gibbs free energy, defined for a magnetic material as [28], [78], [79]:

$$dG = Vdp - SdT - \mu_0 MdH \qquad (3.10)$$

The first term of eq. 3.10 is null throughout the cycle as all transformations occur at atmospheric pressure, while the other terms take on different values for each transformation. Remembering that for a closed loop the total Gibbs free energy difference is equal to zero, it is useful analyzing the ΔG value associated with each

step of the cycle to quantify the energy density that comes into play in each transformation.

I. **Step I** The TM material is initially at T_{cold} temperature. At a constant temperature, a magnetic field H is applied to the material which reduces the Gibbs energy by $\Delta G_I = -\mu_0 \int_{H_{min}}^{H_{max}} M_{cold} dH$.

II. **Step II** The heat provided by the hot source (Q_{in}) is used to heat up the thermomagnetic material beyond T_t, at a constant magnetic field, reducing the Gibbs free energy by $\Delta G_{II} = -\int_{T_{cold}}^{T_{hot}} S_{II} dT$. The magnetic moment of the material is reduced from M_{cold} to M_{hot}.

III. **Step III** Keeping the temperature constant at T_{hot} the magnetic field is removed, this requires to the system a value of Gibbs energy equal to $\Delta G_{III} = \mu_0 \int_{H_{min}}^{H_{max}} M_{hot} dH$.

IV. **Step IV** The thermomagnetic material is brought back into contact with the cold thermal source. The temperature of the material decreases to T_{cold}, entailing a change of Gibbs energy $\Delta G_{IV} = \int_{T_{cold}}^{T_{hot}} S_{IV} dT$ and its magnetic moment increases returning to the value it had in step I, closing the thermomagnetic cycle.

After one cycle the system can produce a useful work equal to the sum of the change of the Gibbs free energy across the first and third (or the second and the fourth) transformations [80] that correspond to the area between the two magnetic moment curves $M(H,T_{cold})$ and $M(H,T_{hot})$ in the magnetic field range from H_{min} to H_{max} shown in Fig. 3-7 and calculated by the integral:

$$W_{max} = \mu_0 \oint H \, dM \qquad (3.11)$$

As mentioned before, the difficulty in evaluating TM materials for low-grade heat energy harvesting applications lies in the number of different properties to assess.

A TM material should present a high change of magnetic moment in a temperature range as low as possible, this usually occurs in the magnetic transition. With reference to what was discussed in the previous section regarding first and second-order magnetic phase transitions, thermomagnetic materials can be divided into two categories depending on the magnetic phase transition they exhibit: thermomagnetic materials that present a phase transition of the first order are called First-Order Phase Transition (FOPT) while materials that present a second-order transition are called Second-Order Phase Transition (SOPT). Generally, FOPT materials are

characterized by a high and sharp change of magnetic moment but are often accompanied by thermal hysteresis that decreases the cyclic performance, especially for applications that provide a low temperature difference between thermal sources. Otherwise, SOPT materials have no thermal hysteresis, but the change of magnetic moment is not as sharp as the first-order transitions.

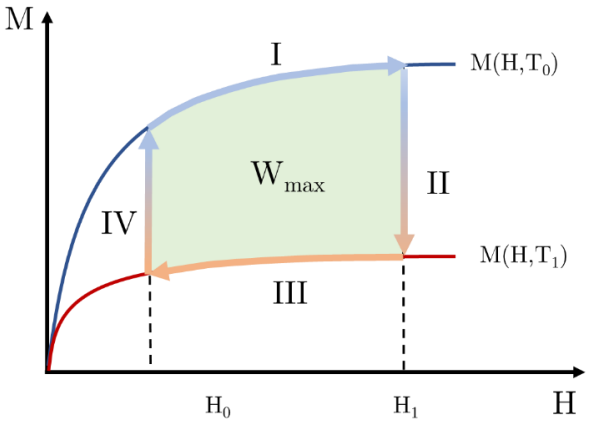

***Figure 3-7**: Representation of the two isotherm magnetic moment curves at temperatures T_{hot} and T_{cold}. Gibbs free energy difference between transformations I and III is represented by the area highlighted in green. The representation of the useful work presented in the image differs from the definition given in eq.3.11 since the integral represented has as variable H and not M. However, since they are integrals conducted along the same closed cycle, they are quantitatively identical.*

3.2.2 Evaluation of thermomagnetic properties

The thermal properties of the material also play a key role in the choice of thermomagnetic materials, by these, in fact, depend on the frequency of the thermomagnetic cycle and therefore the energy converted per unit of time of the device. The thermal properties can be estimated by looking at the thermal diffusivity value of the material, defined as follows:

$$\alpha = \frac{\rho k}{c_p} \qquad (3.12)$$

where ϱ represents the density of the material, k the thermal conductivity, and c_p the specific heat. However, in addition to the thermal characteristics of the material there are other aspects that determine the rate of heat exchange such as the

convective heat transfer coefficient of the transfer fluid of the thermal sources and the shape of the TM material.

Having established the difficulty of evaluating the thermomagnetic properties of material overall because of the high number of physical properties to be evaluated, it is however necessary to identify a simpler and more relevant possible figure of merit, which can provide an evaluation meter for thermomagnetic materials. The thermal efficiency, defined as

$$\eta = \frac{|W|}{Q_{in}} \cong \frac{\mu_0 \oint H \, dM}{\rho \int_{T_{cold}}^{T_{hot}} c_p(T) dT} \qquad (3.13)$$

is often used in the literature [81], [82]. This solution provides particularly relevant results to estimate the limit efficiency of the material, in fact, both the density of energy produced per cycle and the heat absorbed by the material are calculated. However, the classification of materials by the thermodynamic efficiency of the cycle presents an avoidable complication: the calculation of the absorbed heat. While the input thermal energy is quantitatively essential to assess the efficiency of the thermomagnetic cycle, the thermal properties of the material can be evaluated directly in the calculation of the produced energy density, which coincides with the area between the two magnetic moment curves of Figure 3-7. The higher the rate of heat exchange between the material and the sources the wider the area between the two magnetic moment curves will be.

A different approach is given by Dzekan *et al.* [17] where TM materials are evaluated using the power density (P_D) produced by the thermomagnetic cycle:

$$P_D = \mu_0 H \Delta M \qquad (3.14)$$

Where the terms $\mu_0 H \Delta M$ correspond to an approximated form of the Eq.3-11. The study of power density allows to evaluate, beyond the work obtainable from the thermomagnetic cycle, the speed of the cycle which, besides being particularly relevant from an application point of view, is closely related to the thermal properties of TM materials. Certainly, the best aspect of this method is the simplicity of the calculation necessary for the evaluation of TM materials, however this is due to the important approximation wherein the value of the magnetic field passes from a zero value to the H value in a discrete way. This does not happen from an application point of view, especially for magnetic field values in which the material is far from the saturation, and more generally the magnetic field varies from a minimum value of H_{min} to a maximum value of H_{max} continuously.

In this thesis, the useful work produced by the thermomagnetic material in one cycle per mass unit will be used as Figure of Merit (FoM), calculated as the area enclosed between the two M(H) isotherms corresponding to the highest and lowest temperatures reached by the material (Eq. 3.15). These two temperatures will be referred as T^{TM}_{hot} and T^{TM}_{cold}, respectively. The FoM is defined as the magnetic work per unit mass and is measured in J/kg.

$$FoM = \frac{1}{m} \oint_{M(T^{TM}_{cold})}^{M(T^{TM}_{hot})} H \, dM. \qquad (3.15)$$

The selection of the FoM allows for a simpler evaluation compared to the analysis of thermal efficiency in Eq. 3.13. In this case, it is not necessary to directly calculate the heat absorbed by the magnetic material during the cycle. However, the input energy of the system is taken into account in Eq. 3.15 through the choice of integration limits. Furthermore, the choice of using TM material temperatures as integration extremes and not thermal source temperatures is taken to make the FoM as accurate as possible.

The evaluation of TM materials based on the chosen FoM does not account for the assessment of the thermomagnetic cycle frequency. However, the frequency is intrinsically linked to the temperature difference exhibited by the material during the two transformations at constant field (II and IV), making it a challenging parameter to evaluate. In the case of a very fast thermomagnetic cycle (i.e., with high-frequency values), the time available for the TM material to exchange heat with the environment is reduced, resulting in a smaller temperature difference between T^{TM}_{hot} and T^{TM}_{cold}. This, in turn, reduces the area between the isotherms, as schematized in Fig. 3-7. Conversely, when considering a low-frequency cycle, the temperature difference in the TM material increases, thereby enhancing the magnetic work produced during the cycle. Given the dependence of the thermomagnetic cycle frequency on the material's ability to exchange heat with the thermal reservoirs, it is important to note that this heat exchange capacity is not solely determined by the intrinsic thermal properties of the magnetic material, as summarized by its thermal diffusivity (Eq. 3.12), but also by the geometry of the active material and the architecture of the thermomagnetic device employed.

3.2.3 Thermomagnetic Devices

The idea of using thermomagnetic effects for energy conversion has a rich history, dating back to the late 19th century [81].

In 1889, Nikola Tesla patented several innovative designs for thermomagnetic motors [83]. His design, depicted in Figure 3-8 (a), converted thermal energy into mechanical energy through the interplay of heat, magnetism, and a spring mechanism. Tesla's thermomagnetic motor utilized an electromagnet or a permanent magnet to generate a magnetic field, which interacted with an armature connected to a pivoting arm. When a burner heated the armature above its Curie temperature, the spring pulled the armature away from the magnet. Once the armature cooled below the Curie temperature, the magnetic force overcame the spring tension, returning the armature to its original position. This cyclical heating and cooling maintained continuous motion.

Thomas Edison [84] introduced a similar concept known as the pyromagnetic motor (Figure 3-8(b)), which used heat generated from burning coal or wood. Edison's design featured a thin iron sheet armature with longitudinal tubes, mounted vertically on a shaft and placed between magnetic poles. A furnace beneath the armature had outlets directing hot air through some tubes and cold air through others, creating a temperature differential. This caused uneven magnetization across the armature, resulting in continuous rotation as long as the heating and cooling cycles persisted.

In 1890, Tesla further advanced the field with a patent for a pyromagnetic electric generator, aiming to produce electric current directly without mechanical motion [85]. As shown in Figure 3-8 (c), this device used a permanent magnet bridged by an armature core composed of iron tubes, with conductors coiled around it. Heating and cooling the central portion of the armature alternately switched the magnetic circuit on and off, inducing an electrical current in the conductors.

In 1892, Edison patented another type of pyromagnetic generator (Figure 3-8 (d)) [86], which included bundles of thin iron tubes arranged inside two iron rings. Strong permanent magnets or electromagnets magnetized these tubes, forming the poles of a long magnet, with each tube bundle surrounded by windings. A furnace placed beneath the lower ring, along with a rotating shield, alternately heated and cooled the tubes, causing variations in magnetization and generating current in the windings.

As illustrated in Figure 3-8, these early thermomagnetic devices were highly complex and relied on iron as the working ferromagnetic material. Iron's high Curie temperature (768 °C) posed significant challenges, including the risk of thermal degradation of the permanent magnets and the need for substantial fuel combustion, raising economic feasibility concerns.

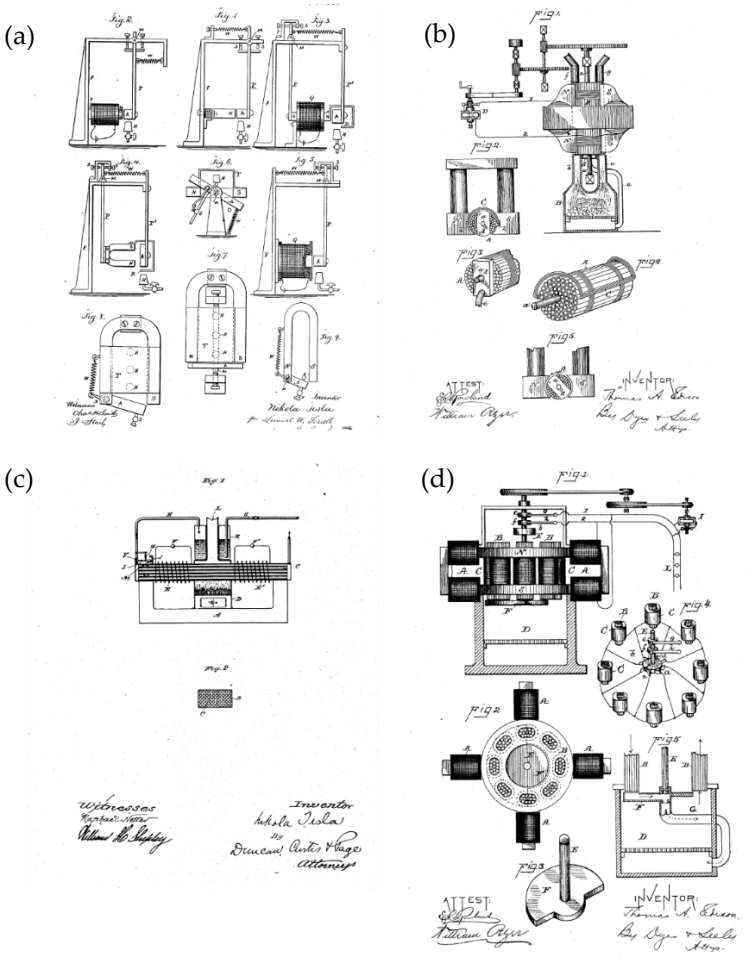

***Figure 3-8**: Few early thermomagnetic devices. Thermomagnetic motor by N. Tesla (a), pyromagnetic motor by T. Edison (b), pyromagnetic generator by N. Tesla (c) and pyromagnetic generator by T. Edison (d).*

Fast forward to the present, and the evolution of material science, coupled with cutting-edge engineering techniques, has revolutionized thermomagnetic devices. Modern thermomagnetic energy harvesters utilize advanced magnetic materials with precisely optimized transition temperatures and sophisticated design

methodologies to achieve unprecedented efficiency and scalability. These contemporary devices are not only more efficient but also more versatile. The advancements in thermomagnetic technology demonstrate significant potential for enhancing energy efficiency and sustainability across diverse sectors.

As previously written, the efficiency of the cycle, and therefore of the conversion device, is closely linked to the difference of magnetization of the material in the range of the working temperature of the device. However, other aspects are particularly relevant to maximize conversion performance, one of which is how thermomagnetic material exchanges heat with thermal sources. In fact, the more the temperature variation is wide and fast in the isofield II and IV transformations, the less time it takes for the device to complete an entire cycle increasing the working frequency of the device. Currently, in the literature, there are some examples of devices for the conversion of low-grade heat that differ in "architecture", method of heat exchange with the sources, and the type of energy produced [81], [12], [16].

Generally, the conversion devices that exploit the thermomagnetic cycle can be divided into the three families whose operating principle is schematized in Figure 3-9, these are called TM generators, TM oscillators, and TM rotors. The operations and characteristics are summarized below.

3.2.3.1 TM Generators

From a conceptual point of view, the TM generator is very similar to an electrical circuit within a magnetic field flow. As schematized in Figure 3-9 (a) the field lines are generated by a permanent magnet and flow into a magnetic yoke. Inside the yoke there is a thermomagnetic material that acts as a switch, since the magnetic field flow depends on the magnetization of the material when it changes value, following a change in temperature (transformations II and IV), the system exhibits a magnetic flux variation that can be used to generate electricity through a coil that wraps the magnetic yoke.

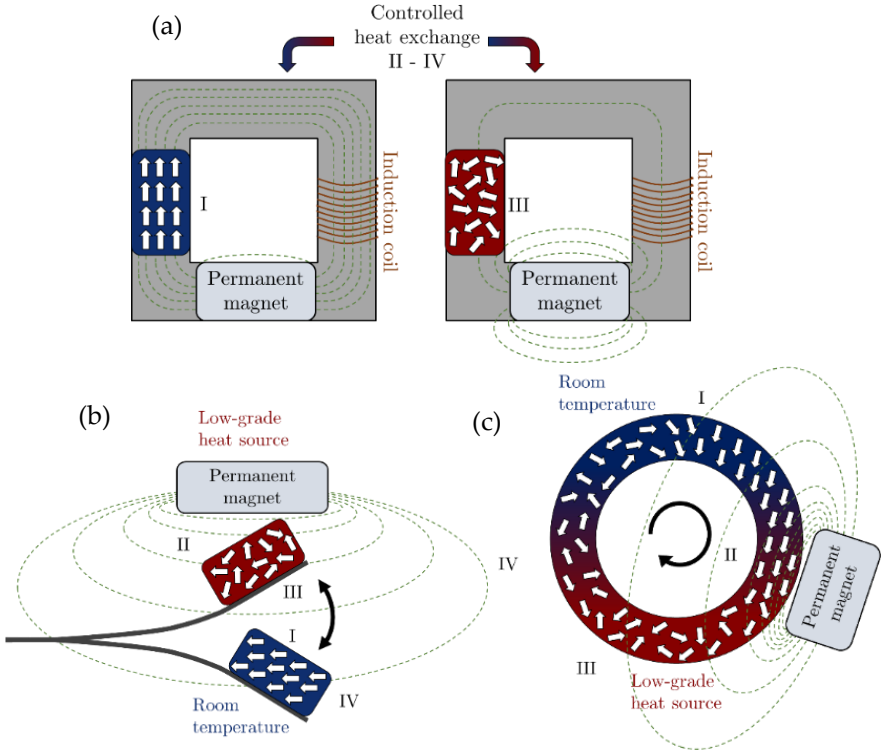

***Figure 3-9**: Illustrations of (a) the TM rotor, (b) the TM oscillator, and (c) the TM static generator, designed for waste heat recovery. The TM material is shown in either red or blue to indicate its temperature. Arrows within the material represent the orientation of magnetic moments. The numbers in brackets refer to the stages of the TM cycle detailed in figure 3-6.*

The first proof of concept of thermomagnetic generation is presented by V. Srivastava et al. [87] in 2011 realizing a TM generator based on a Heusler compound NiCoMnIn with a composition chosen to present a martensitic transition at about 410 K characterized by a low thermal hysteresis. Another interesting work about TM generators was published by T. Christaanse and E. Brück [82] in 2014, in this case as thermomagnetic materials were used some disks of $(Mn,Fe)_2$ (P,As) with different Curie temperatures between 300K and 310K. More recently it has been reported by A. Waske et al. [88] a static TM generator configuration that differs from the diagram of Figure 3-9 (a) in the number of closed loops of the magnetic circuit, the authors demonstrated experimentally and through a simulation an increase in the performance of the device increasing to three closed loops of the magnetic circuit. The device uses a thermomagnetic alloy based on La-Fe-Co-Si with a transition temperature at 300K and is 1.5 mV.

This type of device certainly has the great advantage of converting heat directly into electricity, thus avoiding further conversion of mechanical energy and thus avoiding further loss of system efficiency. However, since they are static generators, the thermomagnetic material cannot vary its temperature by moving from one thermal source to another, this leads to the need to use controlled flows for the heat exchange of transformations II and IV. This last aspect not only involves an additional energy consumption that should be considered in the calculation of the efficiency of the device, but also ward off the possibility of using these devices in energy harvesting applications that are usually characterized by fixed thermal sources.

3.2.3.2 TM Oscillators

In this configuration (Figure 3-9 (b)), the thermal energy is converted into vibrational energy. Generally, a thermomagnetic film is placed on the top of a cantilever which is attracted to the magnetic field source at room temperature. If the field source coincides with the hot thermal source of the system, the material heats up decreasing its magnetization, and the elastic force of the cantilever returns the material at the initial configuration. In 2016, M. Gueltig et al. [89] realized an oscillator prototype based on a 5μm thick Ni-Mn-Ga film. The system was able to convert vibrational energy into electric energy through a pick-up coil located on the cantilever that vibrates in a magnetic field gradient generating an induced current. The authors show how the device's performance increased greatly when the system oscillated at the resonance frequency of the cantilever generating about 40 mV at a frequency of 85 Hz. The same year, J. Chun et al. [90] proposed an alternative and particularly effective method for converting mechanical energy into electricity. The authors using a 127μm thick Gd foil made a device capable of generating about 3 V using a piezoelectric cantilever with a frequency of about 3 Hz. Moreover, it has been shown how connecting in series more devices is possible to remarkably increase the produced energy obtaining 17 V with 8 foils of Gd, however having the Gd a transition temperature at 294 K the thermal sources used for this work had a temperature of -10°C and 70°C for the cold and hot source respectively, making the device not suitable for energy harvesting applications at room temperature.

These kinds of devices, although they are characterized by rather low energy outputs, are very promising for micro harvesting applications that work at high frequencies. The possibility of working at higher frequencies than those allowed by other TM devices comes from the greater thermal diffusivity of the films (or thin foils) compared to the bulk counterpart. This allows the material to exchange heat with the environment faster and increases the speed of thermomagnetic cycles.

3.2.3.3 TM Rotors

These devices, like oscillators, convert thermal energy into mechanical energy (rotational in this case) which will have to be converted into electrical energy later. In this configuration (schematized in Fig. 3-9 (c)) the thermomagnetic material is characterized by a circular shape, usually called rotor, near the two thermal sources and the magnetic field source. A characteristic of these types of devices is that all the steps that make up the thermomagnetic cycle occur simultaneously at different points of the rotor.

The principle of operation is based on the magnetic force that is established at every point of the magnetic material in the presence of a magnetic field. This force also depends on the value of the magnetization of the material and therefore on the temperature, in this way the region of the rotor that is at the interface between the two thermal sources, where usually should lie the point of maximum magnetic field value, undergoes a non-zero magnetic force that puts the rotor in rotation, generating mechanical energy.

The TM rotors are particularly promising in the application field, for example R. Kishore et al. [91] show how a gadolinium-based rotor is able to operate even in a particularly low thermal gradient (2 K) generating a power density of about 100 $\mu w/cm^3$, with performance increasing by more than four times when the temperature difference between hot and cold source is increased to 10 K. Recently the Swiss blue Energy company has published the results obtained from their TM rotor prototype [92] that can generate more than 500 W by imposing a temperature difference of about 60K on six different points of a large gadolinium rotor.

The possibility of generating large amounts of energy is certainly one of the most promising aspects of these devices. However, the most relevant examples in the literature are based on rotors made of gadolinium that, while on the one hand is characterized by excellent thermal properties compared to alloys composed of different materials, on the other gadolinium is a rare earth metal and its criticality do not make it a viable option [93].

3.3 Materials

3.3.1 Heusler compounds

The history of one of the most fascinating material classes dates back to 1903 when Fritz Heusler discovered that an alloy composed of Cu_2MnAl behaves like a ferromagnet, even though none of its constituent elements are magnetic on their own [40]. This extraordinary material and its relatives, which now include a vast array of over 1500 compounds, are known as Heusler compounds. These materials are ternary, either semiconducting or metallic, with a 1:1:1 (referred to as "Half-Heusler") or a 2:1:1 stoichiometry. Figure 3-11 provides an overview of the possible combinations of elements that form these materials.

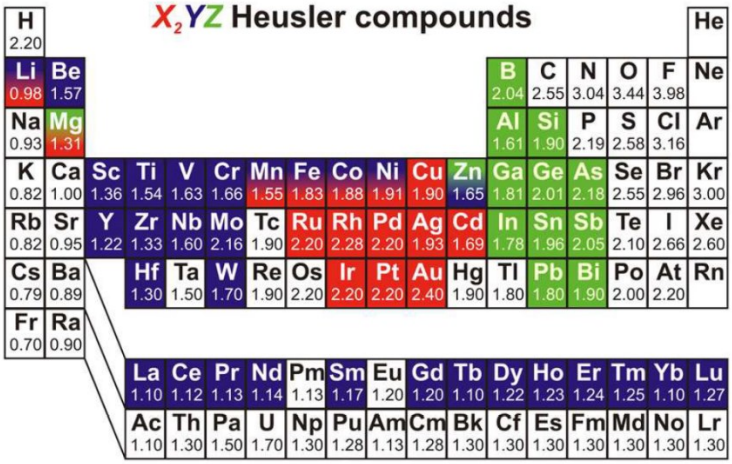

***Figure 3-10**: Periodic Table of Elements, with color-coded highlighting to indicate all possible combinations of elements that can form a Heusler compound. Each color represents a specific grouping or type of element that can participate in Heusler phase formation [40].*

Interestingly, the properties of many Heusler compounds can be predicted simply by counting the number of valence electrons [94]. The extensive class of magnetic X_2YZ compounds exhibits various kinds of magnetic behavior and multifunctional magnetic properties, including magneto-optical [95], magneto-structural [96] and magnetocaloric characteristics [97]. Among the large family of magneto-electrical Heusler compounds, half-metallic ferromagnets are semiconducting for electrons of one spin orientation while metallic for electrons with the opposite spin orientation. These compounds exhibit nearly fully spin-polarized conduction electrons, making them suitable for spintronic applications. Half-metallic Co_2-based Heusler

compounds continue to attract interest due to their high Curie temperatures [98] and are currently used in magnetic tunnel junctions [99].

From a magnetic perspective, specifically in the fields of magnetocalorics and thermomagnetics, Heusler alloys are of particular interest because certain compositions exhibit not only the classic Curie phase transition but also a first-order magnetostructural transition that can be driven by the magnetic field [100]. This transition is a displacive solid-solid transformation between a cubic phase (austenite) and a low-symmetry phase (martensite).

Half-Heusler materials XYZ can generally be seen as compounds that consist of both covalent and ionic components. The X and Y atoms exhibit distinct cationic characteristics, while Z serves as the anionic counterpart. Generally, X is the most electropositive element and can belong to the main group, a transition metal, or a rare earth element. The most electronegative element, which is placed at the end, is a main group element from the second half of the periodic table.

Historically, Heusler compounds were often regarded as intermetallic alloys, though describing them as intermetallic compounds is more accurate due to their characteristic atomic order. Ternary Heusler compounds have the general formula X_2YZ, where X and Y are transition metals, and Z is a main group element. However, in some cases, Y is replaced by a rare earth element or an alkaline earth metal. Traditionally, the metal that appears twice is placed at the beginning of the formula, and the main group element is at the end, such as in Co_2MnSi or Fe_2VAl.

Since this thesis will only study NiMn-based Heusler alloys (with the generic formula Ni_2MnZ with Z = In, Sn or CuGa), the following discussion will no longer address Half-Heusler compounds. Henceforth, the term Heusler alloys will refer exclusively to alloys with a generic 2:1:1 stoichiometry.

In the austenite state, Heusler alloys exhibit an $L2_1$ structure (space group fm-3m), which is composed of four interpenetrating face-centered cubic (fcc) sublattices, as illustrated in Figure 3-11 (a). For stoichiometric compositions, Ni atoms occupy the 8c positions (in Wyckoff notation), while Mn and Z atoms occupy the 4a and 4b positions, respectively [100]. When the temperature decreases, these alloys can undergo a martensitic transformation, adopting various structures. Specifically, NiMnZ Heusler alloys (where Z can be Ga, Al, In, Sn, or Sb) transform into the $L1_0$ tetragonal structure at low Z concentrations, which is also the ground-state structure of the parent compound $Ni_{50}Mn_{50}$.

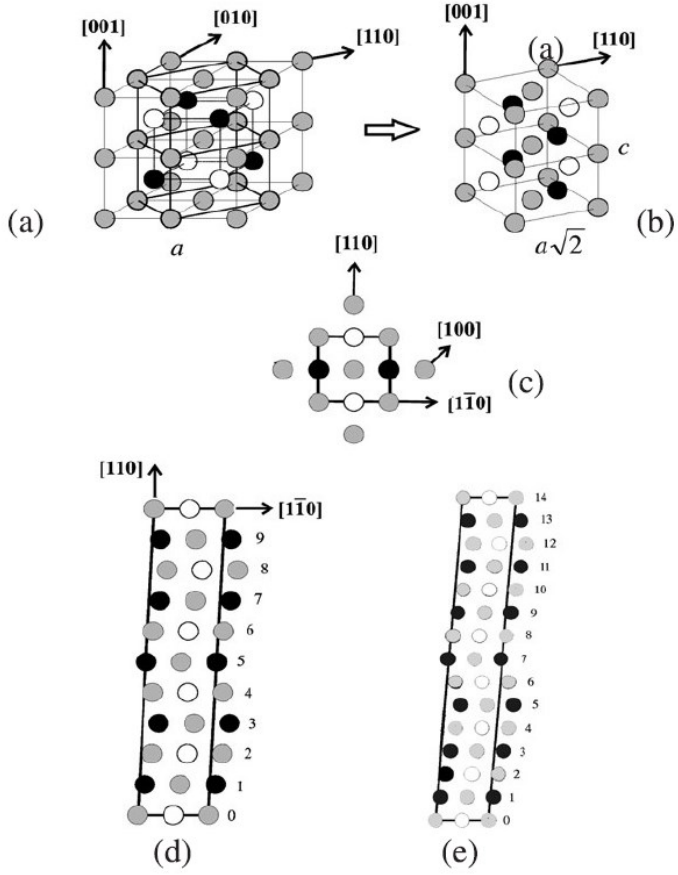

***Figure 3-11**: Austenite and martensite structures of Heusler alloys illustrated for $Ni_{50}Mn_{25}Ga_{25}$. Light grey spheres represent Ni, white spheres represent Mn, and black spheres represent Ga atoms. (a) The $L2_1$ Heusler structure is depicted, along with its relation to the tetragonal unit cell, also shown in (b). (c) A top view of the tetragonal unit cell, while (d) and (e) display the 5 M (or 10 M) and 7 M (or 14 M) modulated structures, respectively, obtained through shearing of the tetragonal cell [100].*

The relationship between the $L2_1$ and tetragonal structures is depicted in Figure 3-11 (a), with the tetragonal structure also shown separately in Figure 3-11 (b). This is not the only structure observed in the martensitic state; monoclinic structures, are also possible. The most prevalent monoclinic structures are the 5M (e.g. $Ni_{50}Mn_{25}Ga_{25}$) and 7M (e.g. $Ni_{50}Mn_{33}In_{17}$) types. In the top-down view of the tetragonal structure in figure 3(b) is presented in figure 3(c), where the modulations for the 5M and 7M cases can be seen in figures 3(d) and 3(e). The term 'M' refers to

the monoclinicity resulting from the distortion associated with the modulation [100]. The 5M and 7M modulations are sometimes referred to as 10M and 14M.

Concerning the MCE, a giant magnetocaloric effect (GMCE) was identified in the Ni_2MnGa alloy near its first-order martensitic transition [41]. A GMCE was also observed in various off-stoichiometric Mn-rich Heusler alloys with the general formula $Ni_2Mn_{1+x}Z_x$, where Z can be Ga, In, Sn, or Sb [43], [101], [97]. For certain compositions, these alloys exhibit a low-temperature martensitic phase with low magnetization, generally due to an antiferromagnetic (AFM) state [102]. In such cases, an inverse-MCE is observed [97], [103], [104]. The structural transition, which features a significant volume discontinuity, can also be induced by applying external pressure, leading to a barocaloric effect [105].

For TM applications one of the main advantages of Heusler alloys is their high thermal diffusivity (defined in eq. 3.12), which leads to a high-power density in the typical temperature range of thermomagnetic applications [17], [19]. However, their application is hindered by significant hysteresis during first-order magnetic transitions. Given the numerous publications on Heusler thin films they are considered the most promising for microsystems. Indeed, these alloys have been successfully used in micro-oscillators [89].

The transition temperatures (both structural and Curie) and the magnetic ordering of the two phases can be modified by altering the alloy composition or introducing appropriate substitutional elements (e.g., Co, Fe, Cu) [106], [107], [108]. This allows control over the magnetocaloric properties of the alloy, including the nature (direct or inverse), intensity, and temperature range of the effect. Increasing the magnetic moment difference between the two phases at the transition enhances the MCE values and the power density [19], [101], [109]. However, the large thermal hysteresis characteristic of the martensitic transition limits the cyclability of the effect when using low magnetic fields ($\mu_0 H \leq 1$ T). This can significantly reduce or entirely eliminate the MCE and the efficiency of TM conversion in subsequent field applications [17], [101]. The primary cause of the large thermal hysteresis is the lattice mismatch between the two phases, involving a symmetry change and a high elastic energy cost [110], [111], [112]. To reduce this energy contribution at the phase boundaries, the martensite develops an adaptive twinned micro- or nanostructure [113]. Changes in composition can alter the adaptability of the martensitic phase to the austenitic phase, affecting the width of the hysteresis. Thermal hysteresis increases when the phases exhibit different types of magnetic ordering. Since hysteresis results from the energy barrier associated with the nucleation and growth process, enhancing the geometric and magnetic compatibility between the phases leads to a reduction in thermal hysteresis [114].

Other factors influencing thermal hysteresis include material microstructure (defects, grain size, local strains, phase coexistence), magnetic properties (magnetic ordering, magnetic anisotropies, magnetic domain structure, spin fluctuations), and chemical order [115].

For TM applications, the only effective way to exploit magnetic materials characterised by thermal hysteresis is to operate a thermomagnetic cycle in which the temperature difference between the thermal sources is sufficiently large to allow the material to fully transition during the cycle. Conversely, in MC applications, some studies have shown that a reversible MCE can be achieved by following minor loops in the mixed-phase region due to the finite width of the structural transformation [116], [117]. In minor loops, the forward and backward transformations proceed mainly through phase-boundary movements, reducing the high energy cost associated with nucleation processes.

Special attention should also be given to the ΔM observed in these alloys near the Curie transition. Although it is less sharp compared to the structural transition, it is fully reversible. As mentioned in Sections 3.1.1 and 3.2.1, the MCE and the TM efficiency near a second-order transition depend mainly on the material's magnetic moment and the intensity of the applied magnetic field. The Heusler alloys with the highest values of magnetization are the Co-rich ones (e.g., the alloy Co_2FeSi has a saturation magnetization (Ms) of 6 μB per formula unit). However, their Curie temperatures are very high, making them unsuitable for room-temperature energy conversion applications [98]. Substituting Co with Ni reduces the Curie temperature closer to room temperature (for the alloys Ni_2MnZ, where Z=In, Sn, Sb) but also reduces the saturation magnetization [118]. An excess of Mn atoms, which can occupy the sites of Z atoms, increases the magnetization with little effect on the Curie temperature. The tendency of Mn atoms to create an AFM coupling at short distances and the appearance of the martensitic phase at room temperature for low Z content limit the achievable increase in magnetization to about 6 μ_B per formula unit for the $Ni_2Mn_{1.4}In_{0.6}$ alloy [44], the limit in Z and Mn content depend on the type of Heausler alloy. The complex configuration of magnetic interactions within the Heusler cubic cell and the potential to introduce other elements offer opportunities to further increase magnetization and fine-tune the critical temperatures (Fig.3-12).

The absence of rare earth elements, straightforward preparation processes, and the flexibility to exploit various compositions and elemental substitutions make these materials highly attractive for magnetic refrigeration devices and thermomagnetic applications, although some challenges still need to be addressed.

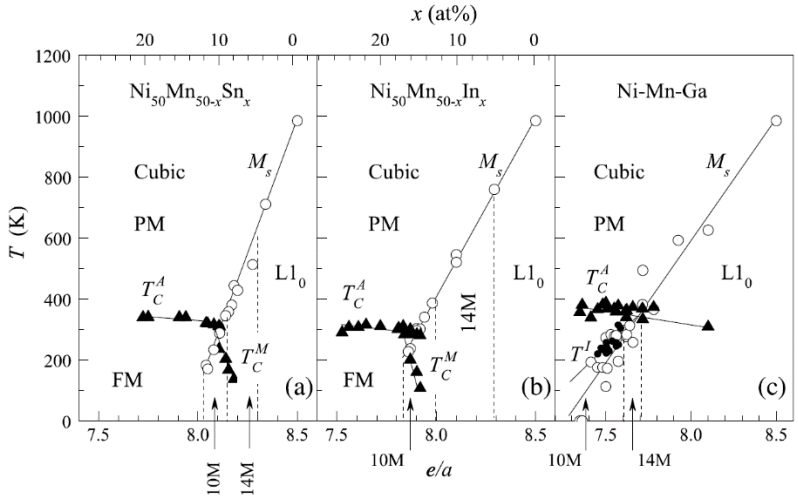

***Figure 3-12**: The magnetic and structural phase diagram for Ni–Mn–Z Heusler alloys, where Z represents (a) Sn, (b) In, and (c) Ga. Triangular markers denote the magnetic transition temperatures, while circular markers represent the martensitic transformation temperatures. Discontinuous lines delineate regions associated with distinct structural phases. In (c), smaller solid circles indicate the premartensitic transition temperatures [100].*

3.3.2 High Entropy Alloys (HEAs)

Metallurgy has been pivotal in shaping human history, providing the foundation for technological advancements, economic development, and societal evolution. However, recent years have witnessed a profound shift in alloy design methodologies. Traditionally, the prevalent practice involved the addition of trace elements to existing alloys to enhance their properties. Yet, this conventional approach has reached a point of diminishing returns, compelling researchers to explore novel strategies. Among these pioneering methodologies, HEAs emerge as a groundbreaking frontier in metallurgical science [119], [120].

HEAs represent a paradigm shift, leveraging the inclusion of five or more principal elements at elevated concentrations. This unique compositional framework unlocks a vast spectrum of possibilities, facilitating the discovery of alloys endowed with unprecedented and superior characteristics compared to their conventional counterparts. Notably, HEAs are distinguished by their exceptional mechanical attributes, phase stability, and remarkable resistance to both wear and corrosion.

The definition of HEAs hinges upon two primary criteria: one rooted in entropy and the other in composition. According to the entropy-based criterion, HEAs are

characterized by a mixing entropy ΔS_{mix} (Eq. 3.16) exceeding or equal to 1.5 R, where R denotes the gas constant and x_i is the molar mass of each element present in the alloy, and encompassing five or more principal elements, irrespective of their ambient temperature phase structure [121].

$$\Delta S_{mix} = -R \sum_i x_i \ln x_i \qquad (3.16) .$$

Conversely, the composition-based definition mandates HEAs to encompass at least five principal elements with concentrations ranging from 5% to 35%, while permitting minor elements up to 5% inclusion.

HEAs have captured considerable attention within the scientific community for their potential in functional applications. While initial studies predominantly delved into structural properties, as evidenced by the preponderance of publications, there's a burgeoning interest in exploring their functional attributes, particularly in the realm of magnetism [122], [123]. HEAs exhibit immense promise for applications such as magnetic refrigeration, owing to their optimal blend of magnetic and mechanical properties [124], [125], [126], [127], [128].

For the purpose of this thesis, it is useful to review the recent history of rare-earth-free HEAs without focusing on their rare-earth-containing counterparts. This choice stems from the fact that the aim of the work is to evaluate materials that are as non-critical as possible. Although rare-earth HEAs exhibit higher MCE values, their critical temperatures are very low (around 100 K) [121], making them less suitable for magnetocaloric and thermomagnetic applications near room temperature.

For the rare-earth-free magnetocaloric HEAs, they usually comprise transition metal elements, with initial investigations mainly focusing on tuning their transition temperatures. The work of Lucas et al. on enhancing the magnetic properties and TC of FeCoNiCr-type HEAs via Pd alloying [129] showed that $FeCoNiCrPd_x$ (x = 1 to 2) had a tunable T_C of 440–503 K when changing the Pd content and, at the same time, improved the saturation magnetization with Pd addition. They also reported a magnetocaloric study of another series of $FeCoNiCr_x$ HEAs (x = 0.5–1.15), where T_C values decreased with higher Cr content due to the reduced average exchange interaction [130].

Later, Na et al. reported on alloying Mn, Al, Ga, and Sn to FeCoNiCr HEAs and produced equiatomic FeCoNiCrM (M = Mn, Al, Ga, or Sn) HEAs [131]. While FeCoCrNiMn showed a single FCC phase similar to that of FeCoCrNi, dendritic microstructures composed of BCC-matrix (Ni- and Ga-enriched) and FCC-island (Fe-, Co-, and Cr-dominant) phases were observed for FeCoNiCrAl and FeCoNiCrGa HEAs. Only the additions of Al and Ga to FeCoNiCr changed the

parent paramagnetic behavior at room temperature to ferromagnetic. It is interesting to note that equiatomic FeCoNi is ferromagnetic with M_S = 161 A m^2 kg^{-1} but changed to paramagnetic at room temperature for equiatomic FeCoNiCr. Although the decrease in M_S of FeCoNiCrAl (25 A m^2 kg^{-1}) and FeCoNiCrGa (38 A m^2 kg^{-1}) HEAs is likely due to the dilution effects when alloyed with non-magnetic Al and Ga, their T_C could be tuned from 104 K (FeCoNiCr) to 277 and 703 K, respectively. The authors later extended this work to a systematic compositional variation study to further tune T_C in $FeCoNi_{1+x}Cr_{1-x}Al$ and $FeCoNiCr_{1-x}Al_{1+x}$ (for both cases x = 0–0.5) HEAs based on equiatomic FeCoNiCrAl [124]. They found that FeCoNiCrAl and $FeCoNi_{1.5}Cr_{0.5}Al$ HEAs displayed very broad magnetic phase transitions from 100 to 350 K with ΔS_T values of 0.674 (for 7 T at 290 K) and 0.277 J kg^{-1} K^{-1} (for 2 T at 150 K). These HEAs showed a dual phase of Fe–Cr-rich nanoparticles segregated within an AlNiCo-rich matrix, supported by their x-ray diffraction, microstructural, and thermomagnetic results.

Kurniawan et al. studied FeCoNiCuM (M = Mn, Ag, Pt, or Mo) HEAs for TC engineering, in which they found that their equiatomic alloys stabilized in the ferromagnetic face-centered cubic γ-phase (except for M = Ag and Mo), with T_C ranges from 400 to above 1000 K, and slight deviations from equiatomic compositions could further tune the T_C to near room temperature [132]. The reported MCE values were below 1 J kg^{-1} K^{-1} for a small magnetic field change of 0.55 T, and no further information for predicting the MCE at higher fields was available.

Thin films of FeCoNiCuAlCr HEAs fabricated by mosaic targets in magnetron sputtering enabled stoichiometric variation when the surface area of the target segment modifies [133]. Their thermomagnetic behavior shows a broad maximum similar to those observed for superparamagnetic systems, with a blocking temperature at about 325 K. For magnetocaloric properties, the material demonstrates a similar smeared behavior to several rare-earth-free HEAs in the literature, 0.53 (perpendicular to the field) and 0.38 J kg^{-1} K^{-1} (parallel to the field) for 5 T in a wide temperature span of ~200–325 K. Hence, the authors added that the magnetic cooling of these films would be ineffective.

In 2021 J.Y. Law at al published a study where significant result is obtained in $Mn_{22.3}Fe_{22.2}Ni_{22.2}Ge_{16.65}Si_{16.65}$ HEA. The alloy exhibits a magneto-structural first-order phase transition where the MCE of 7.3 J $kg^{-1}K^{-1}$ (for 2.5 T) is the largest reported to date for rare earth-free HEAs [134]

Very recently, research on magnetocaloric HEAs has deviated from the equiatomic compositions. The $Fe_{0.5}Co_{0.2}Ni_{0.5}Cr_{0.3}Mn_{0.89}Al_{0.3}$ HEA of duplex structure (BCC and FCC) was found to exhibit a round MCE peak (~0.16 J kg^{-1} K^{-1} for ~0.78 T) at ~326 K [135]. The authors calculated the magnetocaloric properties of the single BCC phase $Fe_{0.5}Co_{0.2}Ni_{0.5}Cr_{0.3}Mn_xAl_{0.3}$ (0.8 < x < 1.1) HEAs by normalizing their measured

data with the BCC phase fraction obtained from XRD results and reported that single BCC phase $Fe_{0.5}Co_{0.2}Ni_{0.5}Cr_{0.3}Mn_{0.94}A_{10.3}$ can be a promising magnetocaloric HEA within their selection for literature comparison. Thus, they added that stabilizing the BCC phase is an interesting direction for future work.

Sarlar et al., aiming to increase the magnetic properties in magnetocaloric HEAs, reported a non-equiatomic $Fe_{26.7}Ni_{26.7}Mn_{20}Ga_{15.6}Si_{11}$ alloy where the amounts of Fe and Ni were increased to more than equiatomic percent (i.e., 20 at. %) at the expense of Ga and Si [136]. They found that annealing the pieces from an as-cast 2-mm-diameter rod could enhance the $|\Delta S_{T\ peak}|$ values from 0.65 to 1.59 J kg $^{-1}$ K $^{-1}$ (both for 2 T) and T_C from 322 to 334 K, which shows promising MCE values among the magnetocaloric TM-HEAs (compared to those discussed above). The same authors also reported another rare-earth-free magnetocaloric HEA $Ni_{33}Cr_7Mn_{27}Ge_{25}Si_8$, retaining their former interests in strengthening the overall magnetic properties of the alloy when performing their elemental selections [126]. $Ni_{33}Cr_7Mn_{27}Ge_{25}Si_8$ exhibited an orthorhombic structure at room temperature and ΔS_T = 2.49 J kg $^{-1}$ K $^{-1}$ (2 T) with a T_C = 412 K. It is noteworthy to indicate that this MCE value is 57% larger than that of $Fe_{26.7}Ni_{26.7}Mn_{20}Ga_{15.6}Si_{11}$ HEAs [136], and both of these magnetocaloric rare-earth free HEAs displayed higher MCE magnitudes, without having to rely on the intrinsic large magnetic moments of rare-earth elements. This suggests that non-equiatomic compositions could be interesting for further exploration for rare-earth-free magnetocaloric HEAs.

Despite notable advancements, challenges persist HEAs face hurdles in surpassing the magnetocaloric efficiency limitations observed in conventional materials. Furthermore, research into functional HEAs remains relatively nascent, with the majority of studies concentrated on mechanical and structural domains.

In conclusion, the advent of HEAs marks a significant advancement in metallurgical science, promising extensive opportunities for the creation of cutting-edge materials with exceptional properties. Harnessing this potential necessitates ongoing research efforts focused on exploring the functional applications of HEAs, comprehensively grasping their properties, and fine-tuning them to cater to a wide range of industrial needs. This concerted approach is pivotal in unlocking the full capabilities of HEAs and realizing their transformative impact across MC and TM sectors.

4 Sample preparation

4.1 Arc melting

The samples studied in this thesis were fabricated using arc melting. This technique involves the use of an electric arc generated by an electrode that exploits a high potential difference between itself and the samples to be melted inside a chamber filled with an inert gas (Ar). This technique is widely utilized in both research and industrial settings for the production of intermetallics. Arc melting enables the production of uniform metallic alloys with minimal contamination and allows for rapid melting [137].

The arc furnace is essentially composed of four elements (Fig. 4-1): a Tungsten Inert Gas (TIG) generator, an operating handle that allows the management of the electrode and thus the electric arc, a tungsten electrode doped with thorium to increase its melting temperature [138], and water-cooled copper crucibles in which the raw materials to be melted for the synthesis of the alloy are placed.

The raw materials are washed in acetone and isopropanol to eliminate any carbon contamination, cut, and then weighed in the ratios of the desired alloy stoichiometry. Once the raw materials are placed in the crucibles, the chamber is sealed and connected to a vacuum pump (model to be specified). The chamber is evacuated using the vacuum pump and flushed with argon five times to remove air from the chamber. Additionally, approximately three grams of titanium, used as a getter, are melted before proceeding with the melting of the samples.

The time and current intensity employed to melt the alloys depend on the desired compositions. To compensate for the evaporation of certain materials with a high evaporation rate, a greater quantity of these materials is added to the crucibles. To increase the homogeneity of the samples, they are melted and flipped three to four times.

Once melted, the samples undergo heat treatment in a tubular furnace under a protective argon atmosphere to enhance chemical homogeneity and attain the desired crystal structure (Fig. 4-2). In fact, applying a heat treatment after the synthesis of magnetic materials enables sharper transitions, ensuring a change of magnetisation over a narrower temperature range. This enhancement increases the magnetocaloric and thermomagnetic properties of the alloys. The improvement of magnetic properties resulting from post-synthesis heat treatments is extensively discussed in the literature for both Heusler [139], [140], [141] alloys and HEAs [136], [142].

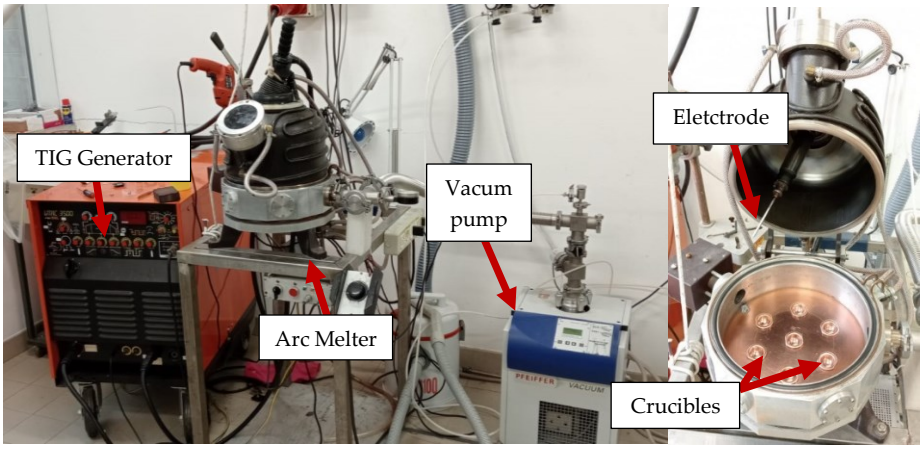

***Figure 4-1**: Photograph of an arc-melter (left) equipped with a tungsten electrode and a water-cooled copper crucible plate (right).*

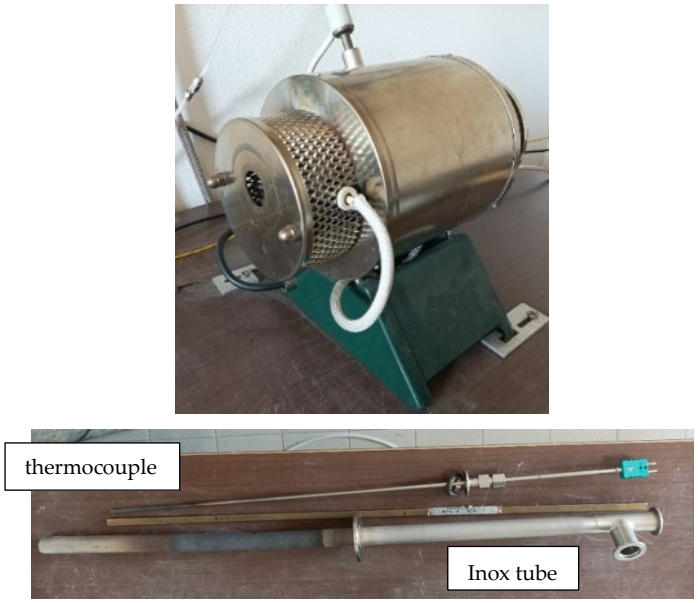

***Figure 4-2**: Photograph of tubular furnace used for the heat treatments (top) of the samples inserted into an inox tube near a thermocouple (bottom).*

Before the treatment, the alloys are washed in acetone and isopropanol and wrapped in specially cleaned tantalum foils that act as getters to prevent oxidation during the treatment.

Similar to the procedure used to eliminate the presence of air in the arc melting chamber, the stainless steel tube is evacuated and flushed with argon five times. The

temperature and duration of the treatment depend on the specific alloy being treated and will be indicated for each type of sample in Section 6. At the end of the treatment, the samples are water quenched.

4.2 Powder and composite

For the direct measurements of TM properties, which will be described in more detail in the upcoming sections, composites are used to fabricate rotors to be implemented in a thermomagnetic properties tester that will be detailed in the next section. To prepare the composites, powders are produced from bulk materials synthetized following the procedure described in the previous paragraph.

4.2.1 Powders

The powders are manually produced using an alumina mortar and a sieve with a 125 μm mesh (Fig 4-3). The mesh is necessary to ensure the powders do not exceed the desired size, while to avoid the powders being significantly smaller than 125 μm, only a few bulk fragments are crushed at a time, and the fragments are frequently passed through the mesh.

Once the powders are obtained, they are wrapped in a tantalum sheet washed with acetone and isopropanol to eliminate any carbonaceous residues and are thermally treated at 773 K for 4 hours using the tubular furnace shown in Fig. 4-2. Subsequently, they are water-quenched to recover the ferromagnetism and a sharp magneto-structural phase transition [143].

***Figure 4-3**:Picture of the agate mortar used to ground bulk samples into powders and the sieve used for controlling the maximum size of the powders.*

4.2.2 Mold manufactured composite

The rotor is constructed from an epoxy-based composite material that includes magnetic powder. The epoxy consists of bisphenol-A epoxy resin-based vinyl ester in styrene (Distitron Ve 100 by Polynt) combined with methyl ethyl ketone peroxide (Butanox M-50) as the hardening agent, chosen for its low water content and the absence of polar compounds. No metallic accelerators were added to the resin to avoid potential unwanted reactions with the magnetic material components. This resin was selected due to its minimal incorporation of air during mixing, as air bubbles in the polymer matrix negatively impact the composite's heat transport properties [144].

The composite is cast into a ring shape using a mold made of water-soluble bioplastic (Figure 4-4 (a)). At the center of the mold is an insoluble plastic support designed for attachment to the generator shaft, specifically engineered to minimize contact with the active material. To distinguish these rotors from those presented in the following section, they will henceforth be referred to as Mold Manufactured (MM) rotors.

The rotors have an external diameter of 20 mm, an internal diameter of either 18 or 17 mm, and a length of 1 mm (Figure 4-4 (b)). Henceforth, the rotor with an internal diameter of 18 mm will be referred to as the 1mm rotor, while the rotor with an internal diameter of 17 mm will be referred to as the 1.5mm rotor, with reference to the thickness of the rotors. When using a composite with 87±2 wt% magnetic powder, the net mass of active magnetic material in the 1mm and 1.5mm rotors is approximately 0.23g and 0.34g, respectively.

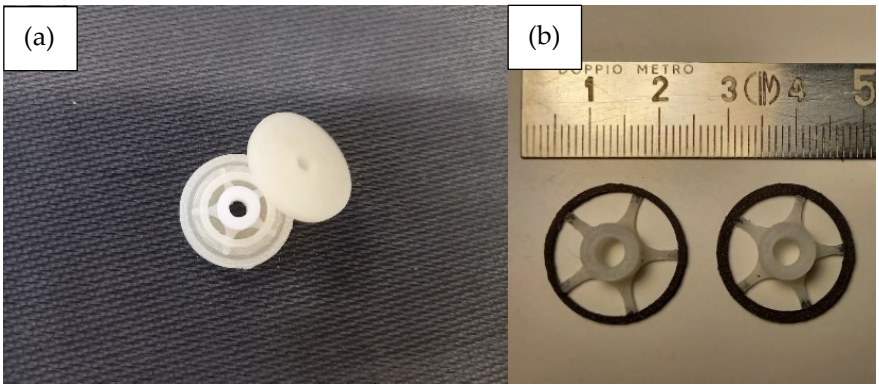

***Figure 4-4**: Picture of the water-solube molds (left) used to cast the 1 mm and 1.5 mm thick HC rotors (right).*

4.2.3 3d Printed composite

The Additive Manufactured (AM) rotors are made with the polymer PETG (Polyethylene Terephthalate Glycol-modified) and magnetic material. The work related to the production of the AM composite was conducted during an internship at the Institute of Condensed Matter of the University of Seville, Spain.

The use of a polymer allows the creation of a composite in the form of a 3D printable filament. The synthesis method of the composite follows the procedure described by A. D. Garzia et al. [145]. This process involves printing PETG capsules and filling them with magnetic material (the nominal ratio between the polymer and the magnetic material is approximately 50% wt). Subsequently, a PETG cover is printed and positioned to seal the capsules. Once sealed, the capsules are separated and inserted into a 3devo NEXT 1.0 Advanced extruder (Fig. 4-5 on the left).

The extruder transports the capsules through a screw mechanism, passing through four heaters with adjustable temperatures. The composite filament is then cooled with fans and passes through a sensor that measures its thickness to control it throughout the manufacturing process. Finally, the filament is wound using a winder. Once the composite filament is obtained, it is used for 3D printing with a Prusa MK3S (Fig. 4-5 on the right) to produce rotors of different sizes.

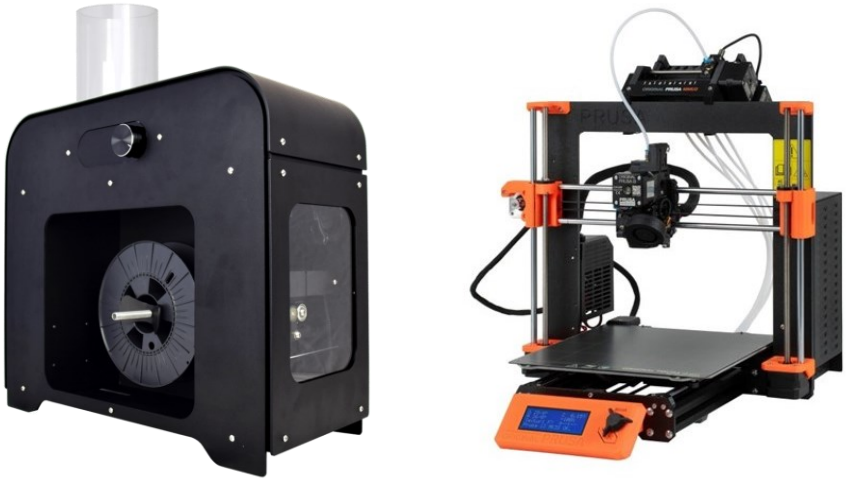

***Figure 4-5**: Photograph of the NEXT 1.0 Advanced extruder (left) used to produce the filament of both the PETG polymer and the AM composite and the 3D printer Prusa MK3S (right) used to print the AM rotors.*

5 Experimental

5.1 ThermoMagnetic Analysis (TMA)

Usually, the first measurement conducted after synthesis is a ThermoMagnetic Analysis, which basically consists of a measurement carried out with an in-situ developed susceptometer. This allows for highly precise measurement of the magnetic susceptibility of a sample as the temperature varies. Measures can be conducted during both heating and cooling phases under a magnetic field of about 10 Oe. This allows for the identification of the Curie transition and the magnetostructural martensitic transition, if present. The basic design of this AC susceptometer, schematized in Fig. 5-1 (a), includes a solenoid that generates a small alternating magnetic field, four pick-up coils to measure the induced voltage in the specimen (proportional to $-dM/dt$) (Fig. 5-1(b)), and two compensation coils to balance the sensing unit in the susceptometer. When there is no sample, the ideal pick-up coils induce zero electro-motive force. Inserting a magnetic sample into one of the secondary coils generates a non-zero signal proportional to the AC susceptibility, $\chi = \chi' - j\,\chi''$, of the specimen [146]. To separately measure the real (in-phase, χ') and imaginary (out-of-phase, χ'') components, a lock-in amplifier is used, requiring a reference signal that matches the frequency and phase of the current from the AC source. The amplifier outputs a magnified DC voltage proportional to its synchronous AC input signal, which can be detected and analysed using computer software. It is important to highlight that magnetic susceptibility measurements do not yield quantitative values and are not directly correlated with magnetization

For measurements, a sample mass of about 50 mg is used, and the rod with the sample attached is immersed in liquid nitrogen to start measurements from cryogenic temperatures. The maximum temperature achievable by the TMA is approximately 1073 K, but in this thesis, only measurements up to a maximum temperature of 420 K will be shown to explore the temperature range most relevant for TM and MC applications.

The temperature of the sample is controlled by a heater made in situ using a tungsten wire that surrounds the sample, passing through thin quartz vials positioned parallel to the rod where the sample is located (Fig. 5-1 (b)). This geometry is chosen to prevent the tungsten wire from forming a solenoid around the pick-up coils and

generating a false signal. Additionally, the heater is wrapped in a sheet of tantalum to concentrate the heat towards the sample limiting irradiation losses. The temperature is increased at a constant rate of 0.10 V/min until the maximum temperature needed for observing the magnetic Curie transition.

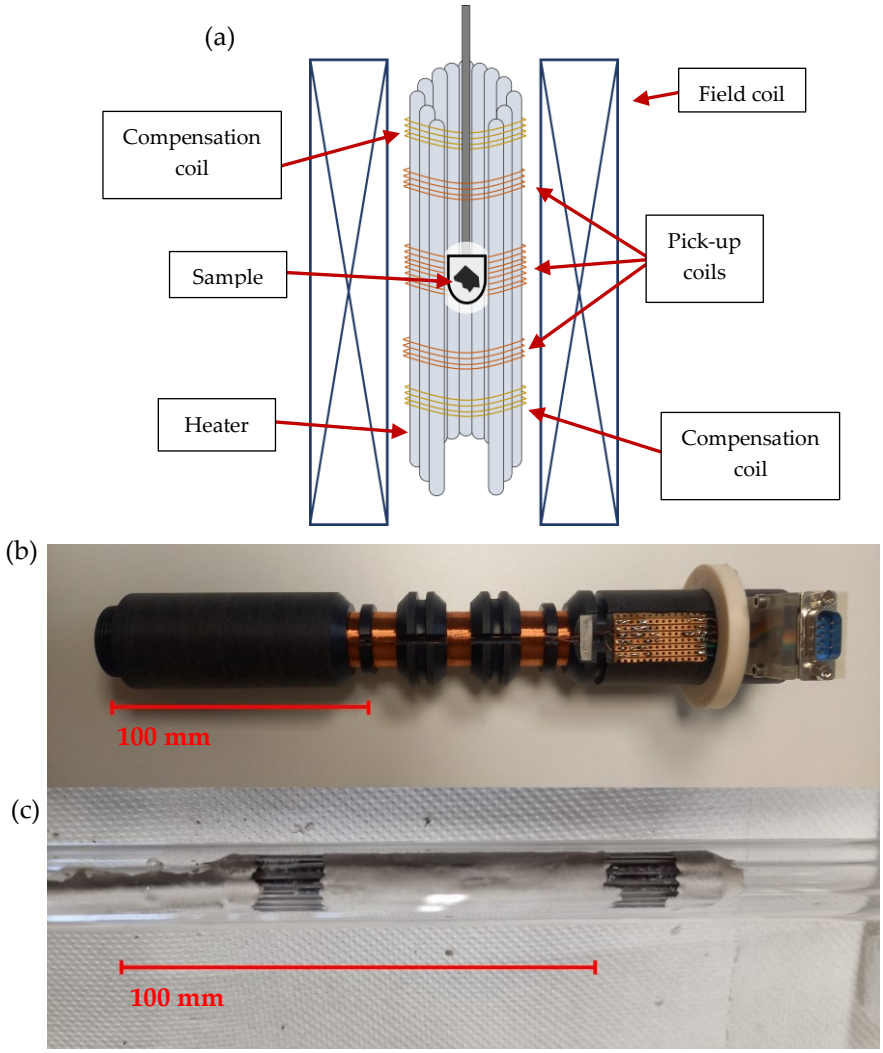

***Figure 5-1**: (a) Schematic representation of the TMA susceptometer to measure the magnetic susceptibility as a function of temperature. All relevant components discussed in the text are highlighted with red arrows. The photograph of the pick-up coils and the heater mounted in the TMA are reported in (b) and (c) respectively.*

Measurements performed at high temperatures are conducted in Ar atmosphere to prevent sample oxidation. The minimum temperature reachable during the cooling measurements is around room temperature.

5.2 Extraction magnetometer

The magnetic moment measurements as a function of temperature, conducted at a fixed external magnetic field, are performed in the Magnetometry laboratory at the Physics Department of the University of Parma using an extraction magnetometer, Fig. 5-2. This magnetometer features an electromagnet capable of generating up to 2 T and a rod with the encapsulated sample attached to the bottom end. The rod is vertically inserted into a region of uniform magnetic field and can be automatically extracted (~1 s) from this region by an electric motor. During extraction, two pairs of pick-up coils register the induced voltage, which, when integrated, is proportional to the magnetic moment of the specimen.

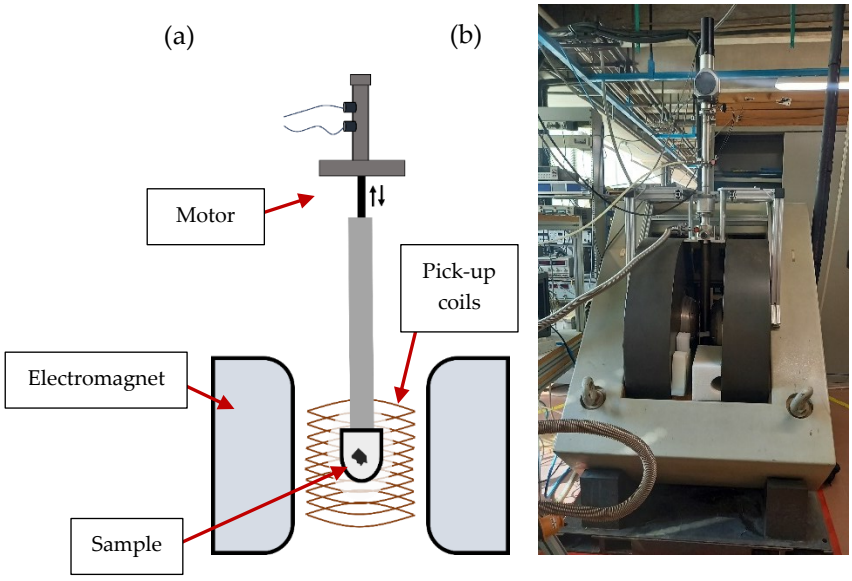

***Figure 5-2**: (a) Schematic representation of the extraction magnetometer. All relevant components discussed in the text are highlighted with red arrows. (b) Photograph of the extraction magnetometer.*

Both bulk and powder samples with a mass of approximately 20-40 mg were measured at 10 mT and 1 T. Measurements were taken during heating and cooling ramps at a constant sweep rate of 2 K/min to ensure equilibrium conditions and accurately study the magnetization behavior and thermal hysteresis across the

martensitic transformation. These measurements were conducted over a temperature range of 80 K to 350 K using a cryostat cooled with liquid nitrogen.

5.3 Stationary pendulum magnetometer

The magnetic moment measurements as a function of magnetic field, conducted at a fixed temperature, are performed in the Magnetometry laboratory at the Physics Department of the University of Parma using a stationary pendulum magnetometer (Fig. 5-3). The instrument allows for the evaluation of the sample's magnetic moment indirectly through a measurement of the torque moment of a tungsten wire transmitted by the rod on which the sample is placed. When the sample is subjected to a magnetic field gradient in the x direction, a magnetic force acts on it that depends on the magnetic moment of the material:

$$F_x = M\mu_0 \frac{\partial H_z}{\partial x} \qquad (5.1)$$

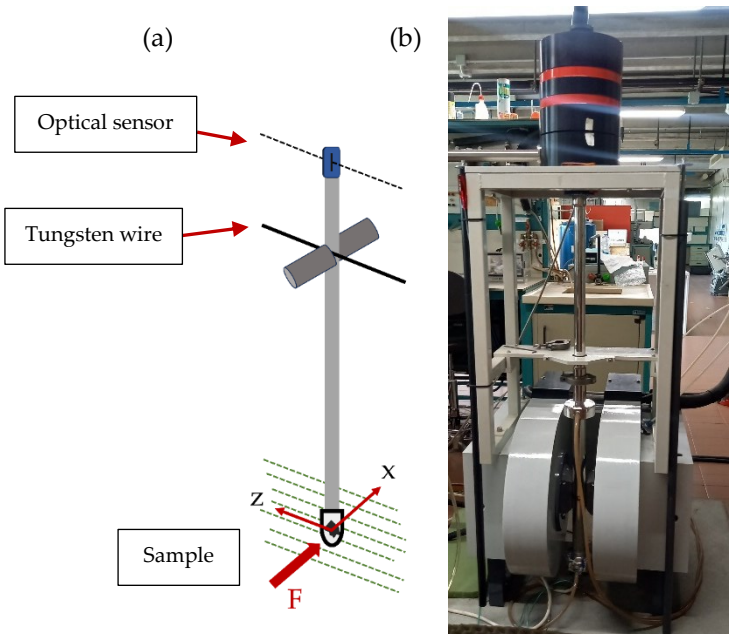

***Figure 5-3**: (a) Schematic representation of the stationary pendulum magnetometer. All relevant components discussed in the text are highlighted with red arrows. (b) Photograph of the magnetometer.*

The system uses optical sensors positioned at the top of the rod to return the sample to its original equilibrium position by applying a torque force. This force at dynamic equilibrium is equal to the magnetic force in eq. 5.1. The measurement of the torque moment applied by the system thus allows the determination of the sample's magnetic moment.

This system allows for measurements at both cryogenic temperatures (80 K) and high temperatures (1000 K), and the external magnetic field can go up to 2T. Given the operating method of the magnetometer, it is clear that magnetic moment measurements as a function of temperature would be excessively time-consuming due to the inability to measure by applying a temperature ramp. For this reason, the stationary pendulum magnetometer is used only for magnetic moment measurements as a function of the external magnetic field, keeping the system's temperature constant.

5.4 SQUID magnetometer

To magnetically characterize small amounts of fine powder and investigate the magnetic behavior of some powder batches down to a few Kelvin, a Superconducting Quantum Interference Device (SQUID), specifically the Quantum Design MPMS-XL5, was used in the Magnetometry laboratory of the Physics Department at the University of Parma. SQUID magnetometers are known for their extremely high sensitivity, making them ideal for measuring tiny magnetic moments. They detect changes in magnetic flux created by mechanically moving the sample through a superconducting pick-up coil, which is then converted to a voltage proportional to the sample's magnetization. In this thesis, iso-field magnetization curves ($M(T)$) as a function of temperature were measured between 400 K and 6 K at a constant sweep rate of 2 K/min

5.5 Thermomagnetic tester

The TM motor prototype designed to test TM materials under operational conditions, developed at the Physics Department at the University of Parma, belongs to the category of "Curie wheels." The TM tester primarily consists of three components: (1) a rotor made of TM material with cylindrical symmetry, (2) a controlled heat source, and (3) an assembly of permanent magnets generating a magnetic field gradient with a maximum field of $\mu_0 H = 0.65$ T.

Figure 5-4 shows a map of the magnetic field generated by the permanent magnet array used. The measurement was performed using a SENIS 3DHALL, which is a CMOS-integrated magnetic field sensor that allows for the acquisition of all three magnetic field components (Bx, By, and Bz) simultaneously and at the same location. The sensor incorporates three groups of mutually orthogonal Hall-effect elements (one horizontal and two vertical) with biasing circuits and amplifiers for each.

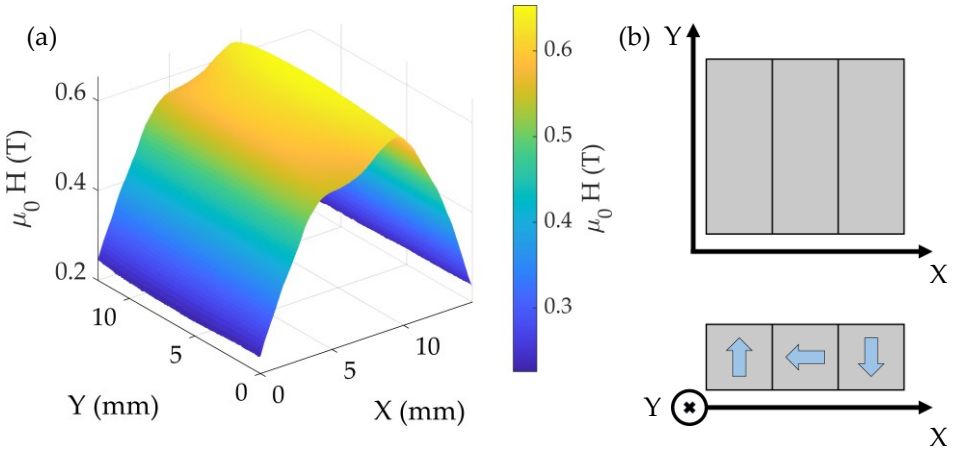

***Figure 5-4**: (a) Surface $\mu_0 H(X,Y)$ of the set of permanent magnets mounted on TM tester measured at a distance of 1 mm from the magnets. (b) scheme of the set. The light blue arrows represent the direction of the magnetic axes of each permanent magnets.*

In Figure 5-5 (a-b) are presented a photograph and a sketch of TM tester. The rotor is partially immersed in warm water at temperature T_{hot}, simulating the heat source, and exposed to the magnetic field gradient. Heat exchanges between the rotor and the heat source, as well as with the environment at temperature T_{cold}, create an angular temperature gradient within the rotor $T(\theta)$.

As a result, the magnetic moment of the rotor and the magnetic interaction force with the field gradient vary with the angular position ($m(\theta)$, $F(\theta)$). The appropriate combination of temperature and field gradients on the rotor generates a torque, derived from the sum of tangential magnetic forces acting on each angular sector. Each sector is characterized by a magnetic moment $m(\theta)$ and subjected to a field gradient in the tangential direction $\partial H(\theta)/\partial u_t$.

$$\vec{\tau}_{net} = \left(\mu_0 \int_0^{2\pi} M(H,T,\theta) \frac{1}{R} \frac{\partial H(\theta)}{\partial u_t} d\theta \right) \vec{u}_t \times \vec{R} \qquad (5.2)$$

The radius vector of the rotor is denoted as $\vec{R}$. It is interesting to note that the part within the parentheses in Eq. 5.2 represents the magnetic force experienced by a magnetic material when subjected to a magnetic field gradient. This force is depicted by the yellow arrows in Figure 5-5 (c).

This torque causes the rotor to rotate, thereby converting thermal energy into mechanical energy. The temperature of the warm source can be adjusted within the range of 290K - 355K and is stabilized with an error margin of 0.5 K. The water level can be adjusted to change the relative position between the thermal and magnetic gradients. The part of the rotor not immersed in water can be exposed to the room environment or to a controlled flow of thermostated air within the 280-300K temperature range.

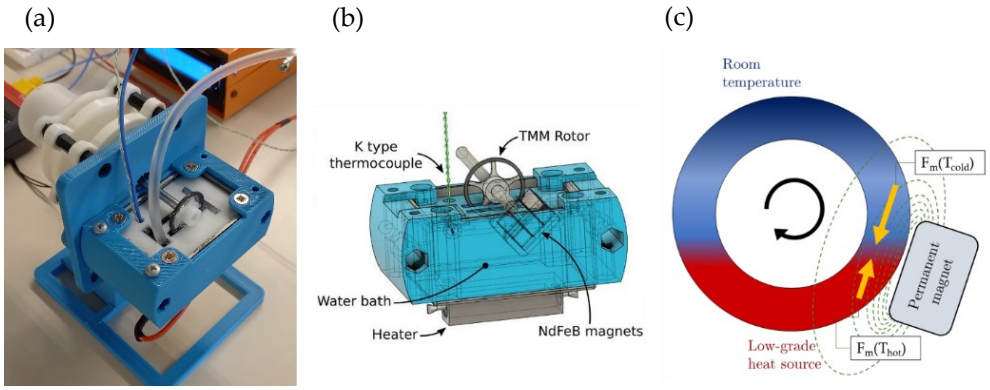

***Figure 5-5**: (a) Photograph and (b) technical scheme of the small-scale TM motor prototype utilized for testing materials. (c) A schematic of the rotor immersed in a magnetic field (depicted with green dashed lines) and in contact with thermal sources. Red and blue areas illustrate the temperature gradient on the rotor. Magnetic forces are represented by yellow arrows.*

The rotor shaft is connected to a custom-designed two-phase electric motor, which allows for the measurement of the TM motor's angular speed and torque. A calibration procedure, involving the application of a known torque to the shaft, was used to determine the constants of the electric generator and to measure the friction torque of the TM motor (details are provided in the Appendix 8.1). To determine the overall torque generated by the TM motor, all torque data collected during materials testing were corrected for the measured friction torque values. Additionally, a controlled electronic load was used to assess the TM motor's performance by adjusting the external load. Integrated software enables continuous measurement of

the TM motor's mechanical output and monitors the temperatures of the cold and hot reservoirs.

5.6 Morphological and structural characterizations

For the morphological analysis and measurement of the compositions of the synthesized alloys, a Bruker Esprit microanalysis on a FEG-ESEM FEI QUANTA 250 was used at CNR-IMEM institute.

For structural characterization, some samples were analyzed at the Department of Chemistry of the University of Parma, while others were analyzed at the University of Lorraine in Nancy, France.

The crystal structure of the samples was analyzed by X-ray diffraction (XRD) on powdered specimens. X-ray diffraction is one of the most crucial non-destructive techniques for characterizing the crystallographic structure of powders and crystals.

For the analysis conducted at the university of Parma, diffraction measurements were conducted using a Rigaku SmartLab diffractometer equipped with a yPix-3000 solid-state detector, a fine-focus filament, and operating at 1.2 kW of power. While for the measurements conducted at the university of Lorraine a Bruker D8 Advance was used.

Analyses on the powdered samples were performed at room temperature in Bragg-Brentano geometry (the standard geometry for powder measurements), using radiation from a Cu source (considering both $K\alpha_1$ and $K\alpha_2$ components).

6 Results

In this thesis, the synthesis and characterization of various materials for potential magnetocaloric and thermomagnetic applications will be described. As mentioned in Section 3.3, the materials used belong to the subclass of NiMn-based Heusler alloys and High-Entropy Alloys (HEAs). Given the particularly large number of samples and sample sets produced in this work, a table is provided below indicating the nominal compositions, the synthetic names by which they will be referred to, and the section where the motivations and the initial magnetic characterization are presented.

Nominal composition	Code name	Section
$Ni_{48}Mn_{36}Sn_{16}$	TM-Sn	6.1.1.1
$Ni_{48}Mn_{36}In_{16}$	TM-In	6.1.1.1
$Ni_{50}Mn_{18}Cu_{6}Ga_{25}$	TM-CuGa	6.1.1.1
$Ni_{50}Mn_{34}Sn_{16}$	Ni/Mn-x0	6.1.1.2
$Ni_{48}Mn_{36}Sn_{16}$ (*)	Ni/Mn-x2	6.1.1.2
$Ni_{46}Mn_{38}Sn_{16}$	Ni/Mn-x4	6.1.1.2
$Ni_{44}Mn_{40}Sn_{16}$	Ni/Mn-x6	6.1.1.2
$Ni_{42}Mn_{42}Sn_{16}$	Ni/Mn-x8	6.1.1.2
$Ni_{48}Mn_{36}Sn_{16}$ (*)	Sub-Fe0	6.1.1.3
$Ni_{48}Mn_{34}Sn_{16}Fe_{2}$	Sub-Fe2	6.1.1.3
$Ni_{48}Mn_{32}Sn_{16}Fe_{4}$	Sub-Fe4	6.1.1.3
$Ni_{48}Mn_{30}Sn_{16}Fe_{6}$	Sub-Fe6	6.1.1.3
$Ni_{48}Mn_{28}Sn_{16}Fe_{8}$	Sub-Fe8	6.1.1.3
$Ni_{48}Mn_{26}Sn_{16}Fe_{10}$	Sub-Fe10	6.1.1.3
$Ni_{50}Mn_{35}Sn_{15}$	Add-Pb0	6.1.1.4
$(Ni_{50}Mn_{35}Sn_{15})_{99}Pb_{1}$	Add-Pb1	6.1.1.4
$(Ni_{50}Mn_{35}Sn_{15})_{98}Pb_{2}$	Add-Pb2	6.1.1.4
$(Ni_{50}Mn_{35}Sn_{15})_{97}Pb_{3}$	Add-Pb3	6.1.1.4

$(Ni_{50}Mn_{35}Sn_{15})_{96}Pb_4$	Add-Pb4	6.1.1.4
$Fe_{27}Ni_{27}Ga_{13}Mn_{22}Si_{11}$	HEA-Ga13	6.2.1
$Fe_{27}Ni_{27}Ga_{11}Mn_{24}Si_{11}$	HEA-Ga11	6.2.1

***Table 1**: List of samples synthesized and characterized in this thesis. The first column presents the nominal compositions of the alloys, the second column contains the names by which the samples will be referenced throughout the thesis, and the third column indicates the section number where the characterization of the samples is presented. Nominal compositions followed by an asterisk refer to the same sample used in multiple sets.*

This section is divided into two sub-sections (6.1 and 6.2), where NiMn-based Heusler compounds and High Entropy Alloys are analysed, respectively. All samples were synthesized via arc melting using the methods described in Section 4.1, and subsequently heat-treated using the tube furnace shown in Section 4.2. Each subsection includes an initial part where the main magnetic characterizations of the different sets of samples, such as magnetization and magnetic susceptibility measurements as a function of temperature, will be presented. Appendix 8.3 includes a table detailing the mass loss for each melting process of all the samples discussed in this thesis.

6.1 NiMn-based Heusler Alloys

As outlined in Section 3.3.1, NiMn-based Heusler alloys hold great promise for thermomagnetic and magnetocaloric applications. However, predicting a material's performance in advance is often challenging and may not fully reflect its practical potential. To address this, Section 6.1.1.1 will detail the characterization of three Heusler alloys (NiMnSn, NiMnIn, and NiMnCuGa), which will undergo direct measurements of their thermomagnetic properties using the device described in Section 5.5.

A key feature of these magnetic materials is the ability to fine-tune their critical temperatures by altering alloy compositions. This thesis will explore three tuning methods: varying the Ni/Mn ratio, as discussed in Section 6.1.1.2; substituting a fourth element (Fe) in place of Mn, covered in Section 6.1.1.3; and introducing a fourth element (Pb) while preserving the primary alloy composition, as described in Section 6.1.1.4.

The evaluation of the three tuning methods will be conducted using a NiMnSn alloy, despite the fact that, as will become evident in Section 6.1.1.1, the magnetic

properties of the In-based alloy are superior and exhibit similar magnetic transition temperature. This choice is justified by the lower criticality of Sn compared to In. Sn is, in fact, significantly more cost-effective than In [147] and considerably more abundant in the continental's crust [148].

6.1.1 Heusler characterization

6.1.1.1 NiMn(In,Sn) - NiMnCuGa

Three Heusler alloys, $Ni_{48}Mn_{36}Sn_{16}$ (TM-Sn), $Ni_{48}Mn_{36}In_{16}$ (TM-In), $Ni_{50}Mn_{19}Cu_6Ga_{25}$ (TM-CuGa), were synthesized. After synthesis, the samples were annealed at 1073 K for 72 hours and subsequently quenched in water. The compositions of the samples were analyzed using energy dispersive X-ray spectroscopy (EDX) described in Section 5.6. All measured compositions were found in agreement with the nominal values, within a margin of experimental error of less than 1%.

Figure 6-1 presents low-field magnetic susceptibility measurements (1 mT) as a function of temperature, measured on heating using the TMA. The results show a single magnetic phase, with all three samples exhibiting a clear and sharp Curie transition within the useful range for low-temperature thermomagnetic applications. The identification of critical temperatures was achieved by calculating the minimum of the first derivative of the magnetic susceptibility with respect to temperature. The detailed process is described in Appendix 8.3. The TM-Sn and TM-In samples display only a second-order transition at 323 K and 316 K, respectively in accordance with the literature [149]. In contrast, the TM-CuGa sample exhibits two magnetic transitions, one at 273 K towards a phase with higher susceptibility on heating, the other, being the Curie transition of the sample, at 301 K.

Figure 6-2 presents the isofield magnetization measurements as a function of temperature for the three samples. These measurements were performed using the extraction magnetometer described in Section 5.2, covering a temperature range between 100 K and 340 K. The results for the TM-Sn and TM-In samples are consistent with the findings in the literature [149], [150], showing approximately a 25% reduction in magnetization when Sn completely replaces In in the $Ni_{48}Mn_{36}(In,Sn)_{16}$ alloy. In these measurements, the low temperature transition of the TM-CuGa sample around 275 K, observed also in Fig.6-1, can be definitively identified as a martensitic transformation, as it is clearly visible thanks to measurements performed while cooling the sample, represented by the dashed line.

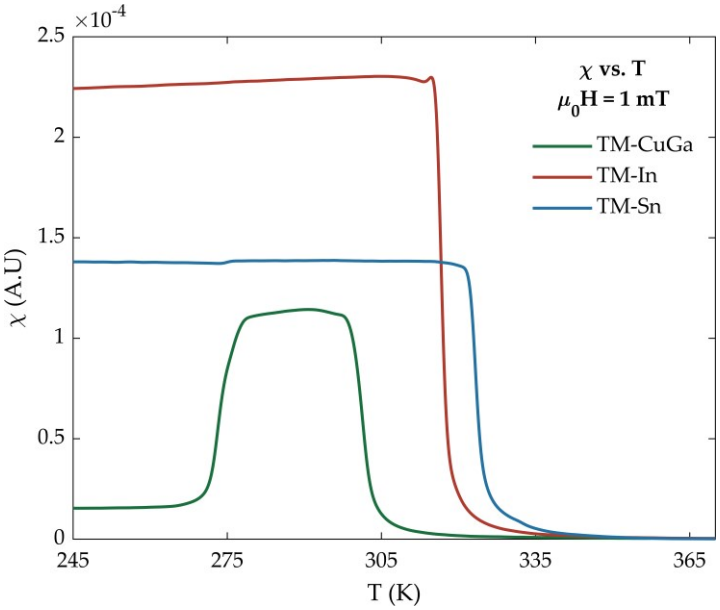

***Figure 6-1**: ac magnetic susceptibility in low applied magnetic field of 1 mT as a function of temperature for the samples: $Ni_{48}Mn_{36}Sn_{16}$ (blue), $Ni_{48}Mn_{36}In_{16}$ (red), and $Ni_{50}Mn_{19}Cu_6Ga_{25}$ (green).*

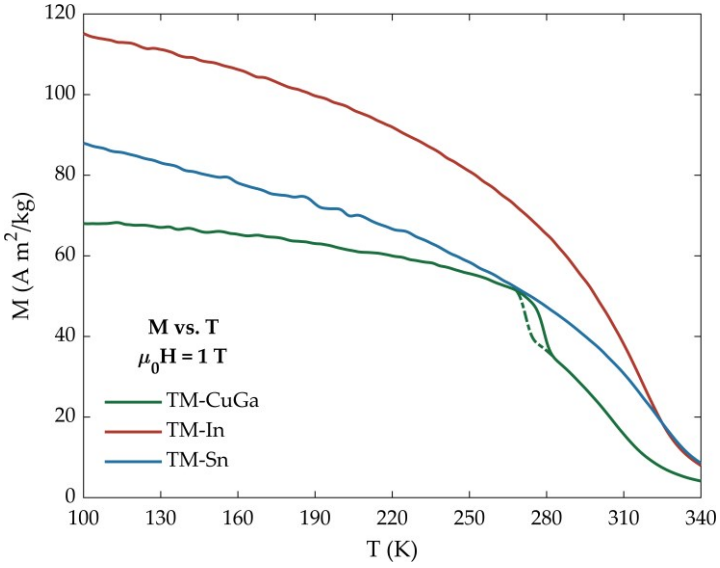

***Figure 6-2**: Isofield magnetization curves as a function of temperature in 1T applied magnetic field for the alloys: $Ni_{48}Mn_{36}Sn_{16}$ (blue), $Ni_{48}Mn_{36}In_{16}$ (red), and $Ni_{50}Mn_{19}Cu_6Ga_{25}$ (green). The dashed green line represents the portion of the cooling magnetization curve of the TM-CuGa sample.*

The thermal hysteresis accompanying the martensitic transition was calculated to be 6 K. The data show a significant superiority in magnetization for the TM-In sample compared to the other two, confirming numerous findings in the literature [149]. The magnetization values measured at 100 K and the Curie temperatures of the three samples in this set are summarized in table 6-2.

A series of isothermal M(H) measurements were taken at different temperatures within the operational range of a TM generator, designed to harvest low-grade waste heat (290-380 K). The isothermal curves are showed in Figure 6-3 and they are obtained using the stationary pendulum magnetometer described in 5.3. These measurements are used to determine the maximum magnetic work per unit mass, chosen as FoM for this thesis, that the TM material can generate during a TM cycle. According to Eq. 3.15, the magnetic work of the cycle is represented by the area enclosed between two isothermal M(H) curves at temperatures T_{hot} and T_{cold} over the field range H_0 - H_1.

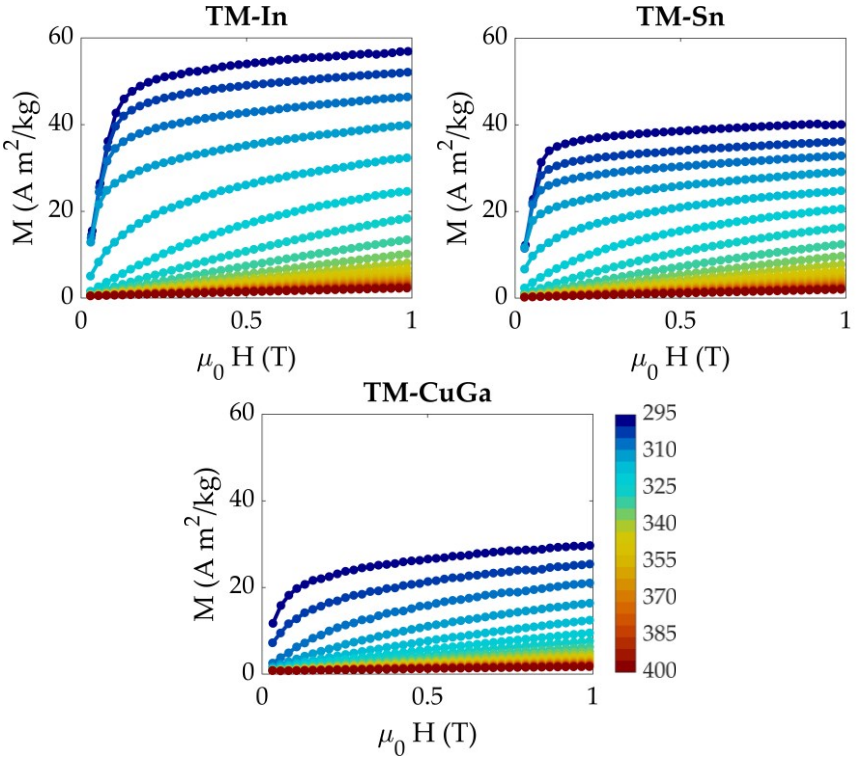

***Figure 6-3**: Isothermal magnetization curves as a function of external magnetic field collected from 297K to 402K every 5K for the TM-In, TM-Sn and TM-CuGa samples.*

Table 6-2 provides a summary of the key magnetic properties essential for TM generation applications of the studied Heusler materials. Both the finite change in magnetization over a 4 K temperature range around the Curie temperature (ΔM_{4K}) and the maximum derivative of high-field magnetization with respect to temperature ($\partial M/\partial T_{Tc}$) show a trend consistent with the alloys' saturation magnetization. These parameters are relevant for an initial assessment of the thermomagnetic potential of TM materials, as they describe the sharpness of the magnetic transition. They are proportional to the pointwise change in magnetization, in the case of dM/dT, and over a temperature range, in the case of ΔM_{4K}. The choice to evaluate the change in magnetization over a 4K temperature range is based on the fact that this range is considered realistic, as discussed in Section 6.1.2.

Sample	Composition	T_C (K)	M_{100K} ($Am^2 kg^{-1}$)	$\partial M/\partial T_{Tc}$ ($Am^2 kg^{-1}K^{-1}$)	ΔM_{4K} ($Am^2 kg^{-1}$)
TM-CuGa	$Ni_{50}Mn_{18}Cu_6Ga_{25}$	301	68.0	0.81	3.2
TM-In	$Ni_{48}Mn_{36}In_{16}$	317	115.2	1.38	5.5
TM-Sn	$Ni_{48}Mn_{36}Sn_{16}$	323	87.9	0.89	3.5

***Table 2**: A summary table of the results obtained from the characterization of the TM-NiMn-based set is presented. In the first column (sample), the names of the samples used are listed, as summarized in Table 6-1. The second column (composition) reports the compositions of the samples. The third column (T_C) shows the Curie temperature measurements obtained from low-field magnetic susceptibility measurements. In the fourth column (M_{100K}), the magnetization value at T = 100K is calculated from magnetization measurements. The fifth column ($\partial M/\partial T_{Tc}$) reports the maximum absolute value of the derivative of the magnetization curve with respect to temperature, in all samples. Finally, the sixth column (ΔM_{4K}) provides the difference in magnetization calculated over a temperature range of 4K around the Curie temperature of the sample.*

6.1.1.2 NiMnSn varying the ratio Ni/Mn

A NiMnSn-based alloy set has been synthesized, where the composition is varied by altering the stoichiometric ratio of Ni and Mn while keeping constant the amount of Sn. Specifically, the set under investigation has the following composition: $Ni_{50-x}Mn_{34+x}Sn_{16}$ (x= 0, 2, 4, 6, 8).

The samples were melted while maintaining the current from the arc melter electrode below 50 A to minimize manganese loss due to evaporation. Each sample was melted three times, with the samples being flipped after each melting to enhance the homogeneity of the alloys. After each melting, the arc melter chamber was opened for cleaning and to monitor the mass of the samples between melts. After the synthesis samples were heat treated for 72 hours at 1073 K.

The rationale for studying this set is twofold. First, as mentioned previously, the ability to fine-tune the Curie temperature by slightly modifying the alloy composition offers a significant advantage for applications where critical temperatures play a crucial role. Second, the Sn-based Heusler alloy serves as a much more cost-effective and less resource-critical alternative to its In-based counterpart. However, the NiMnSn alloy is characterized by lower magnetization values compared to the In-based version. Thus, it is worth to explore various compositions within the NiMnSn alloy system to identify a configuration that maximizes magnetization.

Figure 6-4 presents the magnetic susceptibility measurements as a function of temperature conducted with the TMA with an applied ac magnetic field of 1 mT. All samples were evaluated over the same temperature range (200 K to 400 K) under heating conditions.

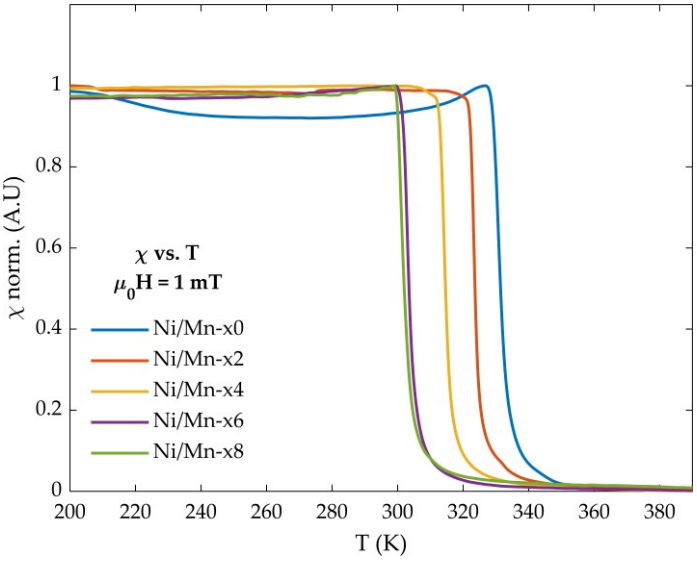

***Figure 6-4**: ac magnetic susceptibility in low applied magnetic field of 1 mT as a function of temperature for the samples: $Ni_{50}Mn_{34}Sn_{16}$ (blue), $Ni_{48}Mn_{36}Sn_{16}$ (orange), $Ni_{46}Mn_{38}Sn_{16}$ (yellow), $Ni_{44}Mn_{40}Sn_{16}$ (purple), and $Ni_{42}Mn_{42}Sn_{16}$ (green).*

The ferromagnetic-to-paramagnetic Curie transitions are clearly visible and sharp, indicating good compositional homogeneity from a magnetic standpoint. The results of this analysis demonstrate excellent tunability of the alloy, showing a clear correlation between increasing manganese content in the alloy and a decrease in the Curie temperature.

The magnetization curves as a function of temperature are shown in Figure 6-5. The measurements were performed using an extraction magnetometer with an applied magnetic field up to 1T. As in previous cases, the measurements were conducted under heating conditions, starting from 100 K and reaching the maximum temperature allowed by the magnetometer, 340 K. The heating rate for each measurement was 2 K per minute.

The stoichiometric percentage of Mn corresponding to the critical concentration is dependent on the specific alloy composition under investigation. Experimentally, in the case of the $Ni_{50-x}Mn_{34+x}Sn_{16}$ series, the maximum magnetization is achieved at x=2, corresponding to the $Ni_{48}Mn_{36}Sn_{16}$ alloy. Consequently, this composition was selected both for the TM analysis discussed in Section 6.1.1.1, and as the base composition for developing additional material sets, as detailed in Section 6.1.1.3.

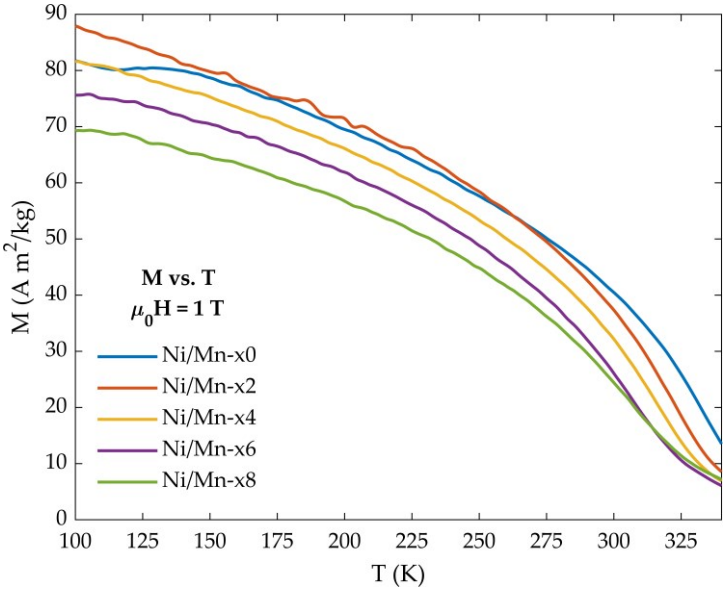

***Figure 6-5**: magnetization in applied magnetic field of 1 T as a function of temperature for the samples: $Ni_{50}Mn_{38}Sn_{16}$ (blue), $Ni_{48}Mn_{36}Sn_{16}$ (orange), $Ni_{46}Mn_{38}Sn_{16}$ (yellow), $Ni_{44}Mn_{40}Sn_{16}$ (purple), and $Ni_{42}Mn_{42}Sn_{16}$ (green).*

Figure 6-6 illustrates the results of the magnetic characterization. In blue, the upper portion of the figure shows the Curie temperatures, determined by identifying the peaks of the temperature derivatives from the curves presented in Figure 6-4. In red, in the bottom of the figure, the magnetization values at T=100 K, obtained from the measurements shown in Figure 6-5, are plotted. These two graphs effectively summarize the key findings of this study: the ability to fine-tune the Curie temperature by adjusting the Ni/Mn ratio, and the identification of the critical Mn concentration that yields the maximum magnetization for these compositions.

As a general trend, it is observed that Curie temperatures decrease with the decrease of $L2_1$ ordering, due to changes in the magnetic moment of the alloys, which are influenced by the Mn atom occupancy on the various lattice sites. These atoms couple antiferromagnetically when they are nearest neighbours (Mn atoms on Sn sites) and ferromagnetically when they are next-nearest neighbours (Mn atoms in the Mn sublattice) [151], [152], [153].

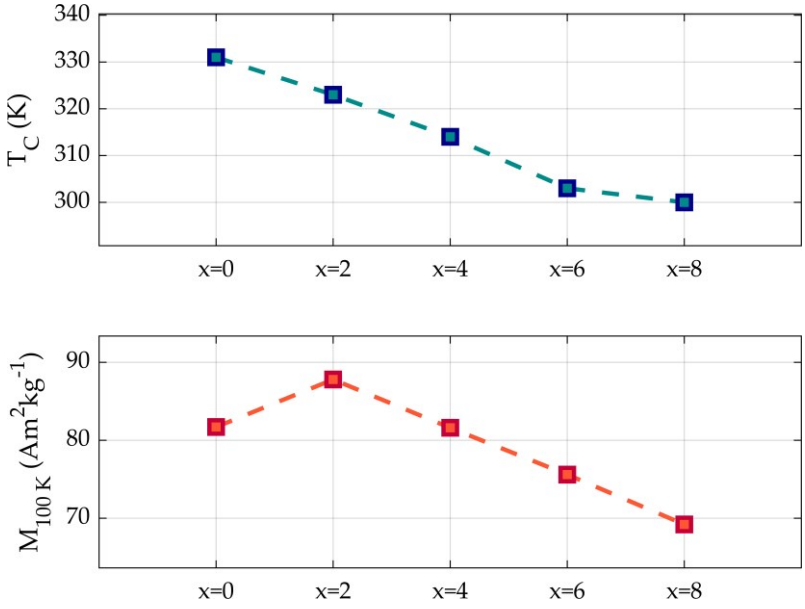

***Figure 6-6**: TC values (top blue) and magnetization at T=100K (bottom red) of the set $Ni_{50-x}Mn_{43+x}Sn_{16}$ on function of the values of x. TC values are calculated using the temperature derivates of the magnetic susceptibility and M_{100K} are obtained by the magnetization curves.*

The compositions of the samples were examined using EDX spectroscopy within a SEM (section 5.6). The results showed that all measured compositions were consistent with the nominal values, with an experimental error margin of less than

1%. A summary table (Tab. 6-3) of the magnetic properties of the set is provided below.

Sample	Composition	T_C (K)	M_{100K} ($Am^2 kg^{-1}$)	$\partial M/\partial T_{Tc}$ ($Am^2 kg^{-1}K^{-1}$)	ΔM_{4K} ($Am^2 kg^{-1}$)
Ni/Mn-x0	$Ni_{50}Mn_{34}Sn_{16}$	330	81.7	0.87	3.4
Ni/Mn-x2	$Ni_{48}Mn_{36}Sn_{16}$	323	87.9	0.89	3.5
Ni/Mn-x4	$Ni_{46}Mn_{38}Sn_{16}$	314	81.6	0.80	3.2
Ni/Mn-x6	$Ni_{44}Mn_{40}Sn_{16}$	303	75.6	0.71	2.8
Ni/Mn-x8	$Ni_{42}Mn_{42}Sn_{16}$	300	69.2	0.64	2.5

***Table 3**: summary table of the results obtained from the characterization of the $Ni_{50-x}Mn_{34+x}Sn_{16}$ set is presented. In the first column (sample), the names of the samples used are listed, as summarized in Table 6-1. The second column (composition) reports the compositions of the samples. The third column (T_C) shows the Curie temperature measurements obtained from low-field magnetic susceptibility measurements. In the fourth column ($M_{100\ K}$), the magnetization value at T = 100 K is calculated from magnetization measurements. The fifth column ($\partial M/\partial T_{Tc}$) reports the maximum absolute value of the derivative of the magnetization curve with respect to temperature. Finally, the sixth column ($\Delta M_{4\ K}$) provides the difference in magnetization calculated over a temperature range of 4 K around the Curie temperature of the sample.*

6.1.1.3 Partial substitution of Fe to NiMnSn compounds

In this section a new set based on the partial substitution of Mn by Fe is presented, using the starting composition: $Ni_{48}Mn_{36}Sn_{16}$, where, as described above, a maximum of ΔM has been observed. Several studies on NiMnSn Heusler compounds have explored the impact of Fe doping on their magnetic, structural, and magnetocaloric properties [154], [155], [156]. However, these investigations have primarily focused on the magnetocaloric performance around the martensitic transformation, with limited attention given to the Curie transition. The primary objective of this work is to achieve precise control of the Curie transition temperature in austenitic NiMnSn based Heusler compounds, while maintaining their magnetocaloric and thermomagnetic properties.

The series produced consists of six samples with the composition $Ni_{48}Mn_{36-x}Sn_{16}Fe_x$. The alloys were synthesized using arc melting, with the electrode current increased up to a maximum of 60 A. As with previous cases, the melting process was divided into three sessions, during which the samples were flipped and weighed between each session. After the melting process, the synthesized alloys underwent a 72-hour heat treatment at 1173 K. The decision to raise the heat treatment temperature by 100 K was based on literature on this type of Heusler alloy, which highlighted issues with compositional homogeneity and the tendency to form iron-rich secondary phases [108].

Figure 6-7 shows the magnetic susceptibility measurements as a function of temperature, conducted using a TMA with an applied magnetic field of 1 mT. The measurements were performed by slowly increasing the temperature within the range of 200 K to 400 K, where all six samples exhibited clear and sharp Curie transitions.

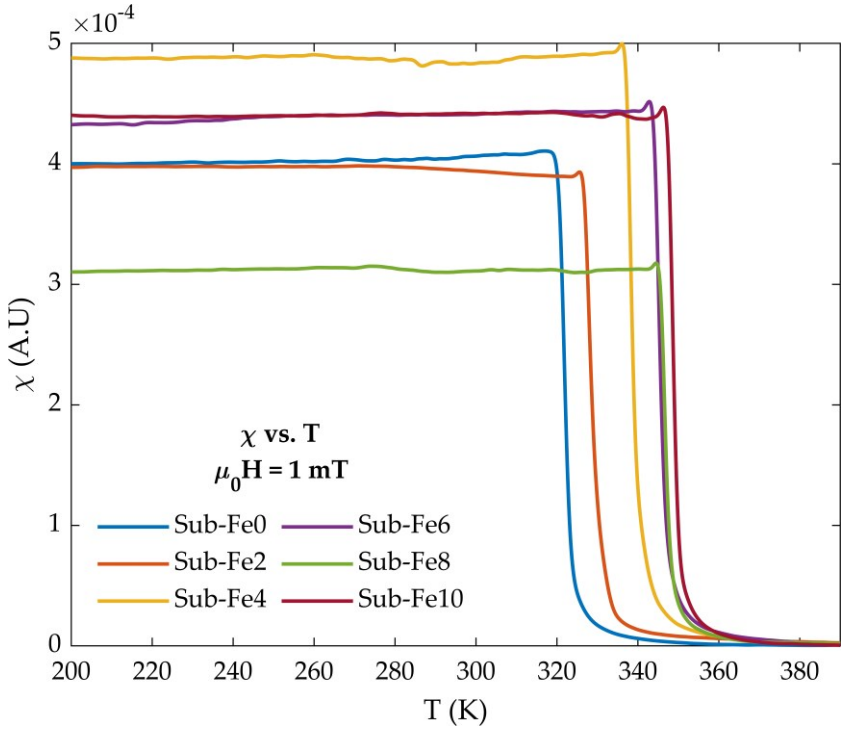

***Figure 6-7**: ac magnetic susceptibility in low applied magnetic field of 1 mT as a function of temperature for the samples: $Ni_{48}Mn_{36}Sn_{16}$ (blue), $Ni_{48}Mn_{34}Sn_{16}Fe_2$ (orange),*

$Ni_{48}Mn_{32}Sn_{16}Fe_4$ (yellow), $Ni_{48}Mn_{30}Sn_{16}Fe_6$ (purple), $Ni_{48}Mn_{28}Sn_{16}Fe_8$ (green), and $Ni_{48}Mn_{26}Sn_{16}Fe_{10}$ (magenta).

TMA measurements indicate that increasing the Fe content in the alloy leads to a rise in the Curie temperature, highlighting the potential to precisely control the para-to-ferromagnetic transition through partial Fe substitution.

Figure 6-8 displays the magnetization measurements as a function of temperature, carried out using an extraction magnetometer under an applied magnetic field of 1 T. As with the previous magnetization measurements, the temperature was increased at a rate of 2 K/min, starting from 100 K and reaching 340 K. Unfortunately, most of the Fe-substituted samples exhibit Curie temperatures that exceed the magnetometer's temperature limit, preventing full observation of the para-to-ferromagnetic transition in the magnetization curves.

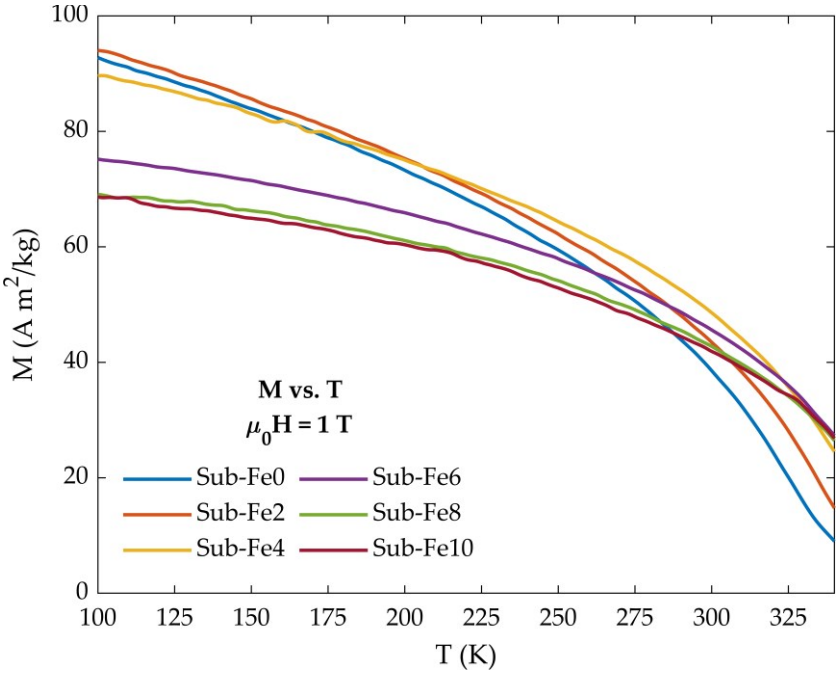

***Figure 6-8**: magnetization in applied magnetic field of 1 T as a function of temperature for the samples: $Ni_{48}Mn_{36}Sn_{16}$ (blue), $Ni_{48}Mn_{34}Sn_{16}Fe_2$ (orange), $Ni_{48}Mn_{32}Sn_{16}Fe_4$ (yellow), $Ni_{48}Mn_{30}Sn_{16}Fe_6$ (purple), $Ni_{48}Mn_{28}Sn_{16}Fe_8$ (green), and $Ni_{48}Mn_{26}Sn_{16}Fe_{10}$ (magenta).*

From the data in figure 6-8, a decrease in magnetization is observed with increasing nominal Fe content in the alloys. This finding contrasts with results reported in similar studies [108], [156].

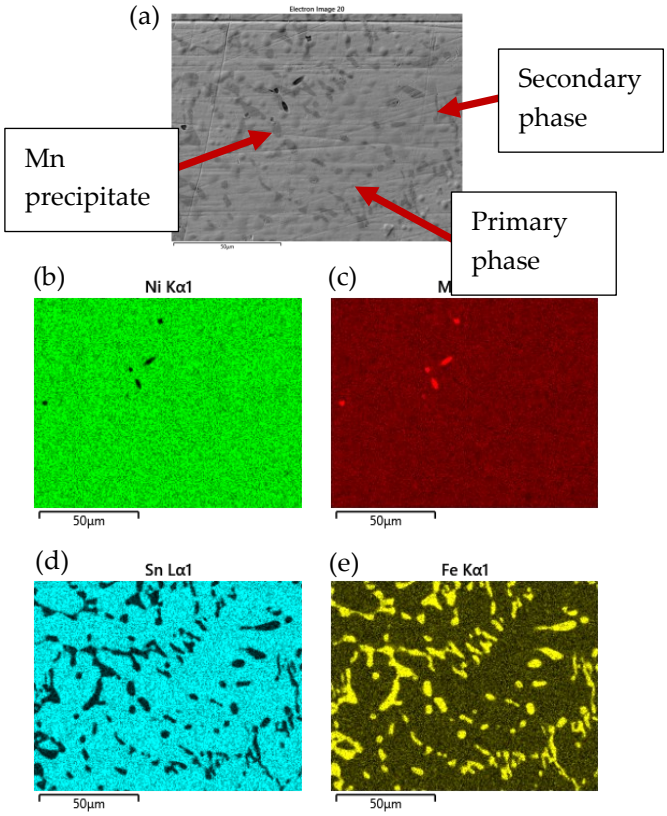

***Figure 6-9**: (a) SEM image of the sample Sub-Fe8, (b, c, d, e) EDX compositional maps showing with different colour the distribution of each element Mn, Ni, Sn and Fe respectively.*

This discrepancy can be explained by examining the EDX images obtained using the SEM, as described in Section 5.6. The analyses show that as the iron content increases, distinct secondary phases form, characterized by a composition rich in Fe and poor in Sn. Figure 6-9 presents an example of an EDX map conducted on a selected region of the Sub-Fe8 sample. This analysis highlights the presence of both the NiMnFe secondary phase (represented by dark grey areas) and manganese precipitates (depicted as black regions).

Figure 6-10 shows the SEM images of all samples, where it can be observed that the Sub-Fe0 and Sub-Fe2 samples are single phase. In the Sub-Fe4 sample, the secondary

phase begins to form, while in the Sub-Fe6, Sub-Fe8, and Sub-Fe10 samples, the presence of the NiMnFe phase becomes increasingly pronounced.

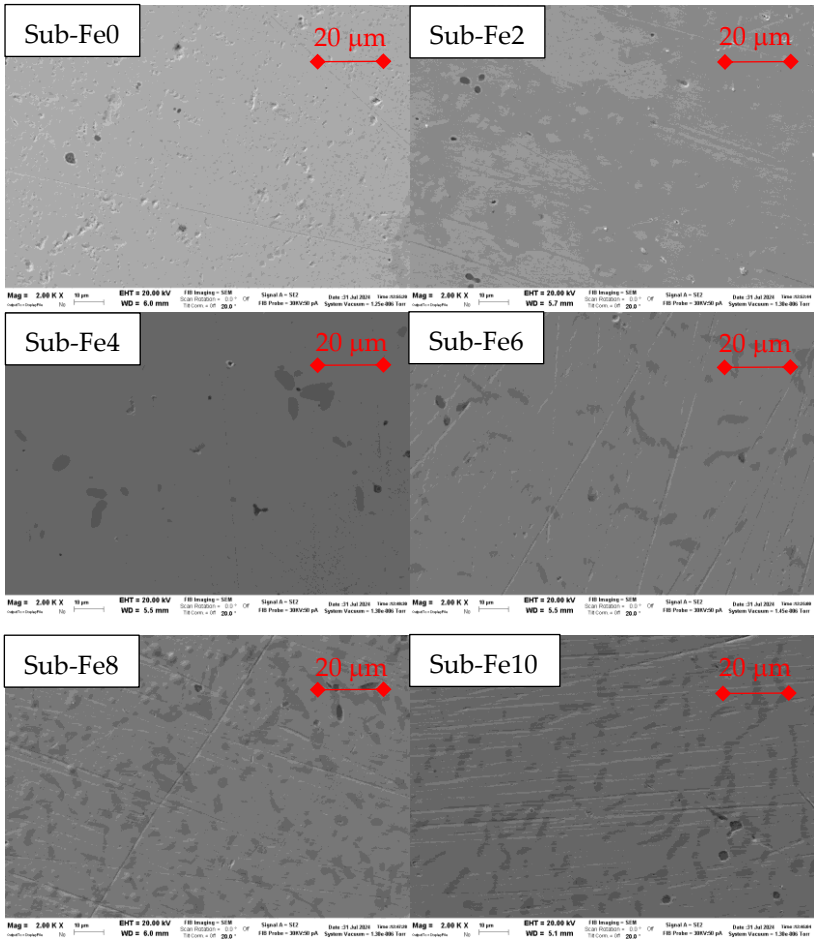

***Figure 6-10**: SEM images of the set of nominal composition $Ni_{48}Mn_{36-x}Sn_{16}Fe_x$. The secondary Fe-rich and Sn-poor NiMnFe phases are the dark grey ones, while the black dots are Mn precipitates. It is noteworthy that this inhomogeneity was not detected in the magnetic susceptibility measurements, which, due to the high sensitivity of TMA, would typically manifest as Curie transitions with distinct slopes or incomplete suppression of the signal following the Curie transition of the primary phase. Please note that the visible contrast in the Sub-Fe2 image does not depend on the presence of a secondary phase but rather on the presence of an isopropanol halo used for cleaning the samples, which was not properly dried.*

Following the EDX analyses, a table that lists the measured compositions of both the primary phases and, where applicable, the secondary phases, is provided (Tab. 6-4). The table also includes the key magnetic properties of the series under investigation.

Sample	Composition	T_C (K)	$M_{100\,K}$ ($Am^2\,kg^{-1}$)	$\partial M/\partial T_{Tc}$ ($Am^2\,kg^{-1}K^{-1}$)	$\Delta M_{4\,K}$ ($Am^2\,kg^{-1}$)
Sub-Fe0	$Ni_{47.3}Mn_{36.4}Sn_{16.3}$	323	92.7	0.89	3.5
Sub-Fe2	$Ni_{48.1}Mn_{34.5}Sn_{15.5}Fe_{1.9}$	328	94.0	0.96	3.4
Sub-Fe4 2nd phase	$Ni_{47.0}Mn_{32.9}Sn_{16.9}Fe_{3.2}$ $Ni_{44.7}Mn_{32.9}Sn_{2.4}Fe_{20.0}$	338	89.6	0.82	3.2
Sub-Fe 6 2nd phase	$Ni_{47.1}Mn_{30.8}Sn_{18.5}Fe_{3.6}$ $Ni_{45.7}Mn_{30.1}Sn_{2.8}Fe_{21.4}$	345	75.2	-	-
Sub-Fe 8 2nd phase	$Ni_{47.2}Mn_{29.1}Sn_{20.3}Fe_{3.4}$ $Ni_{44.5}Mn_{26.0}Sn_{2.1}Fe_{27.4}$	346	69.1	-	-
Sub-Fe 10 2nd phase	$Ni_{47.5}Mn_{27.2}Sn_{20.8}Fe_{4.5}$ $Ni_{45.8}Mn_{23.6}Sn_{3.1}Fe_{27.5}$	348	68.6	-	-

***Table 4**: A summary table of the results obtained from the characterization of the $Ni_{48}Mn_{36-x}Sn_{16}Fe_x$ set is presented. In the first column (sample), the names of the samples used are listed. The second column (composition) reports the compositions of the samples measured via EDX analysis. The third column (T_C) shows the Curie temperature measurements obtained from low-field magnetic susceptibility measurements. In the fourth column (M_{100K}), the magnetization value at T = 100K is calculated from magnetization measurements. The fifth column ($\partial M/\partial T_{Tc}$) reports the maximum absolute value of the derivative of the magnetization curve with respect to temperature. Finally, the sixth column (ΔM_{4K}) provides the difference in magnetization calculated over a temperature range of 4K around the Curie temperature of the sample. For samples with a Curie transition occurring above 340K, the values for $\partial M/\partial T_{Tc}$ and ΔM_{4K} are not provided, as the necessary magnetization data corresponds to temperatures beyond the operational limits of the magnetometer.*

The compositions measured via EDX, presented in Table 6-4, provide a compelling explanation for the discrepancy observed between the clear detection of secondary phases in SEM images and the seemingly single-phase behavior indicated by the TMA data. Additionally, these compositions offer insight into the observed trend in magnetization, measured using a magnetometer, which, contrary to expectations

based on prior literature [157], decreases with increasing nominal iron content in the alloy.

The explanation for these counterintuitive results lies in the nature of the secondary phase, which has been identified as antiferromagnetic [158]. The antiferromagnetic character of the $Ni_{50}Mn_{25}Fe_{25}$ secondary phase accounts for its absence in magnetic susceptibility measurements and also explains the reduction in magnetization observed during magnetometer analysis. This reduction is particularly evident when considering that the magnetization curves, as depicted in Figure 6-8, are normalized per unit mass. Since the total mass of the sample includes the antiferromagnetic secondary phase, the overall magnetization values are effectively diminished by the presence of this non-magnetic component.

Figure 6-11 presents the results obtained from the magnetic characterization described earlier. The blue points in the upper part of the image represent the Curie temperatures, calculated by identifying the peaks in the temperature derivatives of the TMA curves (Fig. 6-7). The red points correspond to the magnetization values of the samples at T=100 K, as obtained from the measurements shown in Figure 6-8. The T_C graph illustrates the ability to fine-tune the Curie temperature, even though the substitution of Fe for Mn was not entirely successful. However, upon examining the composition values presented in the table, an increase in Sn content at the expense of Mn in the alloy is evident. This compositional shift suggests that fine-tuning the critical Curie temperature can also be achieved by adjusting the Sn/Mn ratio in the alloy.

Furthermore, this series extends the range of Tc values up to 350 K, which falls within a critical temperature range for thermomagnetic applications that had not been reached by the previously discussed series.

The magnetization data presented in Figure 6-11 provide a clearer depiction of the drop in magnetization, which initiates in the Sub-Fe4 sample, corresponding to the onset of secondary phase formation, and persists through to the Sub-Fe10 sample

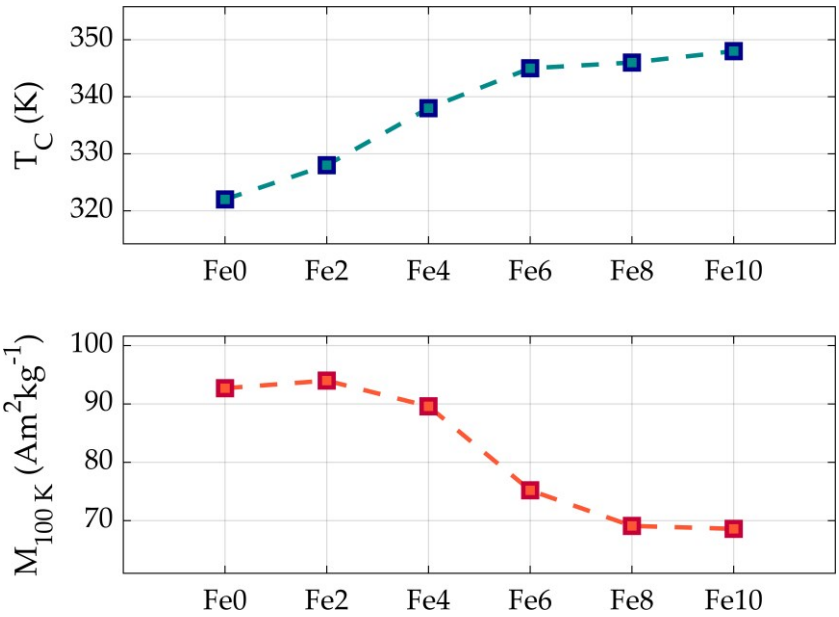

***Figure 6-11**: T_C values (top blue) and magnetization at T=100 K (bottom red) of the set $Ni_{48}Mn_{36-x}Sn_{16}Fe_x$ on function of the amount of Fe in the alloy. T_C values are calculated using the temperature derivates of the magnetic susceptibility and $M_{100\,K}$ are obtained by the magnetization curves.*

6.1.1.4 Pb addition to NiMnSn compounds

This section investigates the magnetic properties of the $(Ni_{50}Mn_{25}Sn_{15})_{100-x}Pb_x$ series. Unlike previous sets, this study seeks to modify the properties of the samples without altering the compositional ratios of the primary Heusler alloy. The choice of lead (Pb) is based on its atomic radius (180 pm), which is significantly larger than those of the other elements in the alloy (135 pm for Ni, 140 pm for Mn, and 145 pm for Sn). The inclusion of an atom with a larger atomic radius is expected to induce negative chemical pressure (expansion of the crystalline cell) and mimic the effects of external hydrostatic pressure, but with an inverse sign. As widely discussed in the literature [159], [160], [161], pressure variations in Heusler alloys can alter their magnetic properties, introducing an additional variable for tuning characteristics that are useful for thermomagnetic and magnetocaloric applications.

Previous attempts to melt this alloy type revealed challenges in melting Pb and achieving its miscibility within the alloy. To overcome this issue, a pre-melting step was introduced where Pb was alloyed solely with Ni followed by melting it with the remaining alloying elements. The samples were melted under an arc current of less

than 50 A to minimize excessive evaporation of Mn and Pb. Each sample underwent three successive melting steps, during which they were flipped and weighed between each step to promote alloy homogenization and monitor mass loss. Following synthesis, the samples were heat-treated at 1073 K for 72 hours.

Figure 6-12 presents the TMA measurements conducted during heating under an applied magnetic field of 1 mT. For the Curie transitions, the sample set demonstrates a clear trend: increasing the nominal Pb content in the alloy correlates with a reduction in the para-to-ferromagnetic transition temperature. The slopes of the Curie transitions indicate strong compositional homogeneity from a magnetic perspective, with no evidence of significant secondary magnetic phases. As before, the measurements are presented without normalization to better evaluate the sharpness of the transitions. It is important to emphasize, however, that the data shown in the figure are purely qualitative and should not be interpreted as having quantitative significance. Their primary purpose is to accurately identify the critical transition temperatures.

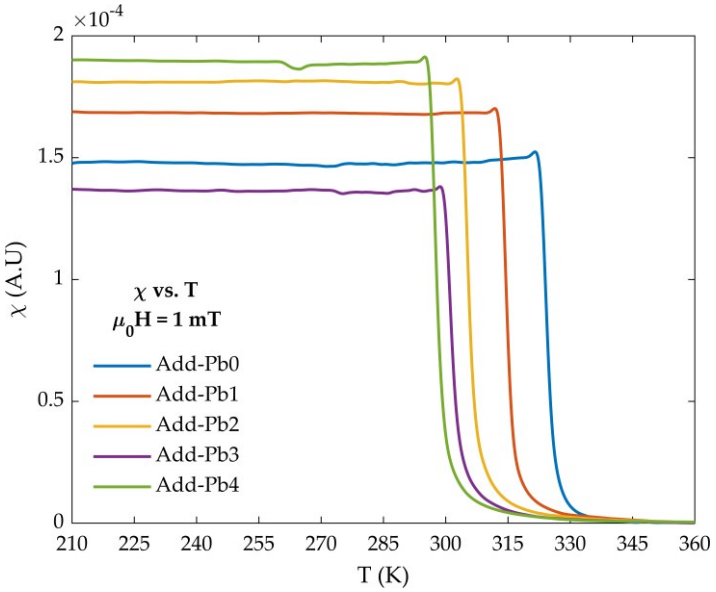

***Figure 6-12**: ac magnetic susceptibility in low applied magnetic field of 1 mT as a function of temperature for the samples: $Ni_{50}Mn_{35}Sn_{15}$ (blue), $(Ni_{50}Mn_{35}Sn_{15})_{99}Pb_1$ (orange), $(Ni_{50}Mn_{35}Sn_{15})_{98}Pb_2$ (yellow), $(Ni_{50}Mn_{35}Sn_{15})_{97}Pb_3$ (purple), and $(Ni_{50}Mn_{35}Sn_{15})_{96}Pb_4$ (green).*

In Figure 6-13, the temperature-dependent magnetization curves are presented, measured using the SQUID magnetometer detailed in Section 5.4 with an applied

magnetic field of 1 T. The measurements were carried out over a temperature range spanning from 10 K to 350 K, with a controlled temperature ramp rate of 2 K/min. Both cooling and heating cycles were performed to capture the thermal hysteresis associated with the martensitic phase transition in the two investigated samples, Add-Pb0 and Add-Pb1. The data reveal a systematic decrease in magnetization as the Pb content in the alloy increases, with a notable reduction of approximately 20% between the Add-Pb0 and Add-Pb-4 samples. This trend highlights the influence of Pb concentration on the magnetic properties of the alloy, suggesting a correlation between Pb content and the observed magnetization behavior during the martensitic transition. From the magnetometer measurements, it is possible to calculate the characteristic temperatures of the martensitic transitions for the first two samples of the series, as reported in Table 6-5.

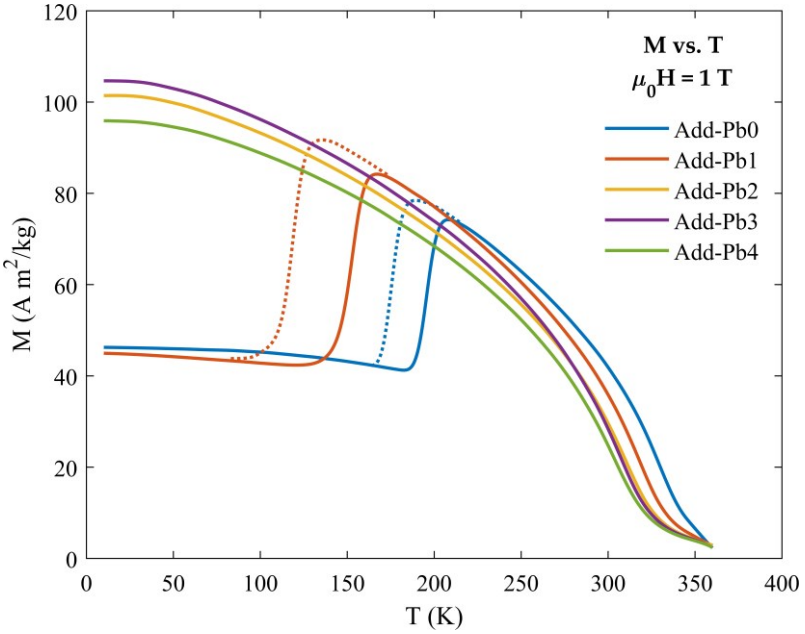

***Figure 6-13**: S.Q.U.I.D. magnetometer magnetization measures in 1T applied magnetic field as a function of temperature for the samples: $Ni_{50}Mn_{35}Sn_{15}$ (blue), $(Ni_{50}Mn_{35}Sn_{15})_{99}Pb_1$ (orange), $(Ni_{50}Mn_{35}Sn_{15})_{98}Pb_2$ (yellow), $(Ni_{50}Mn_{35}Sn_{15})_{97}Pb_3$ (purple), and $(Ni_{50}Mn_{35}Sn_{15})_{96}Pb_4$ (green). The blue and orange dashed lines represent the cooling curves of Add-Pb0 and Add-Pb1 samples respectively.*

Sample	M_S (K)	M_F (K)	A_S (K)	A_F (K)	ΔT_{Hyst} (K)
Add-Pb0	189	166	184	204	20

Add-Pb1	126	101	135	156	35

***Table 5**: Summary table of the critical temperatures characterizing the martensitic transitions martensitic start (M_S), martensitic finish (M_F), austenitic start (A_S), austenitic finish (A_F), and the thermal hysteresis (ΔT_{Hyst}).*

Although the Add-Pb0 sample and the Ni/MnX0 and Ni/MnX2 samples have similar compositions, a comparison of the magnetisation curves as a function of temperature (Figures 6-5 and 6-13) reveals significantly different behaviour. Notably, the Add-Pb0 sample exhibits a structural transition above 150 K, which was absent in the series described in Section 6.1.1.2. These differences confirm the high sensitivity of magnetostructural transition temperatures to the Sn content in this type of Heusler alloy, as even small variations in Sn can lead to significant changes [97], [100], [162], [163].

The sample compositions were analyzed using EDX Spectroscopy within the SEM. For each alloy, compositional measurements were taken from multiple regions of the sample to calculate an average and derive the most precise overall composition possible.

Additionally, compositional maps are presented, with each element in the alloy within a specific region represented by different colors. This approach facilitates the identification and visualization of secondary phases.

As an example, Figure 6-14 illustrates the compositional maps of the Add-Pb3 sample. The measurements for this sample effectively highlight an issue observed throughout the entire series: the apparent immiscibility of Pb within the alloy. Surface measurements indicate uniform compositions with no detectable lead; however, within the craters, spherical Pb precipitates become evident, as clearly shown in the figure. Images 6-14 (b-d) reveal dark regions, which in Figure 6-14 are identified as the only areas where Pb is present.

Measurements across the full sample set reveal that as the nominal Pb content in the alloy increases, the presence of Pb precipitates also increases. Moreover, the amount of Pb detected in the primary phase is consistently below the experimental error margin of 1%, making it impossible to definitively quantify the Pb content in the primary alloy, even in significantly lower amounts than the nominal compositions.

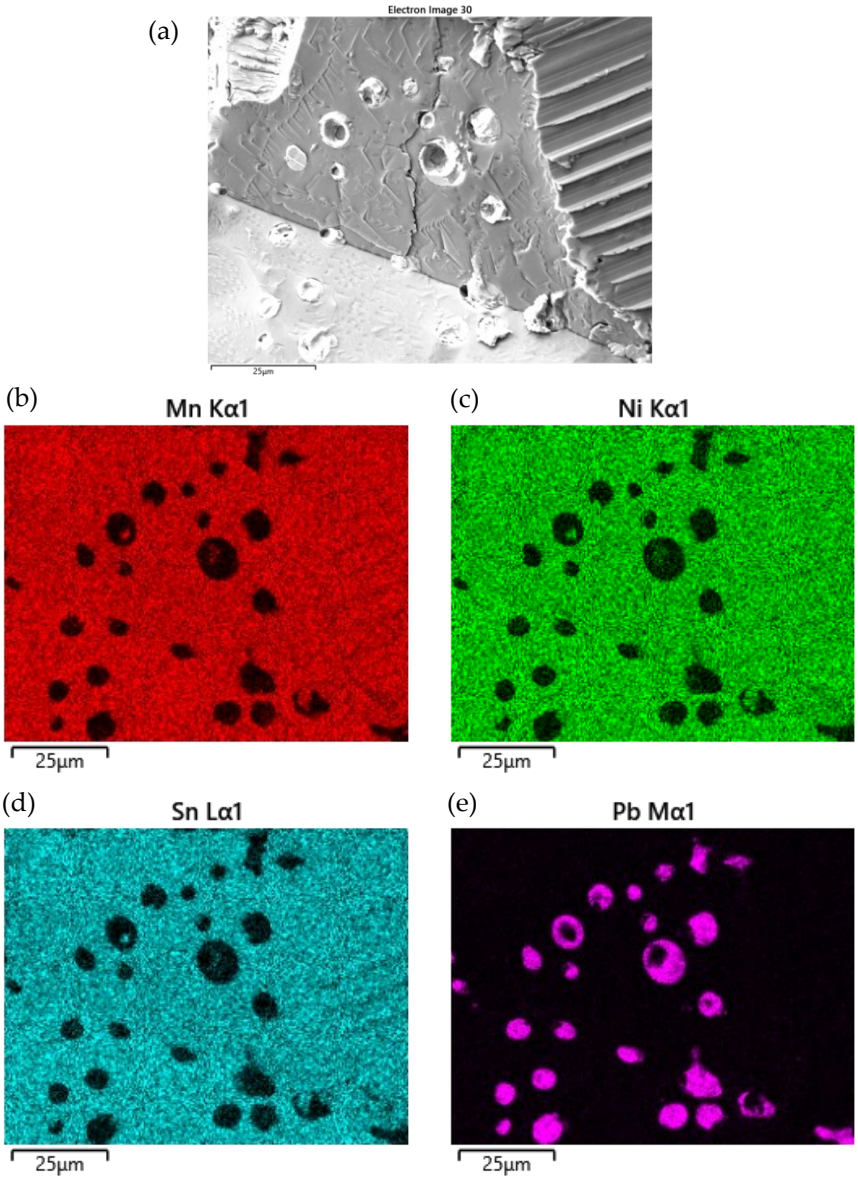

***Figure 6-14**: (a) SEM image of the sample Add-Pb3, (b,c,d,e) EDX compositional maps showing with different colour the distribution of each element Mn, Ni, Sn and Pb respectively.*

Table 6-6 reports the compositions measured by EDX. Notably, as the nominal Pb content in the alloy increases, a decrease in Ni content is observed. This phenomenon is likely attributable to the pre-melting of Ni-Pb conducted prior to the synthesis of

the primary alloy. Similar to Mn, Pb exhibits a significant evaporation rate, and in this context, a possible explanation, to be verified with further experiments, is that the prealloyng of Pb with Ni results in an increased evaporation of both elements and to the observed reduction of Ni content in the final alloy.

The results indicate that the Sn content remains relatively constant, while the Mn content increases at the expense of Ni.

Sample	Nominal composition	Ni (%)	Mn (%)	Sn (%)	Pb (%)
Add-Pb0	$Ni_{50}Mn_{35}Sn_{15}$	49.5	35.3	15.2	-
Add-Pb1	$Ni_{49.5}Mn_{34.65}Sn_{14.85}Pb_{1}$	47.8	38.0	14.1	0.1
Add-Pb2	$Ni_{49}Mn_{34.3}Sn_{14.7}Pb_{2}$	46.2	39.6	14.1	0.1
Add-Pb3	$Ni_{48.5}Mn_{33.95}Sn_{14.55}Pb_{3}$	46.0	40.0	13.8	0.2
Add-Pb4	$Ni_{48}Mn_{33.6}Sn_{14.4}Pb_{4}$	45.0	40.9	13.8	0.3

***Table 6**: In the first two column are reported the samples' name and the nominal composition of the synthetized $(Ni_{50}Mn_{35}Sn_{15})_{100-x}Pb_x$. In the other columns are reported the actual compositions measured with EDX.*

The following table (Tab. 6-7) presents the measured compositions, compared with the key magnetic properties obtained from the earlier characterizations. In this case, the sample compositions are reported without Pb, as its quantity is significantly below the experimental error margin. Additionally, its detection is likely attributable to the presence of subsurface Pb precipitates in the detector's analysis area.

Sample	Measured composition	T_C (K)	M_{100K} ($Am^2 kg^{-1}$)	$\partial M/\partial T_{Tc}$ ($Am^2 kg^{-1}K^{-1}$)	ΔM_{4K} ($Am^2 kg^{-1}$)
Add-Pb0	$Ni_{49.5}Mn_{35.3}Sn_{15.2}$	325	45.2 *	0.92	3.6
Add-Pb1	$Ni_{47.8}Mn_{38.0}Sn_{14.1}Pb_{0.1}$	314	42.8 *	0.91	3.6
Add-Pb2	$Ni_{46.2}Mn_{39.6}Sn_{14.1}Pb_{0.1}$	305	93.2	0.85	3.4
Add-Pb3	$Ni_{46.0}Mn_{40.0}Sn_{13.8}Pb_{0.2}$	301	96.2	0.88	3.5
Add-Pb4	$Ni_{45.0}Mn_{40.9}Sn_{13.8}Pb_{0.3}$	298	88.8	0.81	2.9

***Table 7**: A summary table of the results obtained from the characterization of the $(Ni_{50}Mn_{35}Sn_{15})_{100-x}Pb_x$ set is presented. In the first column (sample), the names of the samples used are listed, as summarized in Table 6-1. The second column (composition) reports the compositions of the samples measured via EDX analysis. The third column (T_C) shows the Curie temperature measurements obtained from low-field magnetic susceptibility measurements. In the fourth column (M_{100K}), the magnetization value at T = 100K is calculated from magnetization measurements, the values followed by asterisk refer to the magnetization values of the martensitic phase. The fifth column ($\partial M/\partial T_C$) reports the maximum absolute value of the derivative of the magnetization curve with respect to temperature. Finally, the sixth column (ΔM_{4K}) provides the difference in magnetization calculated over a temperature range of 4K around the Curie temperature of the sample.*

Figure 6-15 shows the outcomes from the previously discussed magnetic characterization. The blue markers at the top of the image indicate the Curie temperatures, which were determined by locating the peaks in the temperature derivatives of the TMA curves (Figure 6-12). The red markers represent the magnetization values of the samples at T=100 K, derived from the data presented in Figure 6-13.

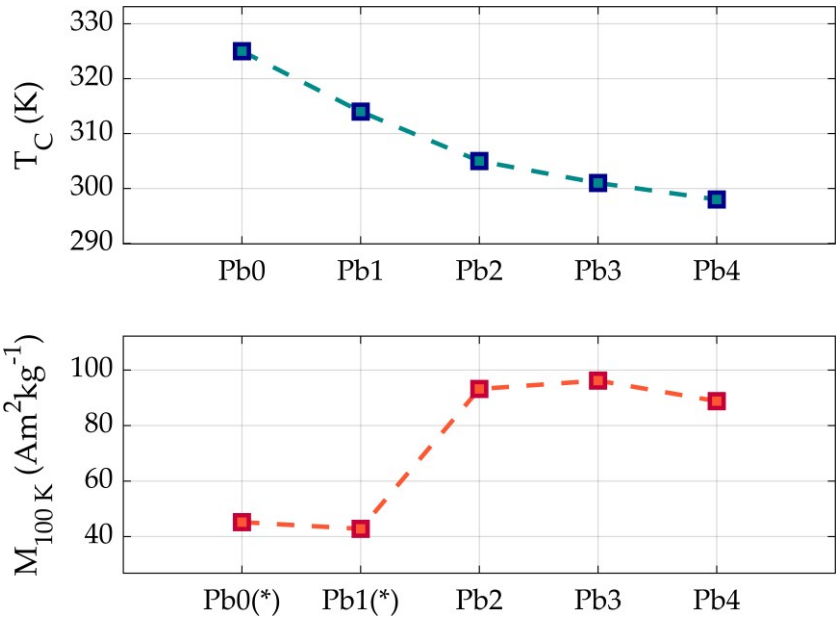

***Figure 6-15**: T_C values (top blue) and magnetization at T = 100 K (bottom red) of the set $(Ni_{50}Mn_{35}Sn_{15})_{100-x}Pb_x$ on function of the nominal amount of Pb in the alloy. T_C values are calculated using the temperature derivates of the magnetic susceptibility and M_{100K} are*

obtained by the magnetization curves. The Pb0 and Pb1 values refer to the magnetization values of the martensitic phase.

The diffraction patterns (Fig. 6-16), obtained through powder diffraction, were analysed using the Jana 2006 software: through Le Bail refinement, the diffraction peaks were indexed, and the lattice parameters were determined, assuming a cubic structure.

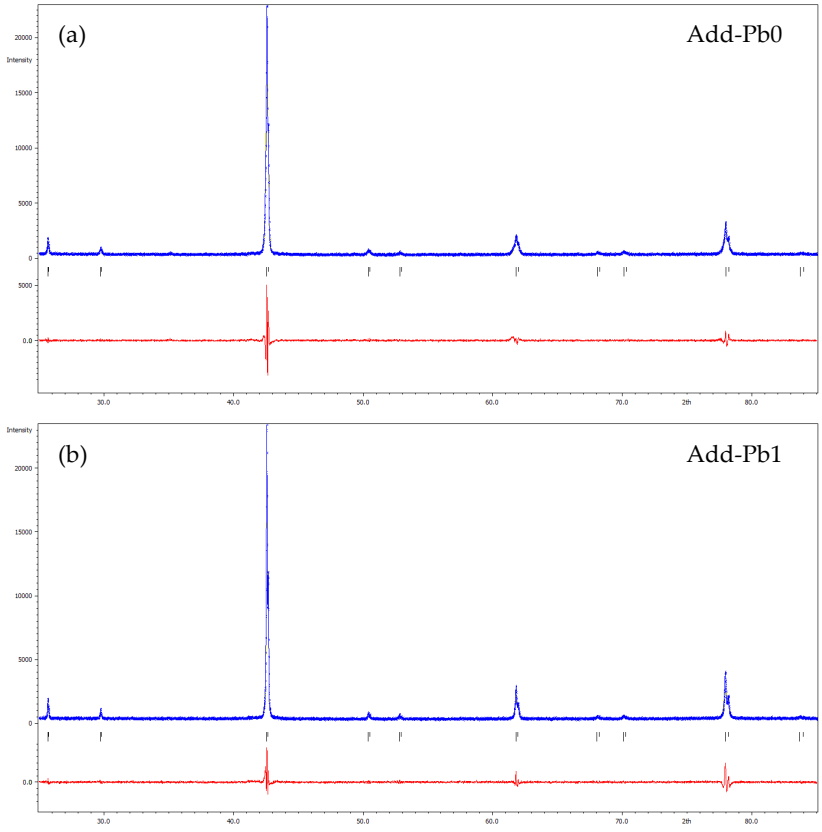

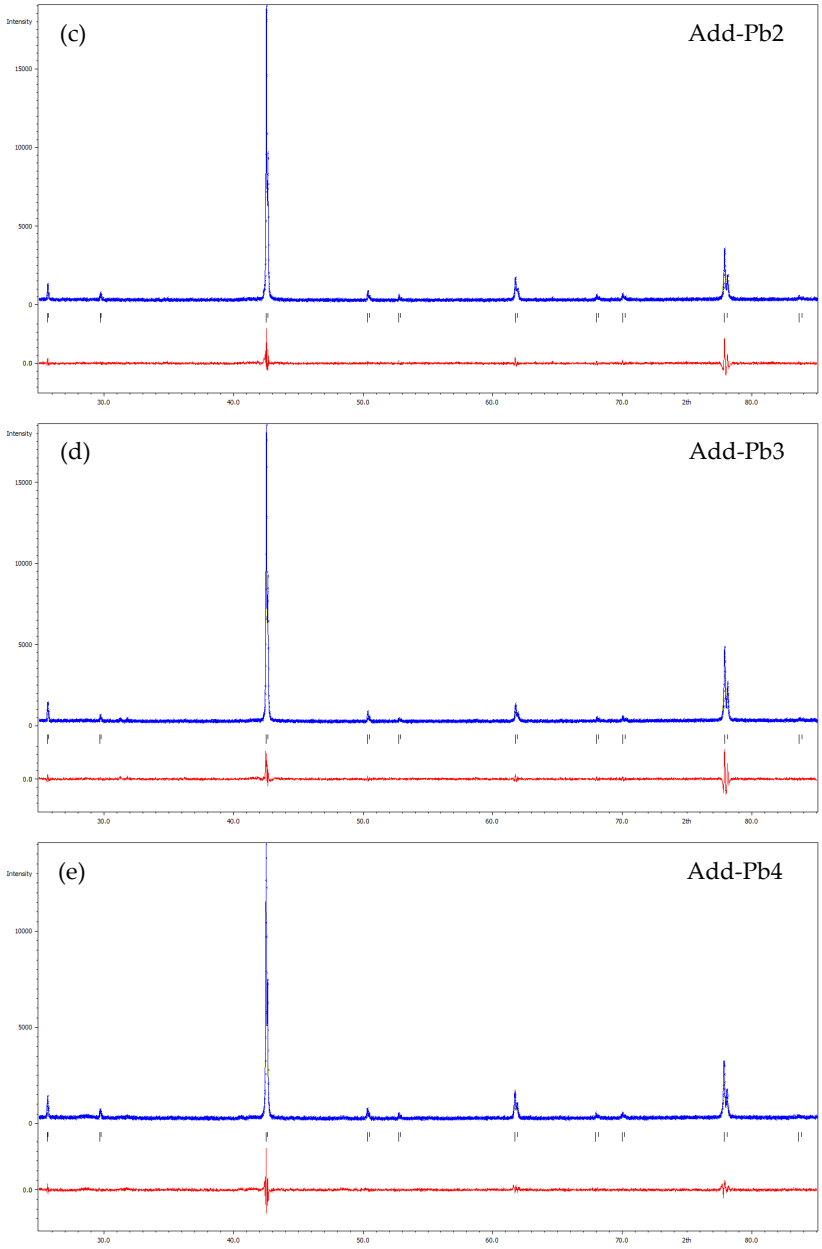

***Figure 6-16**: Diffraction patterns of the set $(Ni_{50}Mn_{35}Sn_{15})_{100-x}Pb_x$ with x=0 (a), x=1 (b), x=2(c), x=3(d) and x=4 (e). The blue curve represents the observed data set, the ticks correspond to the reflections, and the red curve represents the difference between the observed and calculated data. The goodness of fit (GOF) for each diffraction patterns are 2.72, 2.65, 2.53, 2.69 and 2.31 respectively.*

Table (6-8) presents the cell parameters obtained through the refinement process.

sample	a(Å)	b(Å)	c(Å)	α(deg)	β(deg)	γ(deg)
Add-Pb0	5.9952(2)	5.9952(2)	5.9952(2)	90	90	90
Add-Pb1	5.9956(3)	5.9956(3)	5.9956(3)	90	90	90
Add-Pb2	5.9992(2)	5.9992(2)	5.9992(2)	90	90	90
Add-Pb3	6.0008(3)	6.0008(3)	6.0008(3)	90	90	90
Add-Pb4	6.0032(2)	6.0032(2)	6.0032(2)	90	90	90

Table 8: Cell parameters obtained after Le Bail refinement.

The diffraction data and their refinement confirm that all solids crystallize in a cubic structure with $L2_1$ structure and the absence of secondary phases. Starting from the Pb-free sample, Fig. 6-16 (a), a cubic cell dimension of 5.9952 ± 0.0002 Å was obtained. Analysis of subsequent samples shows an expansion of the cell dimension with increasing lead concentration, this behaviour is synthesized in Figure 6-17.

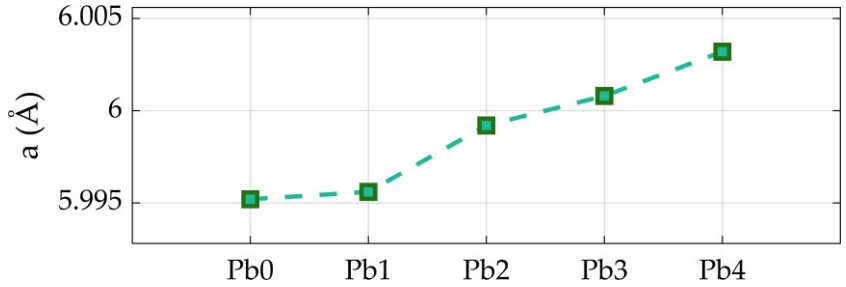

***Figure 6-17**: cubic cell dimension of the set $(Ni_{50}Mn_{35}Sn_{15})_{100-x}Pb_x$ on function of the nominal amount of Pb in the alloy.*

XRD analyses reveal a correlation between the increase in the crystal cell size and the increase in the nominal amount of Pb in the composition.

EDX measurements are consistent with the presence of Pb in the alloy (although a quantitative assessment is not possible) and/or a concurrent, although unintended, decrease of the Ni/Mn ratio. The combined effect of Pb incorporation (which has the larger covalent radius than the other elements in the alloy) and the increase of Mn content in spite of Ni, can result in a monotonic increase of the lattice volume with nominal Pb content increasing.

The tunability of T_C and the observed change in magnetization may therefore be attributed to the variation in the stoichiometric ratio of the alloy elements and the presence of Pb within the crystal lattice.

As outlined in section 6.1, the motivation behind synthesizing this specific set of samples lies in the development of strategies to finely tune the magnetic properties of Heusler alloys. Typically, for applications in waste heat recovery, the primary criterion for selecting magnetic alloys is their magnetization in the ferromagnetic phase, while critical temperatures, provided they are close to ambient temperature, are often considered of lesser importance. However, as will be explored in greater detail in the subsequent section on thermomagnetic devices, a material's efficiency is highly sensitive to its operational temperature range, which dictates the suitability for specific applications. Consequently, this section focuses on assessing and exploring the feasibility of adjusting the critical temperature of a magnetic alloy by implementing slight compositional variations. The ability to modify an alloy to span a wide temperature range by tuning its Curie temperature allows for the precise optimization of its composition tailored to particular applications.

Figure 6-18 illustrates a comprehensive plot of the Curie temperatures for all alloys investigated in this section. The data reveals how a broad temperature range can be densely populated through compositional tuning, underscoring the potential of Heusler alloys, specifically NiMnSn, as promising candidates for TM and MC applications.

In addition, NiMnSn provides a substantial economic advantage due to its low production cost. The cost of individual alloying elements plays a pivotal role in determining the economic feasibility of magnetic materials, and thus becomes a critical factor in the selection process for applications requiring efficient and cost-effective magnetic alloys.

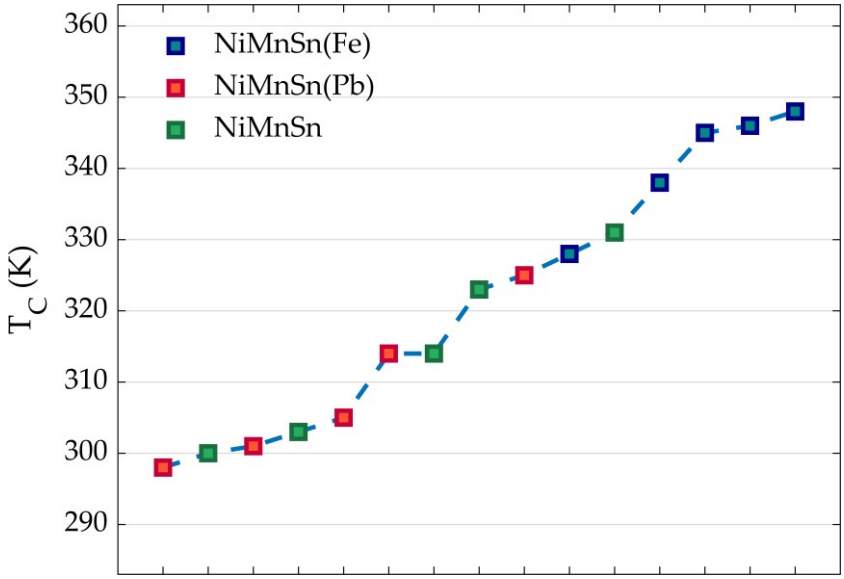

***Figure 6-18**: A summary graph depicting the TC values for all the NiMnSn-based alloy sets is provided. The Curie temperatures for the NiMnSn(Fe) set are indicated in blue, for the NiMnSn(Pb) set in red, and for the NiMnSn set with a variable Ni/Mn ratio in green. These sets are described in detail in sections 6.1.1.3, 6.1.1.4, and 6.1.1.2, respectively.*

6.1.2 Functional testing of TM properties of Heusler compounds

In this section, a thorough thermomagnetic characterization of the selected Heusler alloys discussed in Section 6.1.1.1 is presented, combining detailed analysis of thermomagnetic cycles derived from magnetization measurements with in-operando evaluation of their thermomagnetic performance in a *in situ*-built TM motor prototype (technically described in Section 5.5). The prototype is designed as a flexible and adaptable test platform, allowing for the precise characterization of small masses of thermomagnetic materials (less than 0.3 g) under various operational conditions.

As highlighted in the discussion of the thermomagnetic cycle (Section 3.2.1), an ideal TM material should exhibit significant changes in magnetization over a narrow temperature range, centered around a magnetic transition. One of the primary criteria for assessing the suitability of a magnetic material for TM applications is its magnetization value. Furthermore, as outlined in the previous sections, the ability

to fine-tune magnetic transitions enables the optimization of magnetization change based on specific application requirements. As will be elaborated upon later, the efficiency of the thermomagnetic cycle is highly sensitive to the temperature range in which it is measured, leading to considerable variability in performance depending on the operational context. Nonetheless, it should be noted that magnetic properties are not the only critical factors in the evaluation of TM materials.

The thermal properties of the material are crucial in determining the performance of thermomagnetic devices: allowing for a fast heat exchange between the material and the heat reservoirs has a fundamental influence both to the cycle frequency and the energy conversion rate per unit time. These properties can be estimated by evaluating the material's thermal diffusivity, which is a function of density, thermal conductivity, and specific heat. However, additional factors—such as the convective heat transfer coefficient of the fluid used and the geometry of the thermomagnetic material—also play a significant role in determining the overall heat exchange rate.

While it is challenging to comprehensively evaluate the thermomagnetic properties due to the multitude of relevant physical characteristics, it is essential to identify a simpler yet effective figure of merit for assessing thermomagnetic materials. As introduced earlier, this thesis adopts the FoM defined as the useful work generated per cycle per unit mass (eq. 3.15). The FoM is calculated as the area enclosed between the two magnetization curves M(H) corresponding to the highest and lowest temperatures reached by the material during the thermomagnetic cycle, denoted as T_{hot}^{TM} and T_{cold}^{TM}, respectively.

This approach simplifies the analysis compared to traditional thermal efficiency models (eq. 3.13), as it bypasses the need to directly calculate the absorbed heat, instead focusing on the material's energy density. The temperature extremes T_{hot}^{TM} and T_{cold}^{TM} are chosen to reflect the realistic conditions of the thermomagnetic cycle, accounting for both the material properties and the device's operational environment.

As previously discussed, (Section 3.2.2), the cycle frequency is inversely proportional to the temperature difference T_{hot}^{TM} - T_{cold}^{TM}. Materials that complete faster cycles have less time to exchange heat with their surroundings, which causes their internal temperatures to deviate from the thermal source temperatures. Therefore, the selection of T_{hot}^{TM} and T_{cold}^{TM} values reflect not only the inherent properties of the thermomagnetic material but also the characteristics of the system in which the material operates, and the external conditions under which the cycle occurs.

To initially assess the thermomagnetic properties of the TM-Sn, TM-In, and TM-CuGa samples, their isothermal magnetization curves were analyzed, as shown in Figure 6-3. These curves define the M(T,H) surface, which is essential for calculating the FoM (Figure 6-19).

Using the surfaces, thermomagnetic cycles for each sample were simulated by adjusting parameters such as the temperature of the hot source or the difference between T_{Hot}^{TM} and T_{Cold}^{TM} to compute the corresponding FoM.

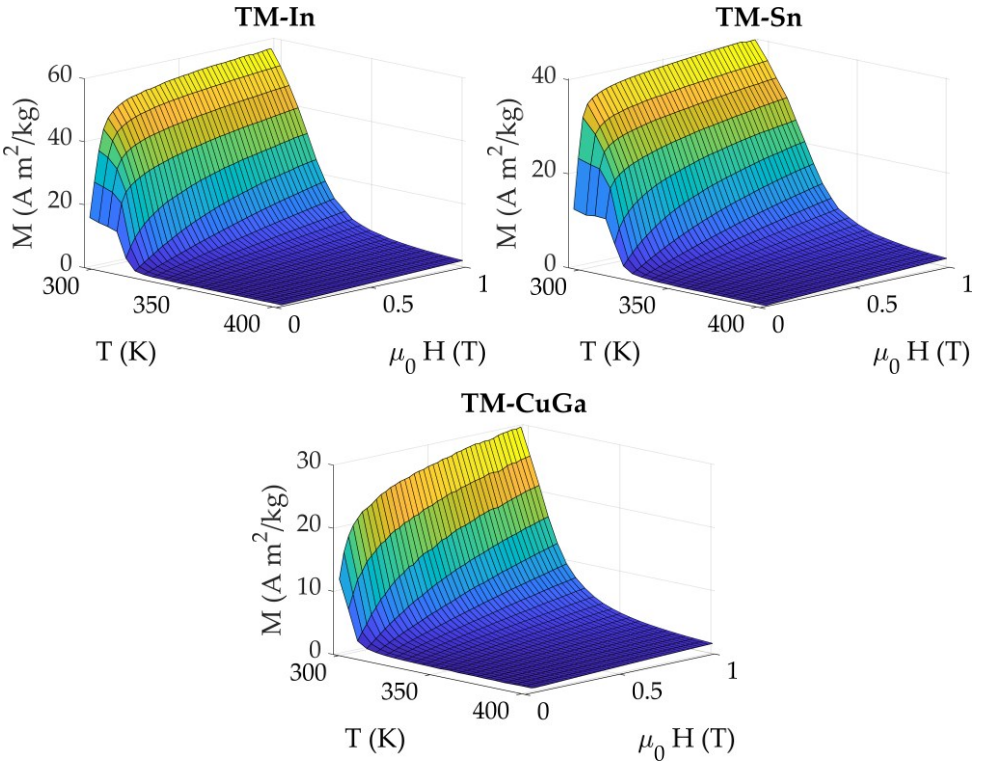

***Figure 6-19**: M(T,H) surface of the TM-Sn sample, derived from M(H) isothermal conducted at various temperatures within the thermomagnetic range of interest. The yellow and the dark blue region correspond to the highest and the lowest values of magnetization respectively.*

Figure 6-20 provides a comparative analysis of the useful magnetic work produced by the three materials under study alongside the benchmark gadolinium. The evaluation considers a maximum applied magnetic field of 0.6 T, with the cold source set at 297 K and the warm reservoir varying between 300 K and 400 K. In

Appendix 8.4 other analysis of the useful magnetic work varying different parameters are presented

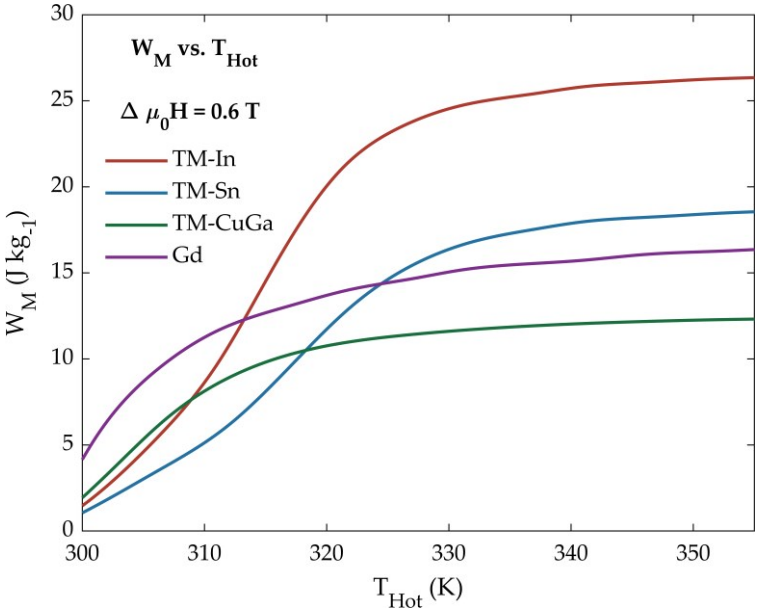

***Figure 6-20**: FoM generated by an ideal TM cycle utilizing NiMnIn, NiMnSn, NiMnCuGa, and Gd materials as a function of the warm cycle temperature T_{hot}. The cold temperature is held constant at 290 K, along with a magnetic field of 0.6 T. The FoM is computed using equation 3.15, based on the surfaces M(T,H) data presented in Figure 6-18.*

An important assumption is made in this calculation: the integration limits of the FoM in Eq. 3.15 are set to match the temperatures of the thermal reservoirs. While this assumption results in calculations that are not quantitatively aligned with realistic application scenarios, it is nevertheless effective for conducting a qualitative comparison between thermomagnetic materials. It enables a clear understanding of how the FoM varies as a function of the thermal reservoir temperatures, within the approximation of either very long operational cycles or very high thermal diffusivity.

Near room temperature, Gd delivers the highest potential output due to its large saturation magnetization (M_{S4K} = 254 Am^2kg^{-1} [21]), which is twice that of the leading Heusler alloy, NiMnIn (M_{S4K} = 135.5 Am^2kg^{-1} [143]). Beyond 310 K, Gd's magnetic work output plateaus as the paramagnetic phase contributes minimally above 292 K. At higher temperatures, above 313 K, a thermomagnetic cycle using NiMnIn demonstrates superior work generation. NiMnSn (M_{S4K}= 96.2 Am^2kg^{-1} [149]) shows

a similar temperature dependence in magnetic work output to NiMnIn, but with a roughly 25% reduction in maximum work, attributed to its lower saturation magnetization. Therefore, NiMnSn overcomes the Gd performance at a higher temperature, above 325 K. NiMnCuGa further reduces the maximum magnetic work but compensates with a lower Curie temperature, making it more effective than the other Heusler alloys at lower temperature ranges. These findings prove the critical role, discussed in Section 3.2.2, of saturation magnetization and Curie temperature in identifying the most suitable thermomagnetic material for a given operational temperature range, particularly for materials exhibiting a second-order Curie transition.

Nevertheless, considering the thermal reservoirs' temperatures as the integration boundaries for the cycle may be unrealistic given the real-world constraints of operational frequencies and heat exchange dynamics. It is therefore fundamental to assess the functional properties of the thermomagnetic materials, and this can be conveniently achieved using the TM device.

A mass of 0.23±0.01 g from each TM-Heusler alloy (TM-In, TM-Sn and TM-CuGa) was formed into a ring-shaped rotor and integrated into the motor. The rotor's mechanical power output, torque, and angular velocity, driven by TM cycles, were recorded by adjusting the temperature of the heat source (T_{hot}) and modifying the external resistive load on the generator.

As previously mentioned in sections 4.2.2, the rotors were fabricated from an epoxy-based composite containing magnetic powder. The powders were obtained from the bulk samples of the TM set described in section 6.1.1.1 through manual grinding and sieving to achieve a particle size of less than 120 μm. The powders were then heat-treated at 773 K for 4 hours. The epoxy, a bisphenol-A epoxy resin-based vinyl ester in styrene, was selected for its low water content and absence of polar compounds. No metallic accelerators were added to prevent unwanted reactions with the magnetic components. The composites were cast into rings using water-soluble bioplastic molds, each with an insoluble plastic core that would provide the scaffold needed to connect the rotors to the generator shaft to the generator shaft. The rotors (Fig. 6-21 (a)), with internal diameters of 18 mm or 17 mm and thicknesses of 1 mm or 1.5 mm, contained approximately 0.23 g or 0.34 g of active magnetic material, respectively.

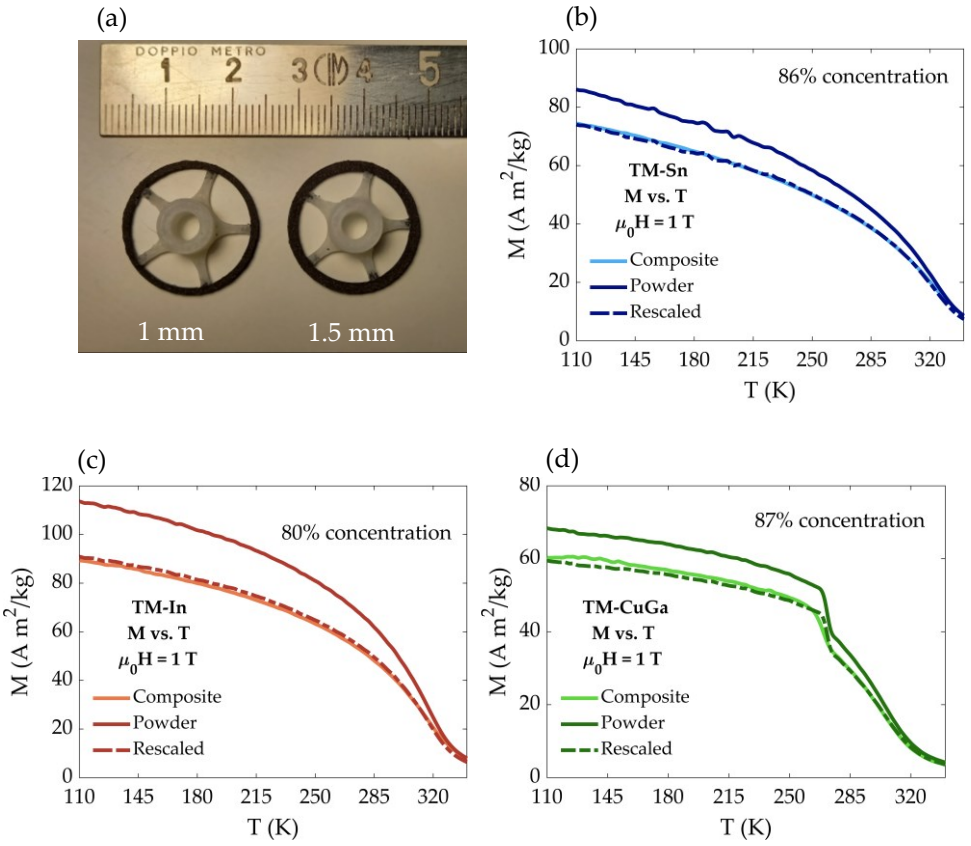

***Figure 6-21**: (a) Example of MM rotors made with TM-In alloy with a radial thickness of 1 mm and 1.5 mm. (b,c,d) Isofield magnetization curves for unit mass of the powder (dark coloured), the composite (light coloured) and the rescaled powder (dashed dark coulored) of TM-Sn (blue), TM-In (red) and TM-CuGa (green) samples.*

Figure 6-21(b-d) presents the measurements of the isofield magnetization curves with an applied magnetic field of 1T conducted using the extraction magnetometer, employed to determine the concentration of magnetic powders within the composite. These measurements are conducted in a temperature range between 100 K and 340 K of both the reference powders and the composite. The magnetization values in the figure are reported per unit mass, and by rescaling the reference magnetization curve to match that of the composite, it is possible to determine the actual concentration of magnetic powders within the composite and calculate the mass of the active material. The mass concentration of active materials ranged between 80% and 87%, as shown in Fig. 6-21

Rotors are inserted into the TM tester described in Section 5.3 and presented in Figure 6-22. The device comprises a controlled heat source and an assembly of permanent magnets creating a magnetic field gradient with a maximum intensity of 0.6 T. The rotor is partially immersed in warm water at temperature T_{hot}, simulating the heat source, while being exposed to the magnetic field gradient.

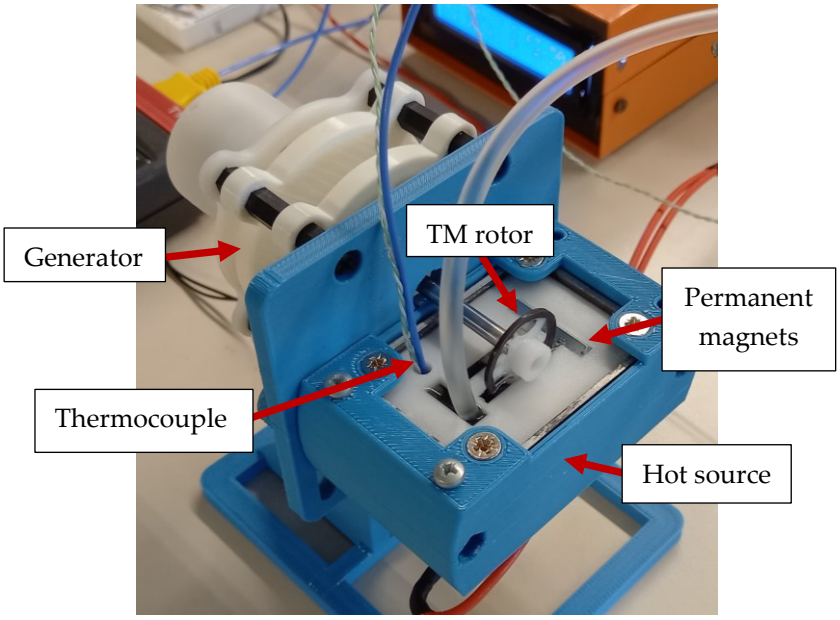

***Figure 6-22**: Photograph of TM tester utilized for testing materials in which all relevant elements are labelled.*

The rotor shaft is connected to a custom-designed two-phase electric motor, Allowing for the measurement of the TM motor's angular speed and torque. A calibration procedure, which involves applying a known torque to the shaft, determines the constants of the electric generator and measures the friction torque of the TM motor (Appendix 8.1). The overall torque generated by the TM motor is calculated by correcting the collected torque data for the measured friction values. A controlled electronic load assesses the TM motor's performance by varying the external load. Integrated software allows for continuous monitoring of the TM motor's mechanical output and the temperatures of the cold and hot reservoirs.

Figure 6-23 illustrates the relationship between mechanical power output and angular speed for the three materials, measured at various values of T_{hot}, while the temperature of the cold reservoir is kept constant at 297 K. Overall, there is a clear trend indicating that as the temperature of the warm heat source increases, the

power output tends to rise. This increase can be attributed to the enlargement of the cycle area, which enhances energy conversion efficiency. However, it is important to note that this trend is influenced by the rotation speed of the rotor.

At higher external loads, the rotational speed is relatively low, which in turn limits the power output achievable by the system. As the external load decreases, the rotational speed of the rotor increases, resulting in a corresponding increase in power output until it reaches a peak value. Beyond this optimal point, further increases in rotational speed can lead to a stabilization or even a reduction in power output. This phenomenon is particularly evident in measurements taken with T_{hot} values that exceed the Curie temperature of the materials being tested.

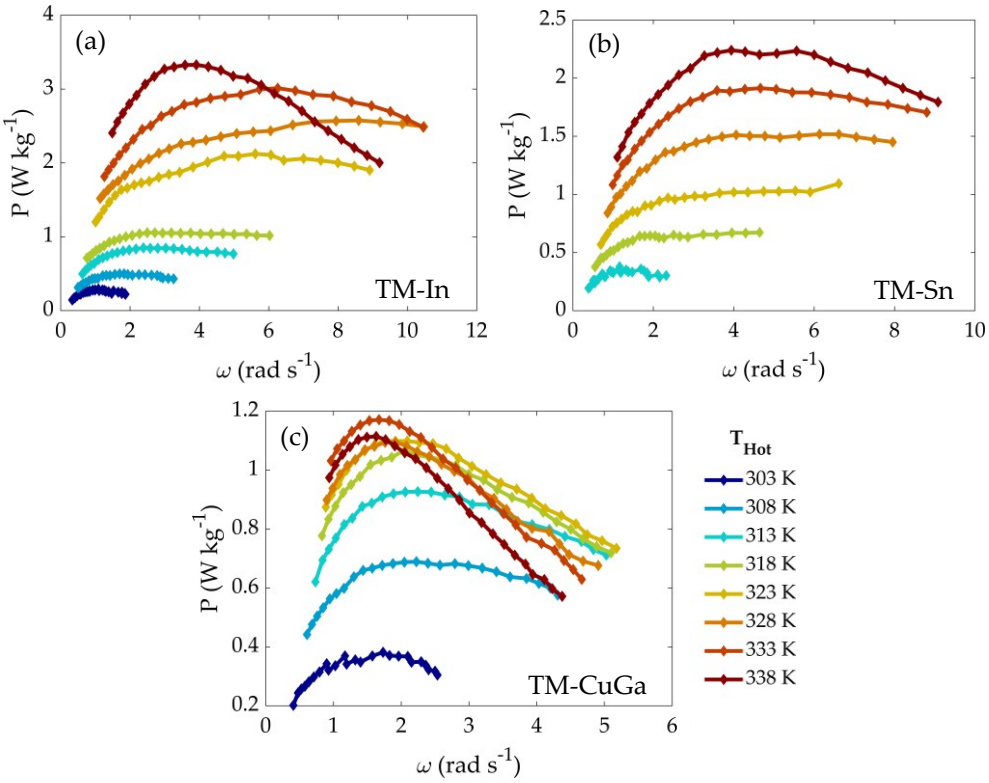

***Figure 6-23**: Mechanical power output of the TM tester as a function of angular speed of the shaft, achieved by adjusting the temperature of the warm source T_{hot} and the external resistive load, using rings made of (a) TM-In, (b) TM-Sn, and (c) TM-CuGa. Each data point represents the average of measurements taken during both increasing and decreasing load sweeps. The solid lines are provided as visual aids.*

The observed decrease in power output at high speeds can be attributed to a reduction in the heat exchanged during the thermomagnetic cycle. As a result, the cycle area diminishes, which directly impacts the output power. When the average temperature of the cycle surpasses the Curie temperature of the active thermomagnetic material, the reduction in the derivative of magnetization with respect to temperature ∂M/∂T leads to a decrease in the net torque experienced by the rotor. Consequently, this reduction in torque results in diminished power output. This effect is particularly pronounced for TM-CuGa sample, as depicted in Figure 6-23 (c), since it possesses the lowest Curie temperature among the materials analysed in this study.

Figure 6-24 illustrates a comparison of the maximum power output as a function of T_{hot} for the three materials. TM-CuGa achieves the highest output at lower temperatures. As the temperature of the warm reservoir increases, the output of TM-CuGa stabilizes, while the outputs of TM-In and TM-Sn continue to rise.

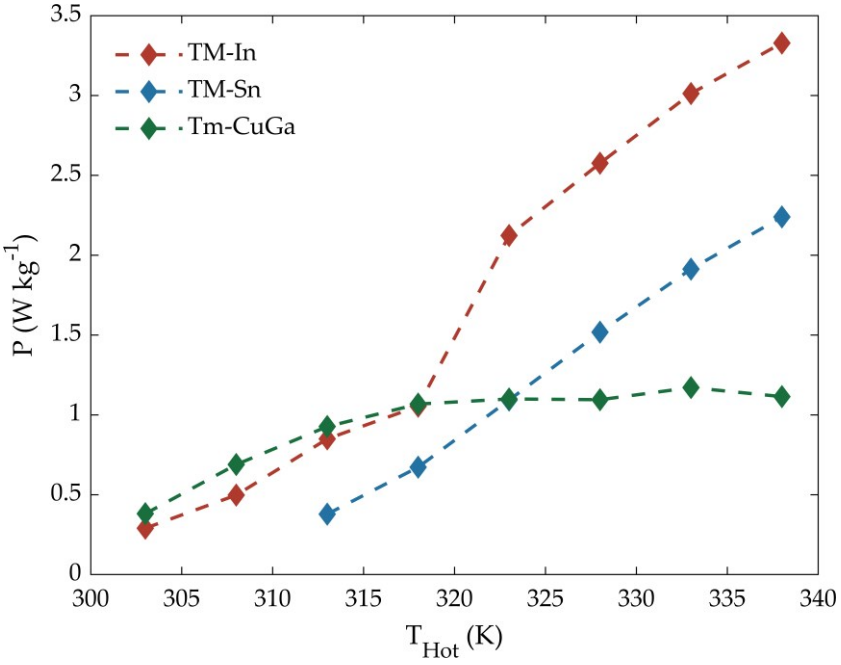

***Figure 6-24**: Maximum mechanical power output as a function of the warm reservoir temperature for rings made of TM-In (orange), TM-Sn (blue), and TM-CuGa (green). The solid lines are provided as visual aids.*

The TM-In rotor reaches a peak mechanical output of more than 3 W/kg. These values have been adjusted to account for mechanical losses due to friction, enabling a direct comparison of the mechanical work produced by the material.

The In-based rotor shows an approximately 26% higher output power values with respect to the Sn-based, in accordance with the cycle calculations based on the surface M(T,H). The temperature-dependent power output observed in the TM tester qualitatively follows the trends of the magnetic work from the thermomagnetic cycle shown in Figure 6-20, which is derived from M(T) and M(H) data, considering the temperatures of the cold and warm reservoirs as the cycle boundaries. However, a comparison between these two quantities, i.e. the experimental power output and the estimated magnetic work of the cycle, indicates that the experimental curves shift towards higher temperatures. The maximum power outputs for both TM-In and TM-Sn continue to rise within the 300-340 K range, while the calculated magnetic work from the cycle tends to saturate between 320 and 330 K. Likewise, the output measured for NiMnCuGa reaches saturation roughly 10 K above the calculated curve. This finding supports the hypothesis that the material does not fully attain the temperatures of the heat sources. This phenomenon, attributed to the slow heat exchange between the TM material and the heat sources, constrains the power output achievable by the TM motor. The explanation of the phenomenon is further supported by the results presented in Section 6.1.3, where thermomagnetic power curves as a function of the hot source temperature were obtained using thinner rotors to facilitate thermal exchange between the active material and the thermal sources. As will be shown later, these curves will exhibit a saturation of magnetic power.

Indeed, it is clear that the power output values measured directly are lower than the magnetic work calculated from thermomagnetic cycles (Figure 6-20) when adjusted for rotation frequency. For instance, for TM-In, the maximum power output of 3.0 W/kg at a frequency of 0.6 Hz corresponds to a mass-normalized work per cycle of 5.0 J/kg. This figure contrasts sharply with the 25 J/kg calculated for a thermomagnetic cycle between 297 K and 338 K. This comparison suggests that the limited heat transfer between the active material and the thermal sources prevents the material from reaching temperatures T_{cold} and T_{hot} during operation, thereby constraining the TM cycle and reducing the achievable output work. It is important to note that the reported estimates already incorporate corrections for friction energy losses, and magnetic losses can be considered negligible due to the very low coercivity of the materials studied.

To investigate how much the limited heat transfer between the active material and the thermal sources influence the performance of the TM generation, the outputs of three rotors with different geometries made from the same TM-In material were compared, as illustrated in figure 6-25. These include a ring rotor with a radial thickness of 1 mm, a ring rotor with a radial thickness of 1.5 mm, and a tandem rotor composed of two 1 mm thick rings mounted on the same shaft. The 7 mm separation between the two rings in the tandem rotor is sufficient to treat them as independent thermal entities, thus minimizing any effects related to water capillarity. The three rotors contain 0.23±0.01 g, 0.34±0.01 g, and 0.46±0.02 g of active TM material, respectively.

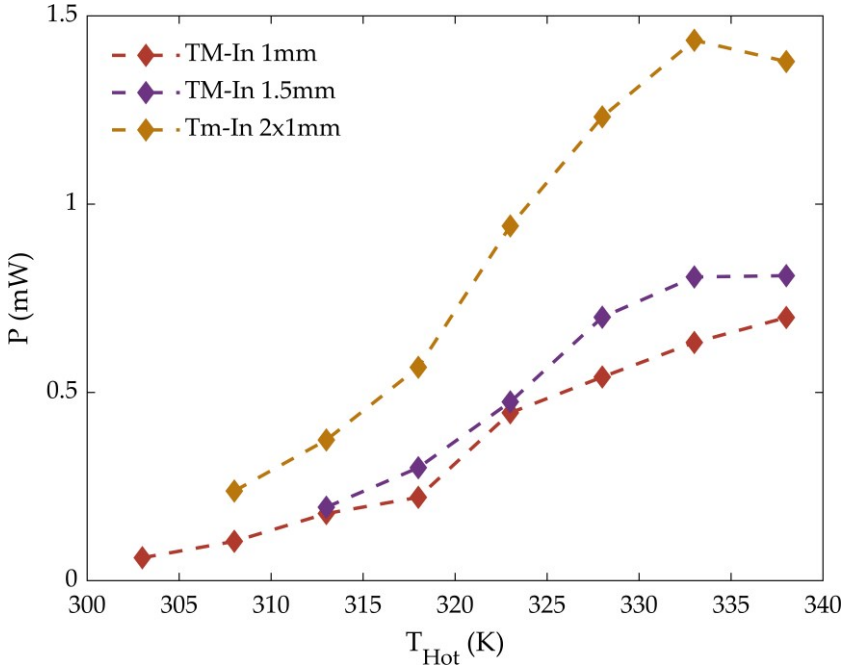

***Figure 6-25**: A comparison of the maximum mechanical power output in relation to the temperature of the warm reservoir is presented for three configurations: a single NiMnIn ring with a radial thickness of 1 mm (red), a single NiMnIn ring with a radial thickness of 1.5 mm (purple), and two NiMnIn rings, each with a radial thickness of 1 mm, attached to the same shaft (yellow). Solid lines are included to guide the interpretation of the data.*

From the measurements, it is observed that the power output of the tandem rotor is approximately double that of the single 1 mm rotor, while the power generated by the 1.5 mm thick rotor does not differ significantly from that obtained with the 1 mm thick rotor.

Conversely, the thickest rotor does not exhibit a proportional increase in power output relative to the mass of active material, with its normalized power limited to 2.4±0.1 W/kg. This limitation is attributed to the heat transfer dynamics between the rotor and its environment. Indeed, the mass-normalized power output of the three rotors (Fig.6-26) correlates well with their surface-to-volume ratios, which are 4 mm^{-1} for the 1 mm thick rotor and 3 mm^{-1} for the 1.5 mm thick rotor.

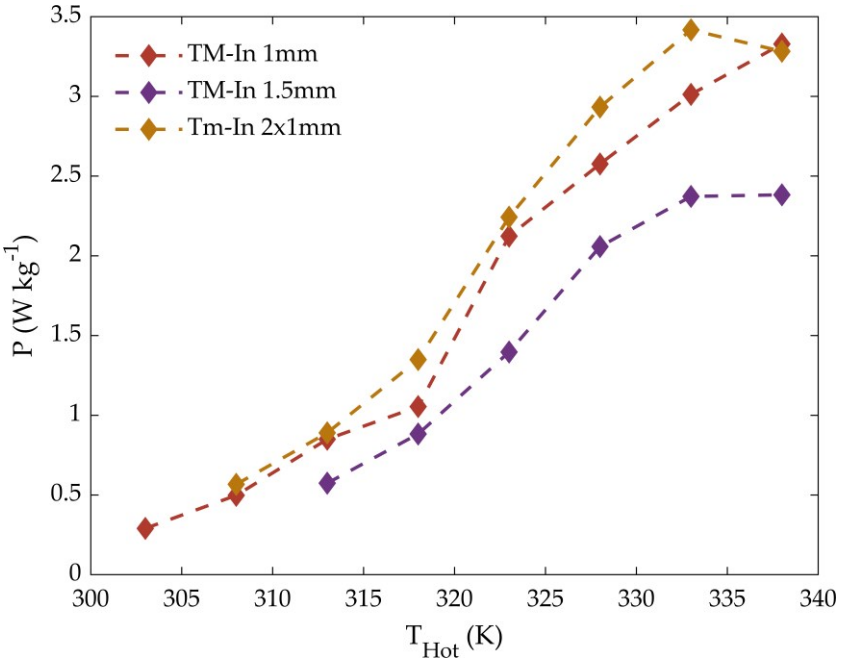

***Figure 6-26**: A comparison of the maximum mechanical power output per unit mass in relation to the temperature of the warm reservoir is presented for three configurations: a single NiMnIn ring with a radial thickness of 1 mm (red), a single NiMnIn ring with a radial thickness of 1.5 mm (purple), and two NiMnIn rings, each with a radial thickness of 1 mm, attached to the same shaft (yellow). Solid lines are included to guide the interpretation of the data.*

All reported TM generator tests indicate that the active magnetic material does not fully reach the thermal reservoirs temperatures during the cycle, primarily due to limited heat exchange. This limitation is largely governed by the thermal properties of the active material and the design of the TM generator, and it represents a significant challenge. Achieving both high operational frequencies and broader temperature spans during the cycle is essential for improving TM generation power output and efficiency. Consequently, the simulation of useful magnetic work (Fig.

6-20) has been revisited, accounting for a reduced temperature variation achieved by the material during the cycle.

To the thermal gradient on the MM rotors, an observation was made using a infrared thermal camera, from which an image is provided in Figure 6-27. The infrared image allows for the estimation of the ΔT on the rotor, which, in the case of the figure below, is approximately 5.5 K for an angular velocity of $\omega = 1.5$ rad/s and with $T_{hot} = 328$ K. It is important to emphasize that the analysis obtained from the thermal camera provides a conservative estimate of ΔT on the rotor, as it is impossible to monitor the hottest portion of the rotor, which is submerged in water. Furthermore, as explained in section 3.2.2, ΔT is related to the frequency of the thermomagnetic cycle and, consequently, to the angular velocity of the rotor. Specifically, at higher speeds, ΔT tends to decrease since the system has less time to exchange heat with the thermal sources.

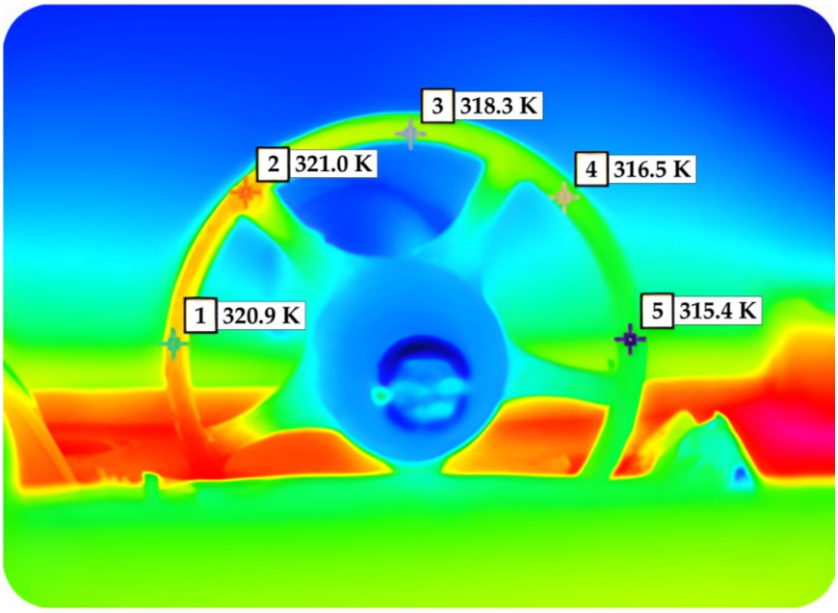

Figure 6-27: Thermal map of the TM-In-based rotor obtained with an infrared camera with T_{Cold}=300 K, T_{Hot} = 328 K and a frequency of 0.24 Hz.

Figure 6-28 shows the expected magnetic work calculated for an ideal cycle with a fixed temperature span of 4 K in width and centered around Tm. It is observed that the maximum magnetic work occurs near the critical temperature, decreasing to zero at higher temperatures due to the minimal contribution of the paramagnetic phase.

Expanding the temperature range increases the output magnetic work, a similar effect observed when increasing the magnetic field span (Appendix 8.4).

Referring to the result of the magnetic work calculation for TM-In obtained from the previously experimental measurements (5.0±0.3 J/kg), it can be observed that this closely aligns with the maximum calculated value of 4.8 J/kg for a cycle centred at 314 K, characterized by an overall temperature difference of only 4 K.

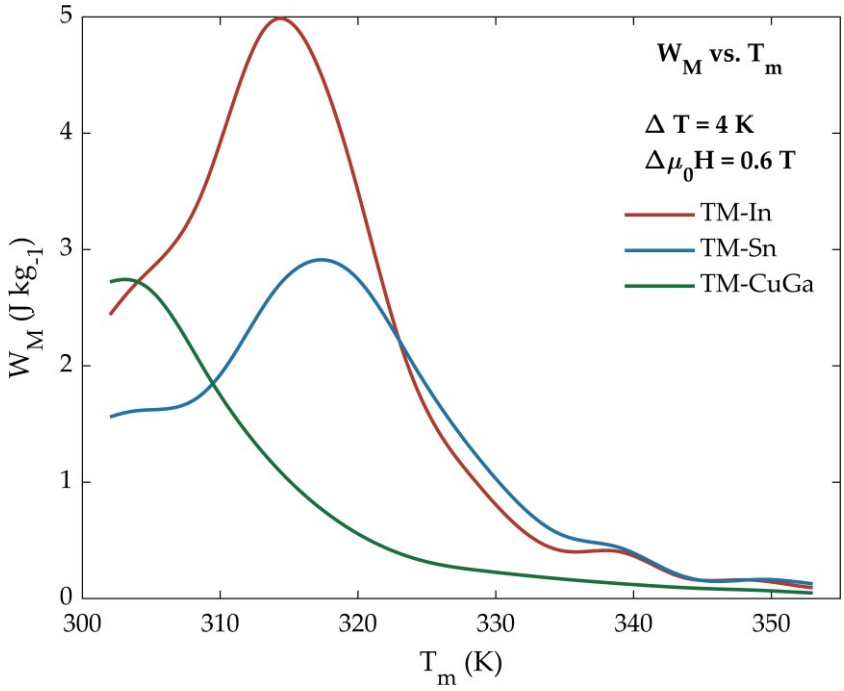

***Figure 6-28**: FoM as a function of the mean cycle temperature T_m, with the temperature difference between the cold and warm sources held constant at 4 K. The FoM is computed using equation 3.15, based on the surfaces M(T,H) data presented in Figure 6-19.*

These simulations emphasize the importance of using materials that undergo a magnetic transition precisely within the operational temperature range of the TM device. This range is determined not only by the thermal source temperatures but also by the actual heat transfer during the cycle.

These findings confirm that heat exchange at the interface between the rotor and the surrounding exchanging fluid currently limits the power output of the TM device. Enhancing this heat transfer, for example by increasing the surface-to-volume ratio

of the active rotor, is an essential goal for improving the power and efficiency of TM generators.

To address this issue, it is crucial to determine the effective temperatures reached by the active material during the cycle and how these temperatures vary with rotation. Future research will include new experiments, thermographic analyses, and finite element simulations of the complex thermodynamic system to achieve this objective. These efforts will facilitate accurate estimations of the heat absorbed by the active material from the warm thermal source, enabling the calculation of efficiencies in the TM energy conversion processes.

To benchmark these results against the current state of the art in TM generators, the electric power output achievable by connecting the motor to a generator with known specifications was estimated. A miniature two-phase electric generator optimized for low RPM operation, featuring a speed constant of 2 $rads^{-1}$ V^{-1} and an internal winding resistance of 1300 Ω, was considered (Appendix 8.6). Utilizing the tandem rotor of TM-In, the TM motor is projected to yield a maximum electric power output of 1.2 mW at an angular speed of 7.3 $rads^{-1}$. When normalized by mass or volume of the active magnetic material, this corresponds to an output electric power of 2.6 W/kg or 20.4 mW/cm^3, respectively. Notably, this estimated electric power significantly exceeds that achieved by a comparable Curie wheel utilizing a Gd ring (0.45 mW/cm^3), as reported by R. A. Kishore et al. [91].

The large difference in power output observed between the results obtained in this thesis and those reported in the literature using Gd is greater than the one calculated in Figure 6-20. This is because, as explained at the beginning of this section, the simulation assumes that the TM material reaches the temperatures of the thermal sources, a scenario that is highly unlikely in real applications, where the TM material experiences far lower temperature gradients, making the positioning of the Curie temperature crucial.

Similarly, static TM devices prototypes employing Gd and LaFeSi-based materials have demonstrated average power densities below 0.3 mW/cm^3 [88], [164]. These findings underscore the potential of the TM motor prototype to serve as an effective test bench for optimizing TMG designs, with the ultimate goal of developing efficient and powerful devices.

6.1.3 Additive Manufacturing of NiMnSn and NiMnIn

In the previous section, it was highlighted how thermal properties of the active thermomagnetic materials are of fundamental importance for low-grade heat recovery applications. Moreover, the comparison between the measurements performed and the simulations carried out emphasized that the heat exchange with the thermal sources of the active material, especially when the material is in composite form, represents the bottleneck for TM applications.

A similar argument applies to MC applications, where the two figures of merit (ΔS_M and ΔT_{ad}) not only depend directly on ΔM, but are also linked to the heat capacity c_P (eq. 3.6) [165], [21]. Finally, for both TM and MC applications, the higher the thermal diffusivity of the material, the higher the operating frequency achievable for a potential device, thereby increasing the efficiency of the thermodynamic cycles per unit of time.

A possible approach to enhance the heat exchange properties of the composite without affecting its magnetic properties is to modify its geometric characteristics. For instance, by increasing the surface-to-volume ratio of the active material, the contact surface between the material and the thermal sources is enlarged, which consequently increases the amount of heat exchanged between the system and the environment per unit of time. Additive manufacturing (AM) allows for excellent control over the geometric characteristics of a composite and represents a promising solution for exploring this approach.

AM of components with functional properties tailored by design is a topic of widespread interest today, as it enables the production of versatile products with different geometries. Similar to other technological fields, AM is emerging as a viable alternative to conventional manufacturing methods due to its ability to address challenges related to poor processability. Additionally, many AM techniques, particularly those involving thermoplastic polymers, are now widely accessible [166], [167], [168].

AM includes techniques that print directly from raw metallic materials; however, these methods often result in alloy formation during the printing process, making it challenging to achieve the desired composition of the alloy. Even when using pre-alloyed powders, metal AM requires melting the alloy, which can alter or degrade the properties of magnetic materials. On the other hand, the most common and accessible AM technique, Fused Deposition Modeling (FDM), uses polymer-based materials. This method is gaining increasing attention because polymeric materials can incorporate various types of fillers to provide functionality to the printed parts. The low melting temperatures of typical polymers prevent the alteration of the

functional powder during processing. In this context, the polymer binder in FDM does not contribute to the magnetic properties but serves to maintain the structural integrity of the part and can act as a protective layer, preventing corrosion of the functional powders [169], [170], [171].

The aim of this work is to fabricate AM rotors based on NiMnSn and NiMnIn (hereafter referred to as AM-Sn and AM-In) with different thicknesses and to test their TM properties using the device described in Section 5.5. The FDM method for producing the composite filament follows the approach proposed by A. D. Garcia et al. [145], which enables the simple and reproducible fabrication of a composite in which the functional powders are well distributed within the polymer matrix.

The polymer PolyEthylene Terephthalate Glycol (PETG) was selected as the matrix for the composite because, unlike other polymers commonly used in 3D printing, it exhibits low thermal shrinkage, excellent moisture resistance, and thermal stability within the temperature ranges where the rotors will be tested. The printing temperature of PETG is 230°C, which, although generally higher than that of other commercial polymers, is still low enough not to compromise the magnetic properties of the powders.

The synthesis method of the composite, outlined in Figure 6-29, involves using the 3D printer Prusa MK3S for printing both the polymer and the functional composite, as well as the filament maker for producing the composite filament. Both instruments are described in Section 4.2.3.

The magnetic materials used have the same nominal compositions as the TM-Sn and TM-In samples described in Section 6.1.1. Powders for both samples were produced following the procedure described in Section 4.2.1.

The process consists of printing several sets of capsules with height of 4.6mm and radius of 1.7mm in PETG (a). Subsequently, NiMnSn and NiMnIn powders are inserted into the capsule cavities until they are fully filled (b). Using a heated tip, the capsule sets are sealed (c) and then cut to obtain individual capsules (d). The capsules were designed and printed so that the volume ratio between the polymer and the functional powders is nominally 50%.

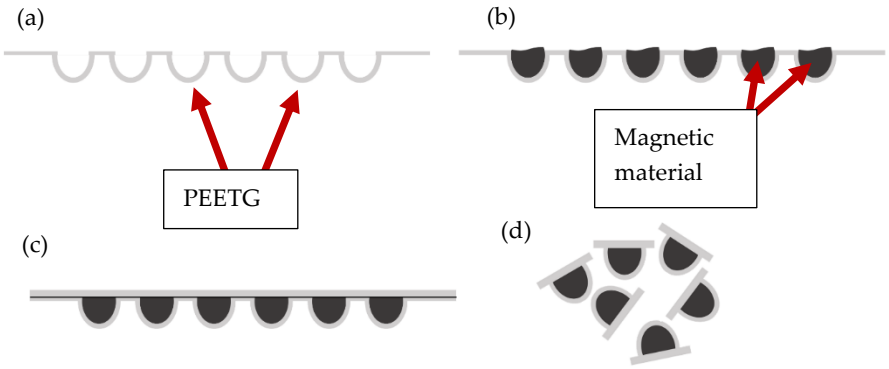

***Figure 6-29**: schematic diagram illustrating the process for producing the magnetic capsules in four steps: (a) printing PETG capsules, (b) filling them with magnetic powders, (c) sealing the capsules, and (d) cutting them into individual units.*

Once the capsules are prepared, the synthesis of the composite filament can proceed. This is done using the filament maker outlined in Figure 6-30. The instrument transports the capsules containing the magnetic powders through a screw mechanism, through four heaters, each of which can be set to different temperatures.

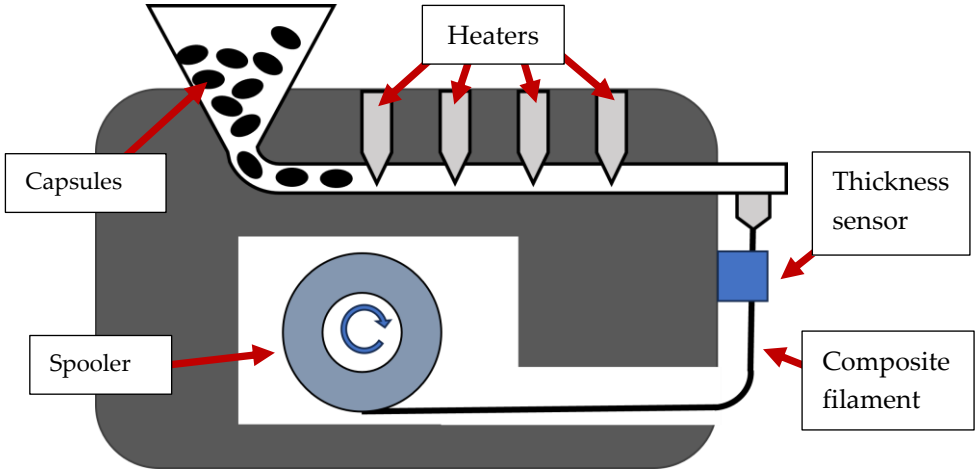

***Figure 6-30**: Schematic diagram of the 3devo NEXT 1.0 Advanced extruder with all relevant components highlighted and labeled.*

The quality of the filament and the optimal dispersion of the powders within the polymer matrix are closely linked to the selection of these four heater temperatures. The composite filament then passes by cooling fans, which allow it

to solidify, and through a sensor that monitors its thickness in real-time. Finally, the composite filament is spooled onto a reel.

The extruder used for the synthesis of the filament does not allow for the direct melting of the capsules filled with magnetic powders. For instrumental reasons, both before and after the insertion of the powders, it is necessary to pass PETG-only pellets through the system. This results in a non-uniform distribution of the powders along the filament, with the highest concentration in the central region. However, given the overall length of the composite filament compared to the little portion required for printing, it can be reasonably assumed that the central sections of the filaments have a homogeneous distribution.

Once the composite filaments are obtained, they are magnetically characterized by measuring magnetic susceptibility as a function of temperature. This allows us to verify if and how the synthesis process temperature has affected the magnetic transitions of the composite filaments. Additionally, isothermal curves are measured at T = 100 K as a function of the applied magnetic field to calculate the actual percentage of powders embedded within the PETG matrix.

Figure 6-31 shows the comparison between TMA measurements of the powders and those of the composite for both samples. It can be observed that the Curie transition of the reference powder and the composite with NiMnSn is broader than the TMA measurement presented in section 6.1.1.1 conducted on TM-Sn sample.

This discrepancy is due to the fact that, to obtain sufficient material (approximately 20 g) for the AM composite, six different samples of NiMnSn with the same nominal compositions were synthesized separately, ground, and then combined. The broader Curie transition is therefore attributed to slight compositional differences among the six samples, which, when measured together, lead to this result.

Despite this, the ferro- to paramagnetic transition remains evident, confirming the successful production of a functional AM composite. Regarding the comparison between NiMnIn reference powders and their respective composite, the measurements do not reveal significant differences, aside from a slight decrease in the slope of the transition.

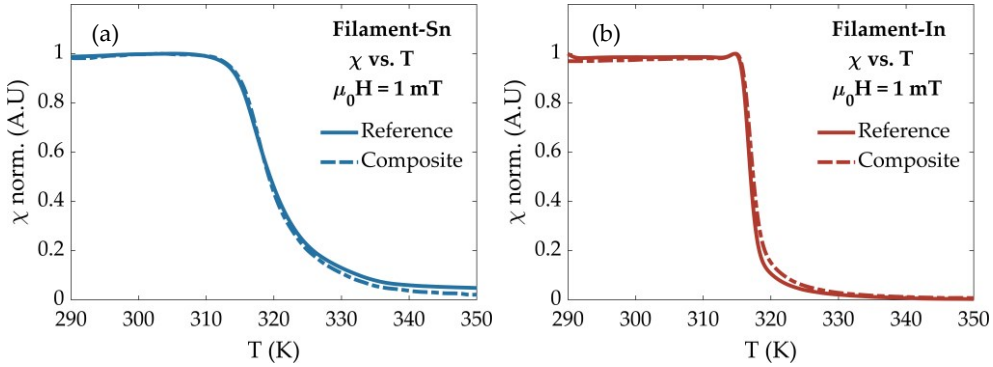

***Figure 6-31**: Comparison of ac magnetic susceptibility in low applied magnetic field of 1 mT as a function of temperature measurements between powder (continue line) and composite (dashed line) for NiMnSn (a) and NiMnIn (b).*

Figure 6-32 presents the measurements conducted using the stationary pendulum magnetometer, employed to determine the concentration of magnetic powders within the composite. These measurements consist of isothermal curves taken at T = 100 K up to a magnetic field of 1 T for both the reference powders and the composite. The magnetization values in the figure are reported per unit mass, and by multiplying for a percentage factor the reference magnetization curve to match that of the composite, it is possible to determine the actual mass of magnetic powders within the composite.

The comparison reveals that the concentrations in the two filaments differ significantly, with only the NiMnIn-based composite achieving the nominal percentage (50%), Meanwhile, the NiMnSn-based composite reaches a concentration of 21%. The wide variation in the obtained concentrations suggests the need for a more reproducible method, which will be explored in future work.

From a geometrical standpoint, the composite filaments exhibit uniform thickness (1.75 mm in diameter) and are suitable for 3D printing. The printer used for fabricating the AM-Sn and AM-In rotors is the Prusa MK3S, which allows for the nozzle of the extruder to be changed in order to adjust the minimum thickness of the

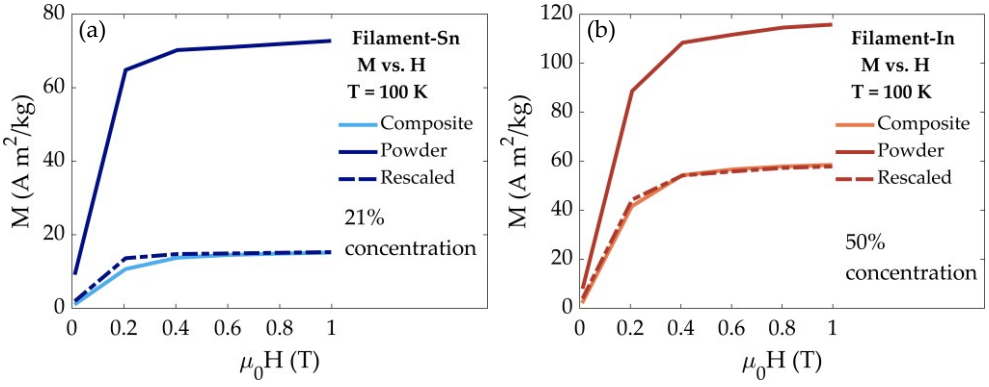

***Figure 6-32**: Isothermal curves per unit mass at constant temperature T=100K over the magnetic field applied of NiMnSn (a) and NiMnIn (b). The magnetization curves of the powder are reported dark coloured, the composite light coloured, and the rescaled powder curves dashed dark coulored.*

prints. Various printing temperatures were tested for the rotor filaments (200°C – 260°C), and setting the extruder temperature at 240°C was identified as the best configuration in terms of print quality. The geometric characteristics of the produced rotors are listed in Table 6-8. For both AM-Sn and AM-In, two rotors were printed with nominal thicknesses of 0.6 mm and 0.8 mm, while the heights of the rotors were calculated to ensure that all rotors have the same volume. This choice allows for the evaluation of how the thermomagnetic properties of the rotors depend on their thickness (and consequently the surface-to-volume ratio). By maintaining the same volume for all rotors, the mass of magnetic material per radial unit remains consistent across all samples.

Based Heusler	Thickness [mm]	Height [mm]	Code name
NiMnSn	0.8	6	AM-Sn-0.8
NiMnSn	0.6	8.4	AM-Sn-0.6
NiMnIn	0.8	6	AM-In-0.8
NiMnIn	0.6	8.4	AM-In-0.6

Table 9: Table summarizing the characteristics of the produced rotors. The first column lists the Heusler alloy used for the composite, the second and third columns show the rotor thickness and height, respectively, and the fourth column provides the names assigned to the rotors for subsequent analyses.

As seen from the magnetic field mapping generated by the set of permanent magnets used in the TM tester, shown in Figure 5-4, the field intensity along the axis parallel to the height of the rotors remains constant.

Figure 6-33 shows, as an example, a photograph of two of the rotors used for the TM tests and a portion of the filament produced using the method described so far.

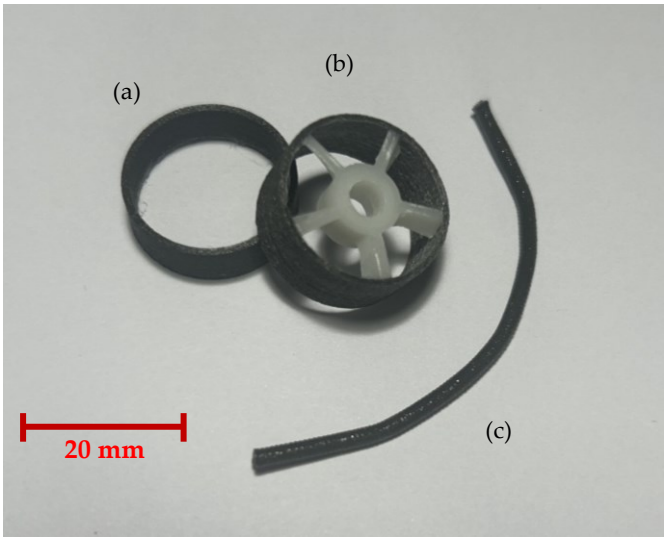

***Figure 6-33**: Photograph of AM-Sn-0.8 (a), AM-In-0.6 (b) and a portion of the AM-In filament (c).*

For each rotor, a support compatible with the TM tester shaft (Section 5.1.3) was 3D-printed to conduct the TM tests.

Figures 6-34 and 6-35 show the mechanical power measurements as a function of the angular velocity of the TM tester shaft for the NiMnIn- and NiMnSn-based rotors, respectively. The measurements were performed following procedures analogous to those described in Section 6.1.2. Given the significant difference in powder concentration between the two composites, AM-In and AM-Sn, the power measurements are reported per unit mass of the functional powder within the rotors.

In Figure 6-34, the results for the AM-In-0.6 (left) and AM-In-0.8 (right) rotors are reported, with the hot source temperature increasing from 313 K to 338 K, while the cold source temperature was kept constant at room temperature. The mechanical power curves as a function of rotor speed exhibit similar trends for both thicknesses, and in both configurations, the hot source temperature corresponding to the highest power output within the studied angular velocity range is T_{hot} = 323 K. Notably, for

Thot values above 338 K, the curves no longer show a peak, and the power output decreases linearly with increasing angular velocity.

To explain this behavior, it is helpful to briefly analyse how the device measures mechanical power; a more detailed discussion is provided in Appendix 8.1. The mechanical power measured by the TM tester is defined as the product of the shaft torque, measured by the two-phase electric motor, and the rotor's angular velocity. In regions of low angular velocity, mechanical power is generally low due to the small values of ω, whereas at high angular velocities, power decreases due to the low torque exerted by the rotor on the shaft. These characteristics lead to the presence of a mechanical power peak in an intermediate region, indicating an angular velocity (and thus a resistive load) at which the device achieves optimal output. The curves in Figure 6-34 that do not exhibit a mechanical power peak represent configurations in which optimal performance occurs at lower angular velocities.

In Figure 6.34, the power curves as a function of the rotor's angular velocity for the AM-In-0.8 sample appear noisier than those for the AM-In-0.6 sample. This is due to the fact that, as previously described, the shaft torque and angular velocity values are obtained from an average of the measurements recorded over one minute. If the rotational speed is not constant during the measurement, the mechanical power value will not align with the expected trend. Given the high sensitivity of the TM tester, even a slight rotor imperfection or a minor temperature variation in the thermal sources can result in increased noise in a thermomagnetic power curve.

A comparison of how the mechanical power output of the TM tester varies with rotor thickness will be provided later in this section.

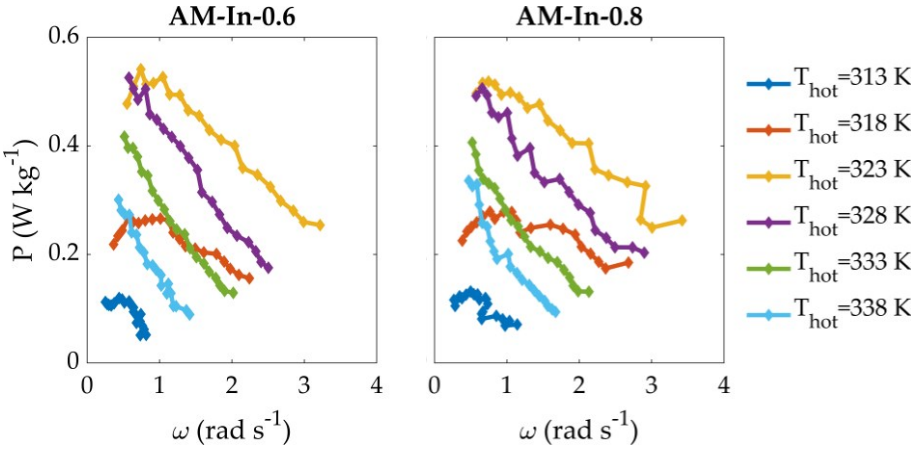

***Figure 6-34**: Mechanical power output of the TM tester as a function of angular speed of the shaft, achieved by adjusting the temperature of the warm source T_{Hot} and the external resistive load, using AM-In-0.6 (left) and AM-In-0.8 (right). The cold source temperature is kept constant at 297 K. Each data point represents the average of measurements taken during both increasing and decreasing load sweeps. Solid lines are included to guide the interpretation of the data.*

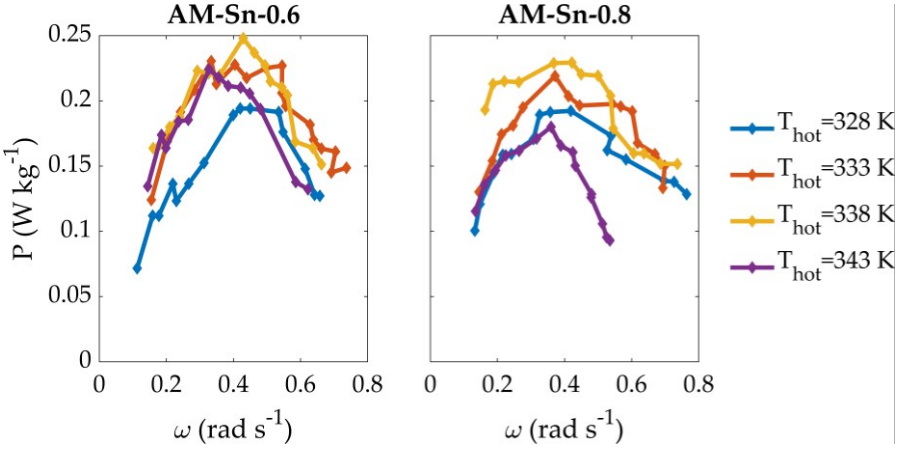

***Figure 6-35**: Mechanical power output of the TM tester as a function of angular speed of the shaft, achieved by adjusting the temperature of the warm source T_{Hot} and the external resistive load, using AM-Sn-0.6 (left) and AM-Sn-0.8 (right). The cold source temperature is kept constant at 297 K. Each data point represents the average of measurements taken during both increasing and decreasing load sweeps. Solid lines are included to guide the interpretation of the data.*

In both the AM-In and AM-Sn analyses, the variation in angular velocity does not follow a linear trend, and the ω range differs significantly between the two sets of measurements. This is because the external load was varied between each measurement point, and the rotor's angular velocity was measured over a one-minute interval, with the average value reported. For low external load values, the rotor can achieve high instantaneous speeds, reducing the time available for heat exchange with the sources, which subsequently leads to a decrease in instantaneous rotational speed. This can result in an average angular velocity lower than expected. However, this phenomenon typically occurs only at low external loads, where the power curve is far from its peak.

The mechanical power peaks from the analyses shown in Figures 6-34 and 6-35 are plotted as a function of the hot source temperature in Figure 6-36, allowing a comparison of how the system's output varies with rotor thickness and an overall comparison between the AM-In and AM-Sn composites. As previously mentioned, the power curves are similar when varying rotor thickness. However, the peak analysis reveals an approximately 5% increase in maximum power when the rotor is thinner, confirming the hypothesis that power generation is linked to the increased surface-to-volume ratio of the rotor.

The comparison between the two composites shows that the power output of AM-In is about 55% higher than that of AM-Sn. This difference is greater than that observed previously using MM composites (Section 6.1.2). The discrepancy is likely due to the difference in the concentration of functional material within the composite. While, from a magnetic perspective, the difference in concentration can be corrected by normalizing to the effective mass of magnetic material, from a thermal perspective, the composite with a lower concentration of functional material will have lower thermal conductivity and higher specific heat due to the greater presence of polymer relative to the alloy.

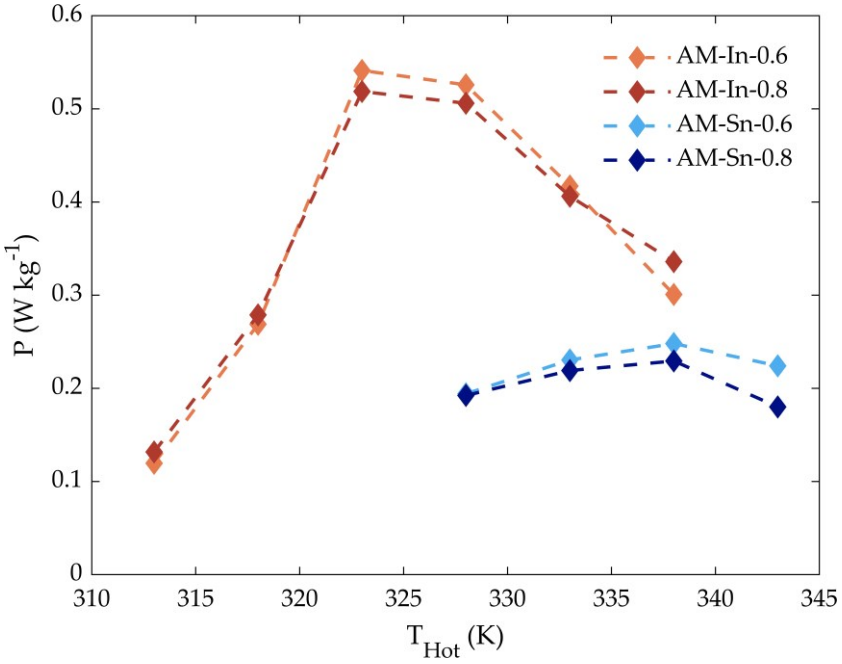

***Figure 6-36**: Maximum mechanical power output as a function of the warm reservoir temperature for AM-In-06 (light red), AM-In-08 (dark red), AM-Sn-06 (light blue), and AM-In-06 (dark blue). The solid lines are provided as visual aids.*

When comparing the mechanical power peaks as a function of T_{hot} for the hand-crafted TM-In and TM-Sn composites in Figure 6-24 with the 3D-printed AM-In and AM-Sn composites in Figure 6-36, two main differences emerge: the curves for the AM composites exhibit a peak, while those for the MM composites show a linear trend as the hot source temperature increases, and the mechanical power values per unit mass differ significantly between the two.

Starting with the first difference, the AM-In and AM-Sn rotors display a peak at T_{hot} = 323 K and T_{hot} = 338 K, respectively, with the mechanical power values decreasing as the hot source temperature rises. This occurs because the active material within the rotors actually reaches the Curie temperature of the alloys, and as the source temperature increases, a larger portion of the rotor transitions to the paramagnetic phase, reducing the ΔM between the coldest and hottest points on the rotor. This phenomenon is presumably absent in the MM rotors, which likely never reach sufficiently high temperatures to exhibit this effect.

The second significant difference lies in the mechanical power values per unit mass, which are 80% lower for the AM composites. This discrepancy is likely due once

again to the difference in concentration of metallic alloy powder within the two composite types. While the AM composites more easily reach temperatures closer to that of the hot source due to their geometric characteristics, the higher proportion of plastic material in the AM composites compared to the MM ones results in lower thermal conductivity. This leads to a reduced short-term heat exchange, shrinking the temperature difference across the rotor and, consequently, the torque generated.

The results obtained using the 3D-printed AM composites reveal a promising relationship between the geometric characteristics of the rotors and their TM performance. Despite the efficiency results still lower than those achieved with the MM composites, future studies will focus on developing a method to increase and homogenize the concentration of active material within the composite, as well as test new geometries.

Since it has been established that an increase in the surface-to-volume ratio enhances heat exchange between the active material and the thermal sources, future studies will focus on testing new geometries aimed at maximising this parameter. For instance, grooves could be added to the rotors, or arrays of thin disks could be employed.

6.2 FeNiGaMnSi HEAs

This section focuses on the investigation of two compositions within the FeNiGaMnSi-based HEAs class. The study encompasses a comprehensive magnetic and structural characterization of the samples, including measurements of magnetic susceptibility, temperature-dependent magnetization, compositional analysis via EDX, and structural evaluation using XRD. Moreover, the synthesis challenges are discussed, with particular emphasis on the difficulties in stabilizing the compositional phase through thermal treatments. The magnetic characterization data are subsequently utilized to compute the figures of merit for thermomagnetic and magnetocaloric applications. Lastly, the powders derived from the two samples are used to fabricate rotors for measuring thermomagnetic properties, following a procedure similar to that outlined in Section 6.1.2.

6.2.1 HEAs characterization

The initial synthesis targeted a set of HEAs with a composition of $Fe_{27}Ni_{27}Ga_{19-x}Mn_{16+x}Si_{11}$, aiming to optimize tunability of the Curie transition within a temperature range close to room temperature. FeNiGaMnSi-based HEAs, aside from having Curie temperatures suitable for magnetocaloric applications [136], are mostly composed of abundant, non-critical, and cost-effective elements (Ga being a minor constituent of these compounds).

In a similar manner to the synthesis of NiMn-based Heusler alloys described earlier, the set was produced using an arc furnace, where the constituent elements were melted in proportions designed to achieve the desired composition. An additional 1.5% of Mn was included to compensate for losses due to evaporation during the melting process. The samples underwent three melting cycles, with each cycle involving flipping and weighing the samples to enhance homogeneity and monitor material loss. After synthesis, the samples were heat-treated at 973K for 1 hour [136].

Figure 6-37 presents the temperature-dependent magnetic susceptibility measurements, performed using a TMA. These measurements were conducted during the heating phase within a temperature range of 145 K to 460 K, under an applied AC magnetic field of 1 mT. The measurements indicate compositional inhomogeneity in most of the analyzed samples, as evidenced by the presence of multiple Curie transitions. The samples with x= 0, 2, and 4 display a sharp drop in magnetic susceptibility at approximately 265 K, suggesting a common

compositional phase. At higher temperatures, these samples undergo additional transitions at 420 K, 386 K, and 337 K, respectively.

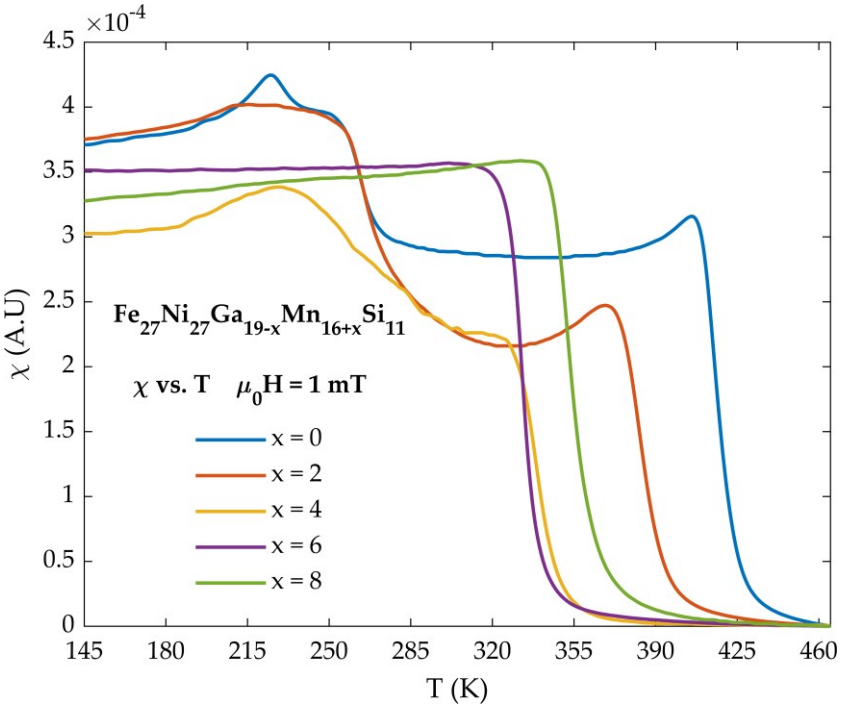

***Figure 6-37**: ac magnetic susceptibility in low applied magnetic field of 1 mT as a function of temperature for the HEAs set $Fe_{27}Ni_{27}Ga_{19-x}Mn_{16+x}Si_{11}$.*

Furthermore, the sample x=0 exhibit a third magnetic phase with a Curie temperature at 230 K. In contrast, the samples with higher Mn content exhibit magnetic single phase behavior, characterized by a single, complete transition from the ferromagnetic to the paramagnetic phase at 331 K and 349 K for the x = 6 and x = 8 samples, respectively. Since TMA measured susceptibility is not correlated with magnetization, estimating the volume (or mass) ratio of two coexisting compositional phases in the measured sample based on the relative height of their signals would be inaccurate.

Given the homogeneity issues observed, the role of thermal treatment in the formation of secondary phases was explored. To investigate this, several fragments were obtained from the x=0 alloy, with a nominal composition of $Fe_{27}Ni_{27}Ga_{19}Mn_{16}Si_{11}$, and each fragment underwent a one-hour heat treatment at different temperatures.

Figure 6-38 presents the magnetic susceptibility measurements of four fragments from the same sample. Prior to the heat treatments, the fragments were measured individually to confirm consistency in their responses, followed by thermal treatments at 973K, 1073K, and 1173K for one hour each. The results show a drastic impact of the heat treatment on one of the two primary magnetic phases, where the Curie temperature drops from 420 K (as-cast) to 345 K (after treatment at 1173 K). Conversely, the various annealing temperatures appear to have minimal effect on the second magnetic phase, which exhibits an almost unchanged Curie transition around 260 K.

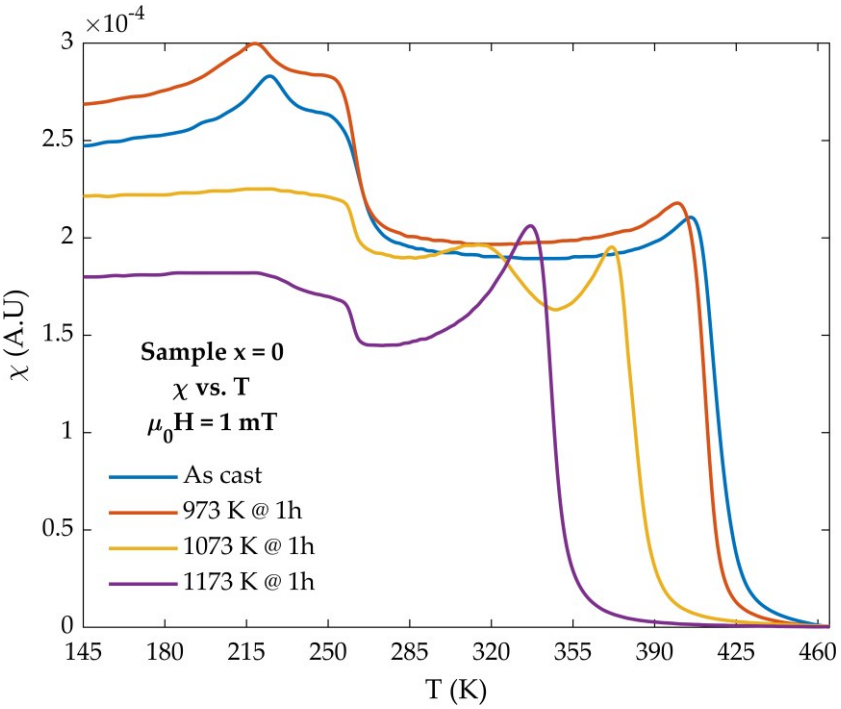

***Figure 6-38**: ac magnetic susceptibility in low applied magnetic field of 1 mT as a function of temperature of different fragments of the HEA sample x=0 heat treated at different temperature. As cast (blue), 973 K (orange), 1073 K (yellow), 1173 K (purple).*

The investigations shown in Figure 6-28 demonstrate a significant correlation between heat treatment and the compositional phases formed within the sample, highlighting the considerable difficulty in synthesizing monophase samples. This aspect of HEAs is widely discussed in the literature and applies to a broad range of different alloys [172], [173], [174]. Since one of the objectives of this thesis is to evaluate the magnetocaloric and thermomagnetic properties of HEAs, further

characterizations for these purposes will be carried out only on the x=6 and x=8 samples whose composition are $Fe_{27}Ni_{27}Ga_{13}Mn_{22}Si_{11}$ and $Fe_{27}Ni_{27}Ga_{11}Mn_{24}Si_{11}$. For this reason, Figure 6-39 provides the TMA magnetic susceptibility measurements as a function of temperature for the samples whose study will be continued. For consistency with Table 6-1, from this point onward, the x=6 and x=8 samples will be referred to as HEA-Ga13 and HEA-Ga11, respectively. The measurements shown in Figure 6-39 were conducted on different fragments of the same samples compared to the measurements in Figure 6-37, as the latter underwent additional heat treatments for the investigations described earlier. However, the new measurements are magnetically identical to the previous ones.

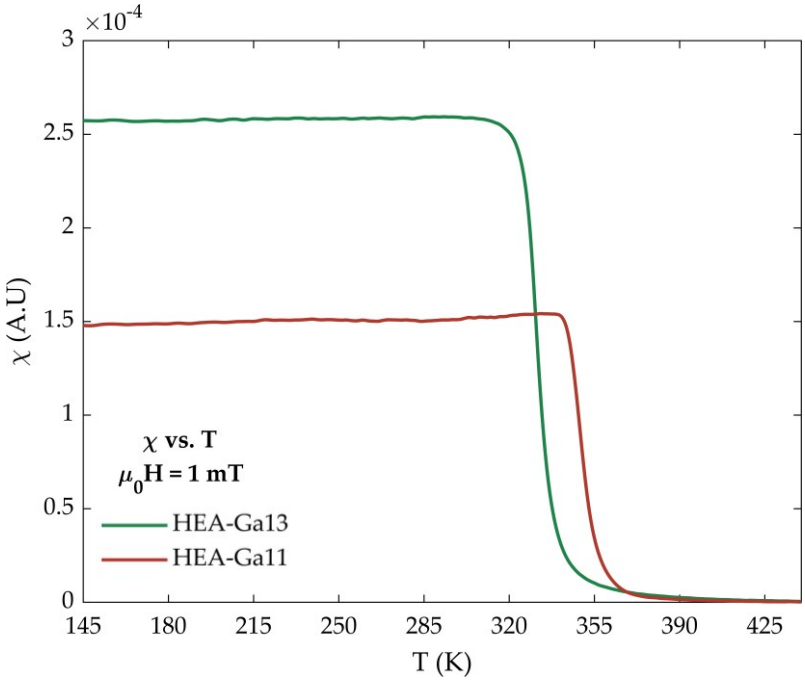

***Figure 6-39**: ac magnetic susceptibility in low applied magnetic field of 1 mT as a function of temperature for the samples HEA-Ga13 (green) and HEA-Ga11 (red).*

Figure 6-40 shows the magnetization curves as a function of temperature, measured using the SQUID magnetometer detailed in section 5.4. The measurements were conducted under an applied magnetic field of 1 T, with a temperature ramp rate of 2 K/min, over a temperature range from 10 K to 360 K.

Unfortunately, the Curie transitions of the two samples are close to the maximum temperature limit of the magnetometer, preventing the observation of the full ferromagnetic-to-paramagnetic transition.

The two HEAs analyzed exhibit notably different magnetization values, with the HEA-Ga13 sample showing a signal more than 20% higher than that of the HEA-Ga11 sample, despite the latter having a higher nominal Mn content. The maximum magnetization values measured at 10 K are 90.6 Am²/kg and 70.7 Am²/kg for the HEA-Ga13 and HEA-Ga11 samples, respectively. These results align with the literature [136] and are comparable to the previously discussed Heusler alloys.

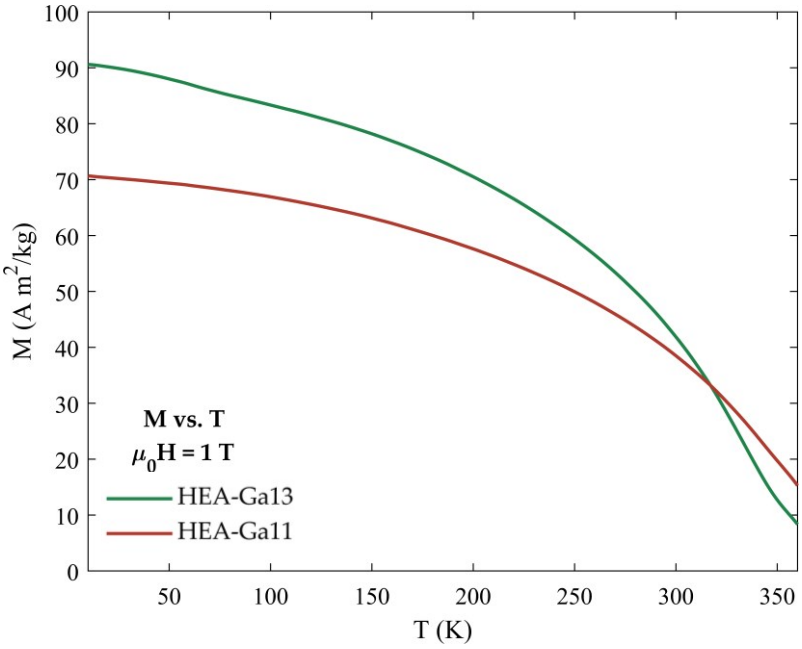

***Figure 6-40**: S.Q.U.I.D. magnetometer magnetization measures in 1T applied magnetic field as a function of temperature for the samples HEA-Ga13 (green) and HEA-Ga11 (red).*

EDX measurements were performed on both samples to determine the actual composition of the HEA alloys. The measurements involved calculating compositions in various regions of the sample, ensuring that there was no excessive discrepancy between measurements conducted on the same sample. Additionally, EDX maps were acquired, in which each element of the alloy was represented by a different colour. Figure 6-41 presents the EDX maps obtained for the HEA-Ga13 sample.

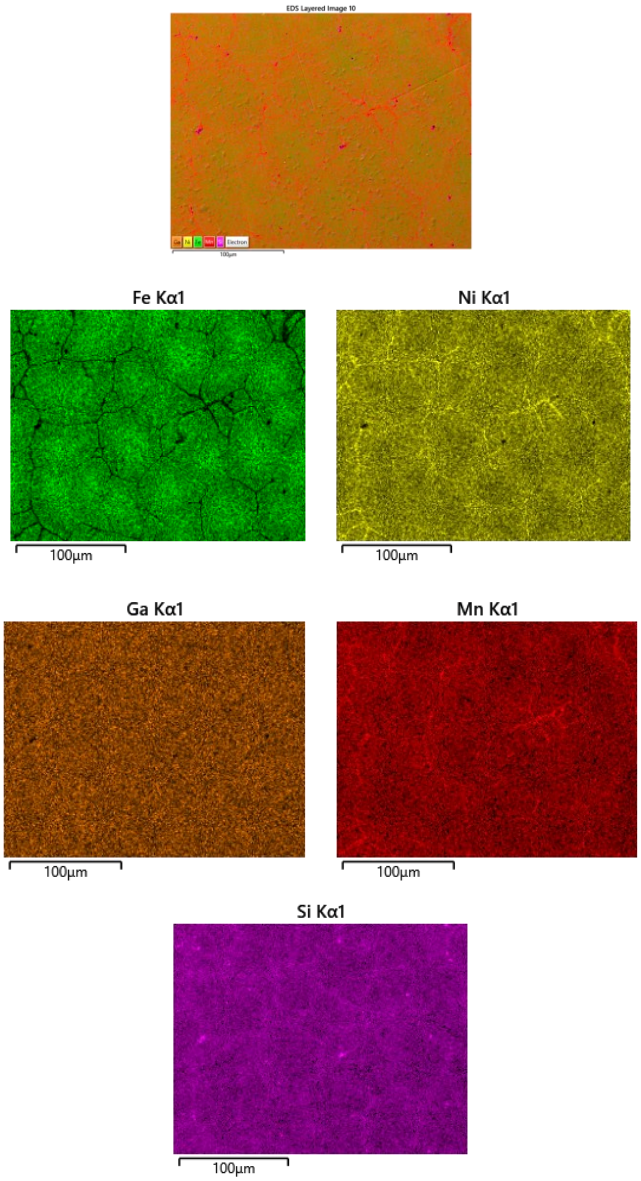

***Figure 6-41**: EDX compositional maps of the distribution of elements Fe (green), Ni (yellow), Ga (orange), Mn (red), and Si (pink) within the sample HEA-Ga13. (a) Composite image showing the distribution of all elements simultaneously. (b-f) Elemental maps highlighting the distribution of each element individually.*

Compositional measurements of the HEA-Ga13 sample reveal a nearly complete homogeneity of the alloy, except for a small secondary phase depleted in iron, easily

identifiable in the Fe EDX map presented in Figure 6-41(b). However, considering the modest amount of this phase and the absence of a corresponding magnetic signal in previously conducted magnetic characterization measurements, it is not expected to compromise the magnetocaloric and thermomagnetic properties of the HEA-Ga13 sample. The measured compositions of the primary and secondary phases are reported in Table 6-10.

Figure 6-42 shows an SEM image of the HEA-Ga11 sample, which exhibits a clear secondary phase. This phase is consistent in all analyzed regions of the sample and is distinguished in the SEM image by a darker grey shade compared to the primary phase.

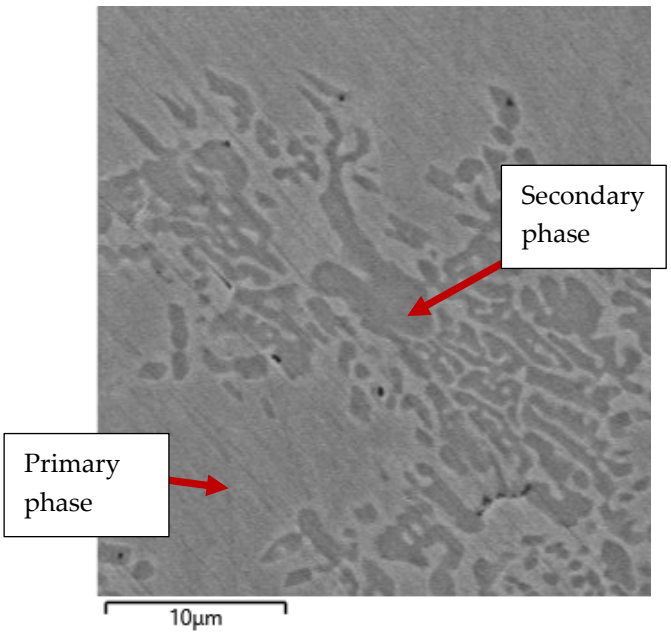

***Figure 6-42**: SEM image of the sample HEA-Ga11. The dark grey areas correspond to a secondary compositional phase of the alloy.*

Figure 6-43 presents EDX maps obtained from another region of the sample, revealing a secondary phase distribution similar to that shown in Figure 6-42. Again, Figure 6-43(a) displays a composite image where all elements are simultaneously represented, while Figures 6-43 (b, c, d, e, f) show elemental maps highlighting the distribution of each element individually.

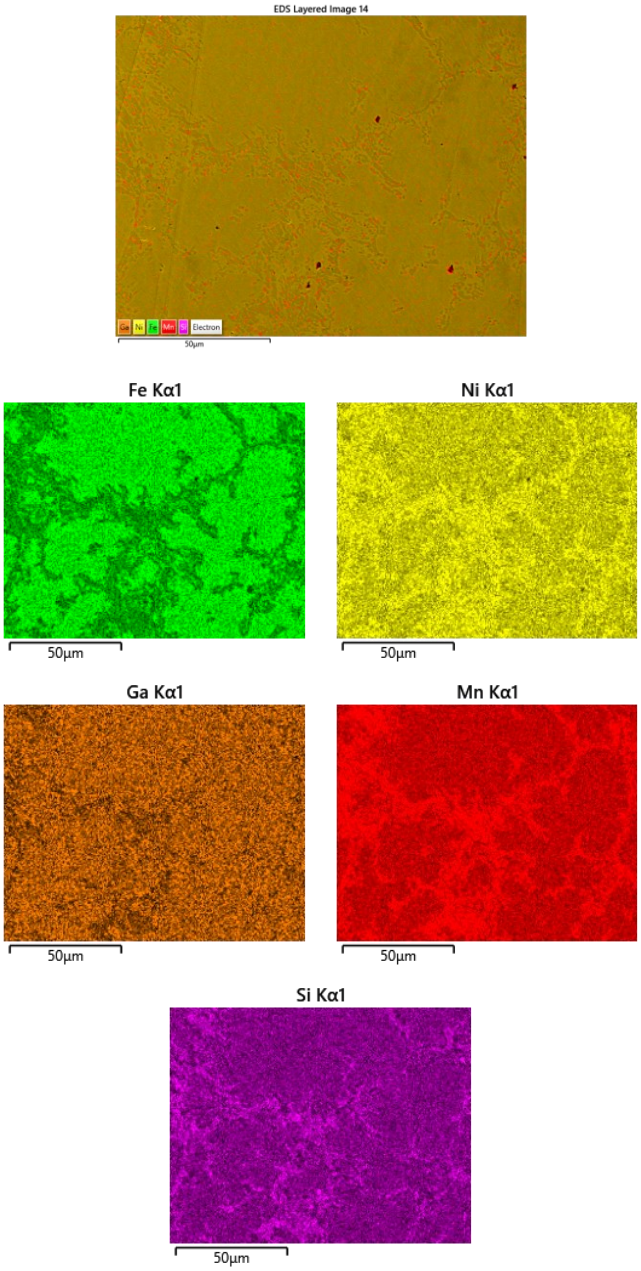

***Figure 6-43**: EDX compositional maps of the distribution of elements Fe (green), Ni (yellow), Ga (orange), Mn (red), and Si (pink) within the sample HEA-Ga11. (a) Composite image showing the distribution of all elements simultaneously. (b-f) Elemental maps highlighting the distribution of each element individually.*

Following the EDX analyses and the magnetic characterization conducted, a table is provided that lists the measured compositions of both the primary and secondary phase.

Sample	Nominal composition	Fe (%)	Ni (%)	Ga (%)	Mn (%)	Si (%)
HEA-Ga13	$Fe_{27}Ni_{27}Ga_{13}Mn_{22}Si_{11}$	**26.1**	**26.8**	**14.1**	**24.1**	**9.0**
2nd phase		12.9	34.4	13.0	28.3	11.3
HEA-Ga11	$Fe_{27}Ni_{27}Ga_{11}Mn_{24}Si_{11}$	**25.6**	**27.1**	**11.9**	**25.1**	**10.3**
2nd phase		12.4	31.9	6.0	33.4	16.3

***Table 10**: In the first two column are reported the samples' name and the nominal composition of the synthetized HEAs. In the other columns are reported the actual compositions measured with EDX of both primary (in bold) and secondary phase.*

The compositional EDX measurements exhibit good agreement between the nominal compositions and the measured main phase, and the nominal values deviate by no more than 2% from the measured ones. As previously mentioned, the secondary phase in the HEA-Ga13 sample is present in a minimal quantity and does not significantly affect the magnetic properties of the sample. Conversely, the secondary phase in the HEA-Ga11 sample is present in non-negligible quantities and is likely responsible for the low magnetization value observed in the temperature-dependent magnetization measurements. Despite the non-negligible presence of a secondary phase, the TMA measurements do not reveal any additional magnetic phase beyond that characterized by the Curie transition at 349 K. This suggests that the composition of the additional phase is characteristic of a non-ferromagnetic compound.

A preliminary X-ray diffraction analysis was conducted on HEA-Ga13 and HEA-Ga11 (Appendix 8.7). The former is single phase with a cubic structure ($Fe_{0.77}Ga_{0.23}$ like) with cell parameter a = 2.88(1) Å. In contrast, the analysis of the HEA-Ga11 sample confirms the coexistence of multiple phases, the most prominent of which is the same cubic phase in which HEA-Ga13 crystallizes with the same cell parameter. The other two phases are a cubic phase (Fe_3Si like) with cell parameter a= 5.64(1) Å

and a hexagonal phase (Ni Garutiite like) with cell parameters a=2.66(1) Å and c=4.32(1) Å.

Table 6-11 provides a summary of the key magnetic properties essential for TM generation applications of the studied HEAs. Both the finite change in magnetization over a 4 K temperature range around the Curie temperature (ΔM_{4K}) and the maximum derivative of high-field magnetization with respect to temperature ($\partial M/\partial T_{max}$) show a trend consistent with the alloys' saturation magnetization. These parameters can be used equally well for an initial assessment of the materials' potential TM performance.

Sample	T_C (K)	M_{10K} (Am^2kg^{-1})	$\partial M/\partial T_{max}$ ($Am^2kg^{-1}K^{-1}$)	ΔM_{4K} (Am^2kg^{-1})
HEA-Ga13	331	90.6	0.67	2.66
HEA-Ga11	349	70.7	0.48	1.78

***Table 11**: Summary table of the results obtained from the characterization of the synthetized HEAs. In the first column (sample), the names of the samples used are listed, as summarized in Table 6-1. The second column (TC) shows the Curie temperature measurements obtained from low-field magnetic susceptibility measurements. In the third column (M_{10K}), the magnetization value at T = 10K is calculated from magnetization measurements. The fourth column ($\partial M/\partial T_{max}$) reports the maximum absolute value of the derivative of the magnetization curve with respect to temperature. Finally, the fifth column (ΔM_{4K}) provides the difference in magnetization calculated over a temperature range of 4K around the Curie temperature of the sample.*

6.2.2 Calculation of ΔS and W_M of HEAs

In this section, the figures of merit characterizing the MCE and TM energy harvesting will be calculated, namely the magnetic entropy change ΔS (eq. 3.4) and the work produced in an ideal thermomagnetic cycle, defined in this thesis as FoM (eq. 3.15).

For both calculations, it is necessary to measure the isothermal magnetization curves. Figure 6-44 presents these curves, obtained using the stationary pendulum magnetometer described in section 5.3. Both measurements were performed by stabilizing the sample temperature and recording the magnetization as the applied magnetic field was varied up to $\mu_0 H$ = 1T. The explored temperatures range from 295 K to 400 K, with measurements taken every 5 K. Within this temperature range,

both samples exhibit their ferro-paramagnetic transition, as demonstrated in the previous characterizations. The same scale is used for both graphs in the figure, and it can be observed that the values obtained for μ_0H=1T are consistent with the M(T) measurements shown in Figure 6-40. The reported measurements show slightly higher magnetization values for the HEA-Ga13 sample compared to the HEA-Ga11 sample (by approximately 10%) within the typical temperature range of TM applications.

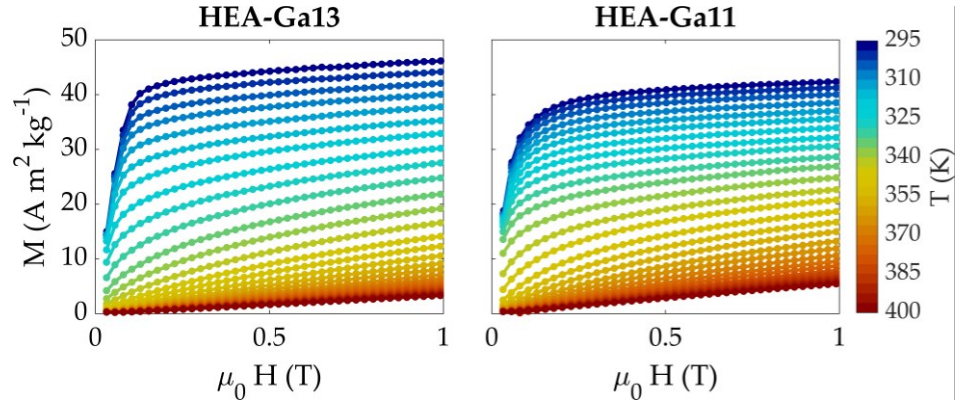

***Figure 6-44**: Isothermal magnetization curves as a function of external magnetic field collected at different temperatures for the HEA-Ga13 (left) and HEA-Ga11 (right) samples.*

The isothermal curve data of both samples are used to extrapolate the M(H,T) data required to perform the calculations of the relevant quantities. Figure 6-45 presents the M(H,T) surfaces for both samples.

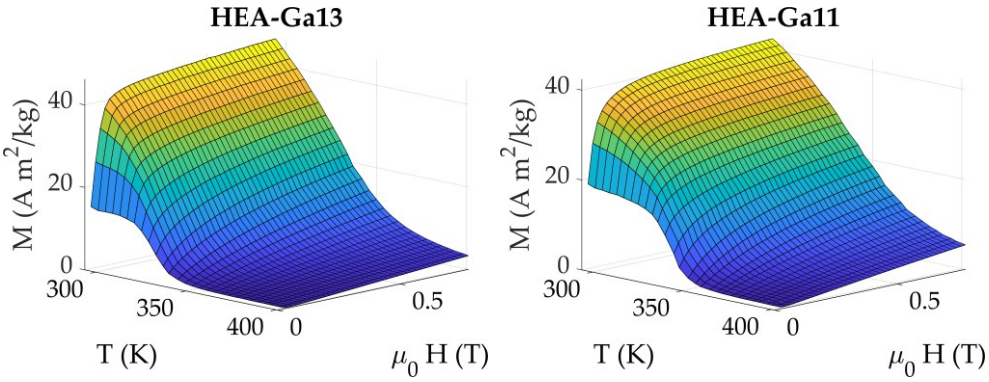

***Figure 6-45**: M(H, T) surface of the TM-Sn sample, derived from M(H) measurements conducted at various temperatures within the thermomagnetic range of interest. The yellow*

and the dark blue region correspond to the highest and the lowest values of magnetization respectively.

Once the H(M,T) surfaces are obtained, it is possible to proceed with the calculation of ΔS and W_M. Figure 6-46 presents the graph of the calculated ΔS value as a function of temperature for both HEA samples. The calculations are based on experimental data and therefore refer to a magnetic field variation of $\Delta\mu_0 H$=1T.

The HEA-Ga13 sample exhibits a minimum ΔS at the Curie temperature of the alloy (around 330 K), with a value of −0.62 J kg^{-1} K^{-1}, while the HEA-Ga11 sample shows a minimum at T = 340 K, with a value of −0.46 J kg^{-1} K^{-1}.

The synthesized HEAs show values of magnetic entropy change comparable to the highest values reported for the sub-set of rare-earth-free HEAs across the Curie transition. Furthermore, although HEAs containing rare earths exhibit higher MCE, they present low magnetic transition temperatures, unlike the HEAs discussed in this thesis, which makes them unsuitable for MC applications near room temperature.

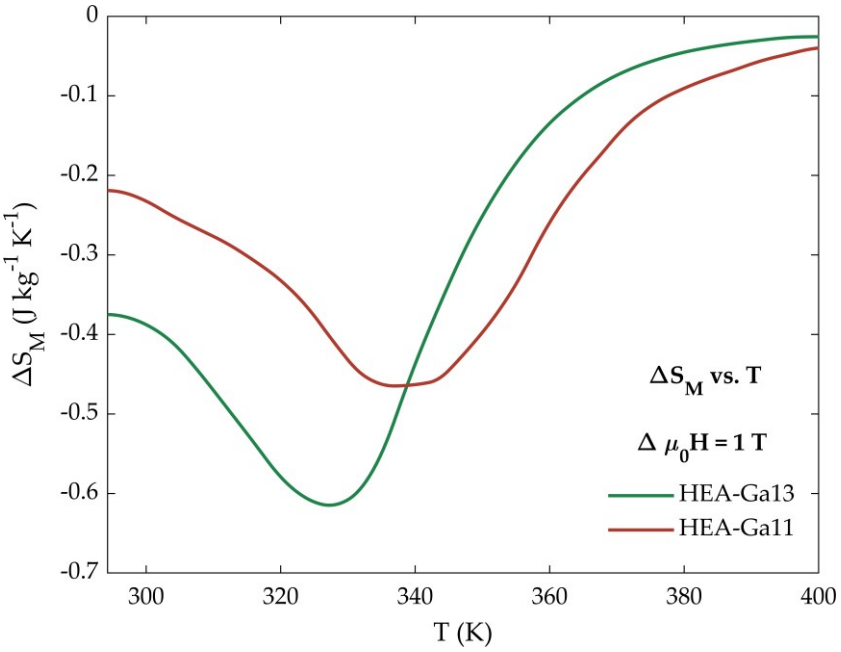

***Figure 6-46**: Temperature dependence of magnetic entropy change ΔS_M of the HEA-Ga13 (green) and HEA-Ga11 (red).*

Figure 6-47 presents a comparative evaluation of the useful magnetic work produced by the two HEAs under investigation and Gd. The analysis is conducted

under an applied magnetic field of 0.6 T, with the cold source set at 297 K and the warm reservoir varying between 300 K and 400 K. Near room temperature, Gd delivers the highest potential output due to its large saturation magnetization. At higher temperatures a thermomagnetic cycle using HEA-Ga13 or HEA-Ga11 demonstrates superior work generation, overcoming Gd at 333 K and 352 K respectively.

A key assumption in this calculation is that the integration limits for the FoM in Eq. 3.15 are aligned with the temperatures of the thermal reservoirs. While this assumption does not provide quantitatively accurate results for practical applications, it serves as an effective tool for qualitative comparisons between thermomagnetic materials. This approach helps illustrate how the FoM changes as a function of reservoir temperatures, under the approximation of either very long operational cycles or exceptionally high thermal diffusivity.

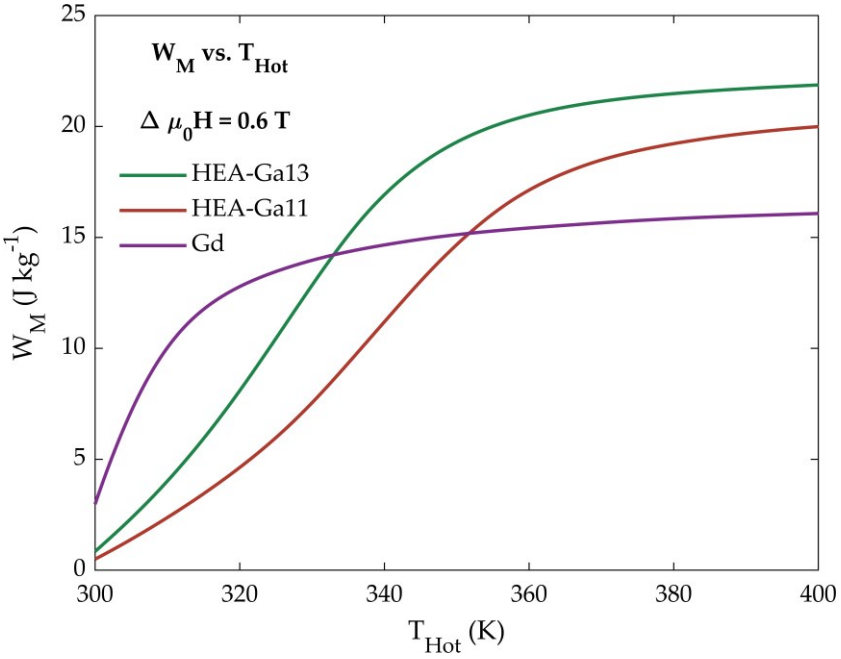

***Figure 6-47**: FoM generated by an ideal TM cycle utilizing HEA-Ga13 (green), HEA-Ga11 (red) and Gd (purple) samples as a function of the hot cycle temperature T_{Hot}. The cold temperature is held constant at 297 K, along with a magnetic field of 0.6 T. The FoM is computed using equation 3.15, based on the surfaces M(T,H) data presented in Figure 6-45.*

The calculation of the magnetic work produced in an ideal TM cycle for the two HEA samples shows that, for both materials, the work increases as the temperature

difference between the two reservoirs increases. The HEA-Ga13 sample exhibits higher magnetic work values compared to the HEA-Ga11 sample, due to higher magnetization values within the temperature range used for the calculation.

6.2.3 TM generator for HEAs testing TM properties

As outlined in Sections 4.2.1 and 4.2.2, the rotors were manufactured from an epoxy-based composite incorporating magnetic powder. The MM composites were molded into rings using water-soluble bioplastic molds, each featuring an insoluble plastic core that served as a framework to connect the rotors to the generator shaft. The rotors had an internal diameter of 18 mm, a thickness of 1 mm, and contained approximately 0.23 g of active magnetic material.

Figure 6-48 presents the measurements of the isofield magnetization curves with an applied magnetic field of 1T conducted using the extraction magnetometer, employed to determine the concentration of magnetic powders within the composite. These measurements are conducted in a temperature range between 100 K and 340 K of both the reference powders and the composite. The magnetization values in the figure are reported per unit mass, and by rescaling the reference magnetization curve to match that of the composite, it is possible to determine the actual concentration of magnetic powders within the composite and calculate the mass of the active material. The measurements indicate a very similar composition for the two samples: 85% and 87% for the HEA-Ga13 and HEA-Ga11 samples, respectively.

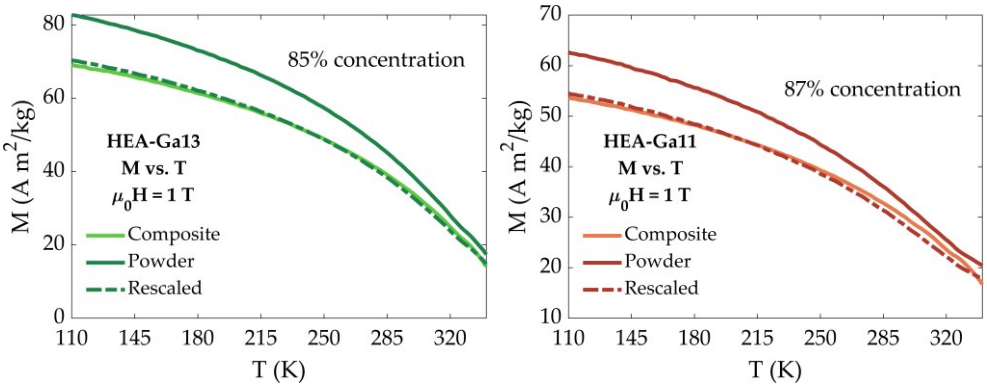

***Figure 6-48**: Isofield curves per unit mass at constant magnetic field $\mu_0 H$ = 1T over the temperature of HEA-Ga13 (left) and HEA-Ga11 (right) samples. The magnetization curves*

of the powder are reported dark coloured, the composite light coloured, and the rescaled powder curves dashed dark coloured.

For the TM tests on the HEA samples, it was decided to use two rotors mounted on the same shaft. This approach offers several advantages: first, increasing the amount of active material enhances the signal strength, allowing for more accurate mechanical power measurements. Second, using tandem rotors helps achieve a more constant angular velocity during measurements, even under lower loads. All mechanical power measurements reported in this section will be normalized to the total effective mass of the magnetic material.

Figure 6-49 depicts the relationship between mechanical power output and angular speed for the three materials, measured at different values of T_{hot} , while maintaining the cold reservoir temperature constant at 297 K. In general, there is a clear trend showing that as the temperature of the hot source increases, the power output also rises. This increase is due to the expansion of the cycle area, which improves energy conversion efficiency. However, this trend is dependent on the rotor's rotational speed.

At higher external loads, the rotor's speed is relatively low, which limits the achievable power output. As the external load decreases, the rotor's speed increases, leading to a rise in power output until it reaches a peak. Beyond this optimal point, further increases in rotational speed may cause the power output to level off or even decrease.

The observed drop in power output at high speeds can be explained by a reduction in heat exchange during the thermomagnetic cycle. This reduces the cycle area, directly affecting power output. Additionally, when the average cycle temperature exceeds the Curie temperature of the thermomagnetic material, the decrease in the magnetization gradient with respect to temperature ($\partial M/\partial T$) results in a lower net torque on the rotor, which further reduces power output.

Figure 6-50 shows the peak values of the mechanical power curves displayed in Figure 6-49. A comparison of the two samples reveals that the HEA-Ga13 sample generates approximately twice the mechanical power per unit mass compared to the HEA-Ga11 sample.

By examining the peaks of the mechanical power curves, it is possible to observe that the values obtained for the HEA samples deviate significantly from those of the Heusler samples discussed in Section 6.1.2.

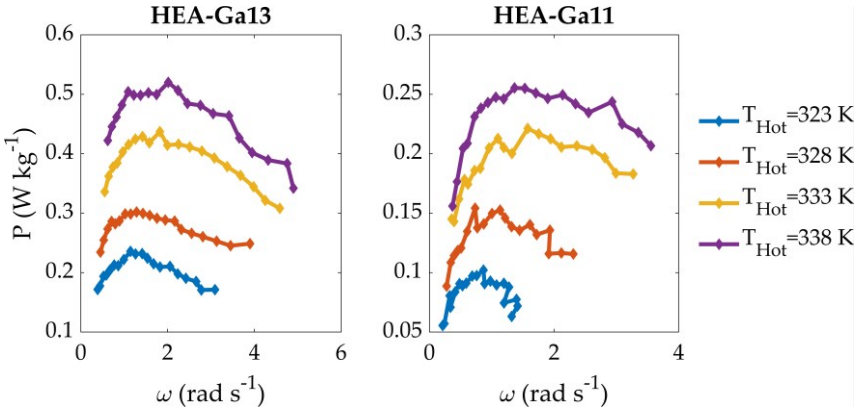

***Figure 6-49**: Mechanical power output of the TM tester as a function of angular speed of the shaft, achieved by adjusting the temperature of the warm source T_{hot} and the external resistive load, using rings made of HEA-Ga13 (left) and HEA-Ga11 (right). Each data point represents the average of measurements taken during both increasing and decreasing load sweeps.*

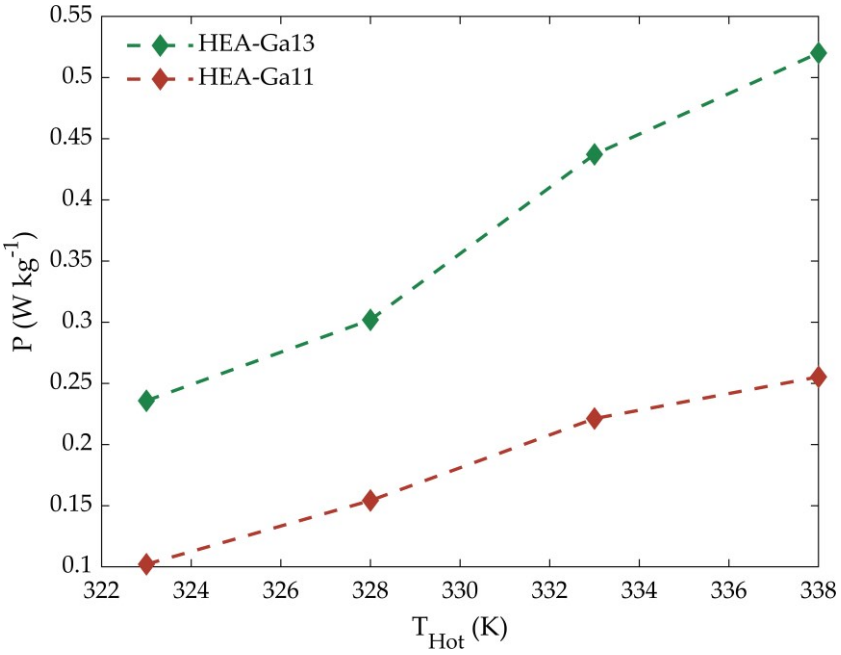

***Figure 6-50**: Maximum mechanical power output as a function of the warm reservoir temperature for rings made of HEA-Ga13 (green) and HEA-Ga11 (red). The dashed lines are provided as visual aids.*

This is also the case when comparing the HEA-Ga13 and TM-Sn samples, which, based on initial characterizations, exhibit similar magnetic properties such as Curie temperature and magnetization values. Despite this, the peak power per unit mass of the TM-Sn sample (approximately 2.2 W/kg) exceeds that of the HEA-Ga13 sample (approximately 0.5 W/kg) by more than four times.

The explanation for this discrepancy can be seen in Figure 6-51, which presents a magnified comparison of the isofield curves of the powder of the two samples as a function of temperature. The HEA-Ga13 sample shows a less steep transition compared to the TM-Sn sample, resulting in a smaller ΔM starting from 285 K. Moreover, near T_{hot} = 338 K (the temperature of the hot thermal source, corresponding to the maximum mechanical power peaks for both samples), the magnetization difference between the Heusler and HEA samples is about 9 A m^2 kg^{-1}.

One possibility that will be explored in future work to increase the sharpness of the magnetic transition in the HEA sample powders is to perform heat treatments on the powders after milling.

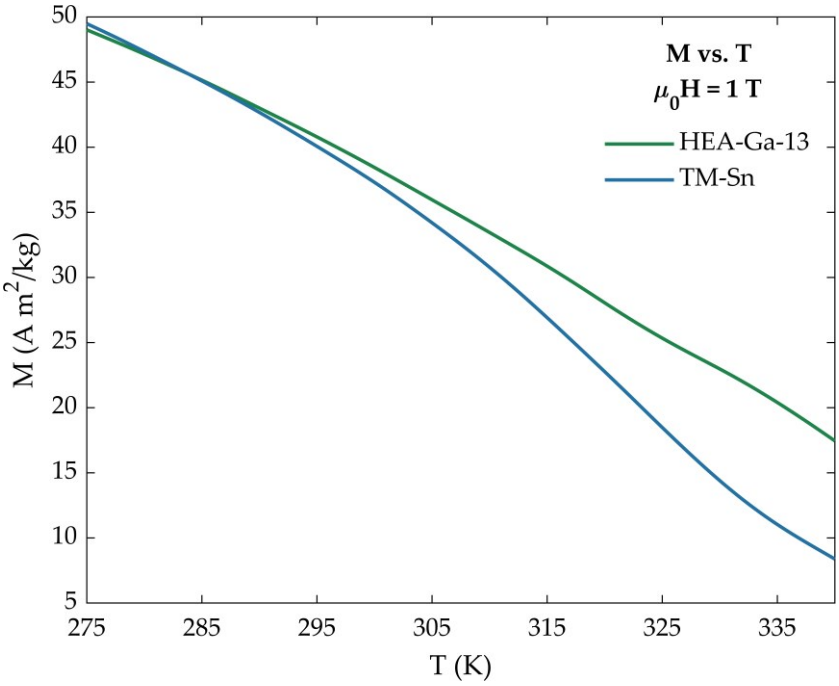

***Figure 6-51**: Magnified view between 275 K and 335 K of the isofield curves as a function of temperature for the HEA-Ga13 (green) and TM-Sn (blue) samples.*

In order to estimate the temperature difference established on the rotors, the maximum work produced per unit mass is calculated, similarly to what was done in Section 6.1.2, using the experimental data summarized in Figure 6-50. The magnetic work values for the HEA-Ga13 and HEA-Ga11 samples at T_{hot}=338 are 1.6 J/kg and 1.2 J/kg, respectively. The estimation of the temperature difference on the rotor is performed by calculating the magnetic work produced in an ideal TM cycle, setting different values for T_{Cold}^{TM} and T_{Hot}^{TM} as integration limits until the resulting magnetic work curve as a function of T_m shows peaks as close as possible to those derived from experimental data. This occurs for ΔT = 3.5K. The result of the calculation is shown in Figure 6-52.

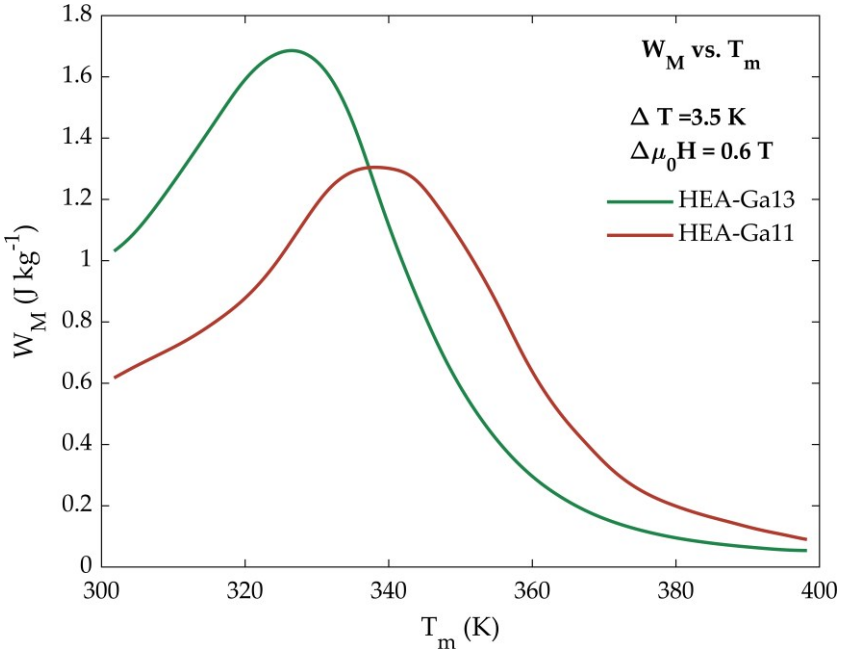

***Figure 6-52**: FoM as a function of the mean cycle temperature T_m for HEA-Ga13 (green) and HEA-Ga11 (red), with the temperature difference between the cold and warm sources held constant at 4 K. The FoM is computed using equation 3.15, based on the surfaces M(T,H) data presented in Figure 6-44.*

Finally, a comparison of the magnetic work produced in an ideal TM cycle calculated from experimental data of all the TM materials characterized in this thesis and compared to the Gd benchmark is presented both considering the maximum temperature span (Fig. 6-53), as well as considering different limited ΔT values (Fig. 6-54)

From both comparisons, it is observed that only within the lower end of the temperature range for TM applications (i.e. up to 310 K) Gd exhibits magnetic work values higher than the other materials evaluated in this thesis, except for TM-CuGa.

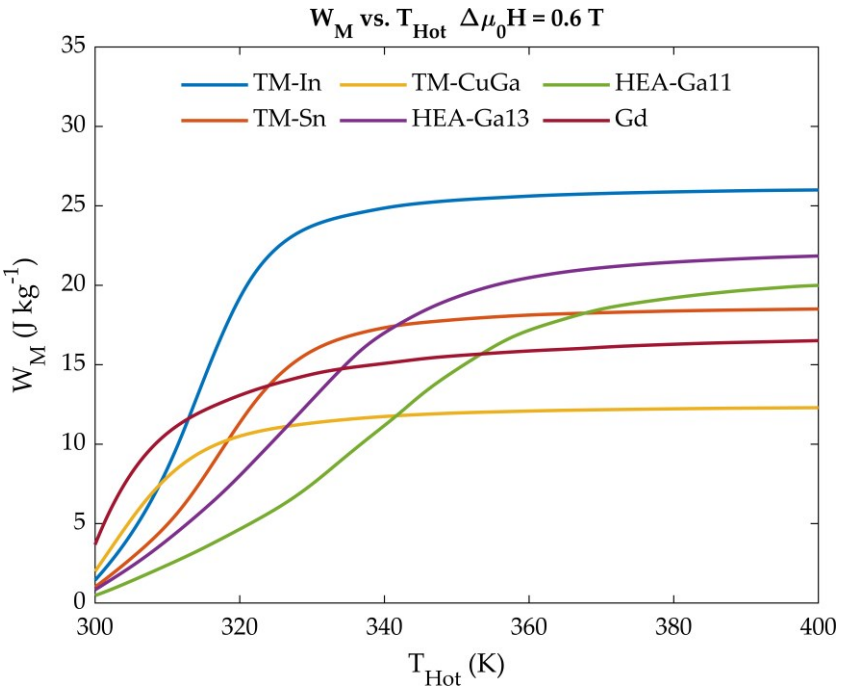

***Figure 6-53**: Comparison of FoM generated by an ideal TM cycle utilizing TM-In (blue), TM-Sn (orange), TM-CuGa (yellow), HEA-Ga13 (purple), HEA-Ga11 (green) and Gd (magenta) as a function of the hot cycle temperature T_{Hot}. The cold temperature is held constant at 297 K, along with a magnetic field of 0.6 T.*

In the condition where the materials fully thermalize with the heat sources within a cycle (Fig. 6-53), the magnetic work increases with T_{hot} and eventually stabilizes above a certain temperature that is characteristic of each material. NiMnIn emerges as the most performant material among those examined, and the two HEAs surpass the performance of NiMnSn when the hot source is at 344 K (HEA-Ga13) and 352 K (HEA-Ga11).

The comparison of the magnetic work as a function of limited temperature span provides valuable insights on how the efficiency of TM conversion changes as a function of the heat exchange or of the cycle duration: for instance, the analyses shown in Fig. 6-54 indicate that between 300 K and 330 K, the Heusler alloys studied

here are the best performing materials of the bunch, outperforming both Gd and the HEAs, while beyond 330 K, the HEAs potentially produce the higher magnetic work.

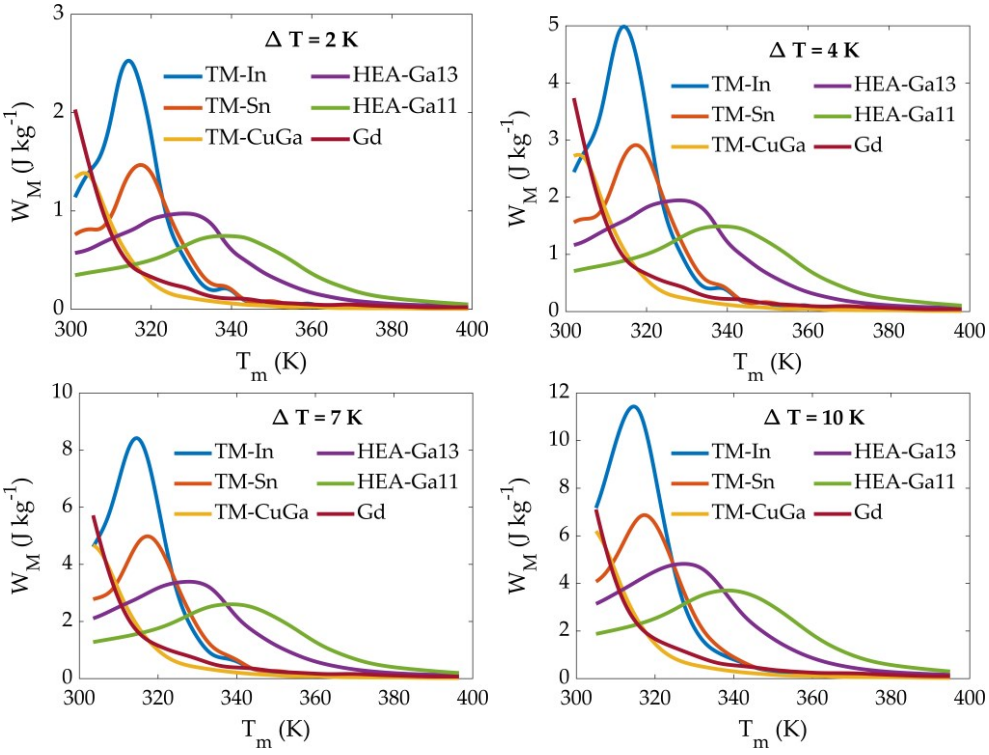

***Figure 6-54**: Comparison of FoM as a function of the mean cycle temperature T_m of TM-In (blue), TM-Sn (orange), TM-CuGa (yellow), HEA-Ga13 (purple), HEA-Ga11 (green) and Gd (magenta), at different values of temperature difference between T_{hot}^{TM} and T_{cold}^{TM}. The analysis considering a magnetic field of 0.6 T.*

These last results further underscore a very interesting finding of this study, namely that TM conversion is highly sensitive to the material properties at a given temperature span, a feature that cannot be unambiguously identified by the intrinsic properties but crucially depend on the extrinsic parameters given by the operational conditions, such as efficiency of heat exchange and temperatures of the heat sources provided by the given application. Therefore, the choice of the most suitable material is ultimately driven by such conditions.

7 Conclusions and Perspectives

This thesis explored the synthesis and application of thermomagnetic (TM) materials, focusing on NiMn-based Heusler compounds and High Entropy Alloys (HEAs) for low-temperature waste heat recovery. The findings span various domains, from the magnetic properties of the synthesized alloys to their direct application in energy recovery systems.

Initially, the study leveraged the fine-tuning potential of NiMn-based Heusler alloys to optimize critical temperatures, investigating three specific tuning methods: varying the Ni/Mn ratio, substituting Mn with Fe, and introducing Pb while preserving the primary alloy composition. For each method, a distinct set of NiMnSn-based samples was synthesized and characterized, given the alloy's non-critical nature, cost-effectiveness, and promise for TM and MC applications.

The characterization of these sets produced several key results. For example, the study of the $Ni_{50-x}Mn_{34+x}Sn_{16}$ series (Secttion 6.1.1.2) led to identifying the critical Mn concentration for peak magnetization in these alloys. The $Ni_{48}Mn_{36-x}Sn_{16}Fe_x$ series revealed a method to increase T_C in the alloy, while the $(Ni_{50}Mn_{35}Sn_{15})_{100-x}Pb_x$ series enabled crystal cell expansion and minimized magnetization loss following a Tc adjustment toward lower temperatures. Collectively, these sets enabled the fine-tuning of T_C across a broad range, facilitating composition optimization for specific applications. This work thus demonstrates how compositional tuning can precisely adjust the temperature response range in NiMnSn Heusler alloys, reinforcing their suitability for TM and MC applications.

Subsequent analysis evaluated the potential of three representative NiMn-based Heusler alloys ($Ni_{48}Mn_{36}Sn_{16}$, $Ni_{48}Mn_{36}In_{16}$, and $Ni_{50}Mn_{19}Cu_6Ga_{25}$) for TM waste heat harvesting in the 300–340 K range (Section 6.1.2). The thermomagnetic performance of these alloys was analyzed by calculating the magnetic work of ideal thermomagnetic cycles, using magnetization data as a function of temperature and applied magnetic field. Further evaluation employed an in situ thermomagnetic motor prototype, specifically designed for testing TM materials. Mechanical output from rotors made of the three alloys was measured by varying the temperature of the hot source and adjusting the external resistive load.

The results, normalized by the mass or volume of the active magnetic material, indicated an electric power output exceeding 2.5 W/kg or 20 mW/cm³. Notably, this estimated electric power greatly surpasses values reported in similar studies, underscoring both the potential of the TM motor prototype as an effective testing platform for TMG designs and the promise of NiMn-based second-order Heusler compounds for low-grade heat energy harvesting applications.

Comparisons between the magnetic work calculations for an ideal TM cycle, based on magnetic characterization data, and the power curves measured with the TM motor, as well as measurements from rotors of varying thicknesses, highlight that the limits of power output on a TM device arise from the position of the Curie temperature with respect to the available hot and cold reservoirs, and from heat exchange at the interface between the rotor and surrounding heat-transfer fluid. The possibility to finely tune the critical temperature of the TM material is of paramount importance for achieving maximum energy output in a limited temperature span. Furthermore, improving the heat exchange, such as by increasing the surface-to-volume ratio of the active rotor, is essential to enhance both the power and efficiency of TM generators.

Subsequently, 3D-printed AM rotors based on NiMnSn and NiMnIn with varying thicknesses were fabricated to test their TM properties (Section 6.1.3). The composite filament production method employed is simple yet effective, enabling a uniform dispersion of magnetic powders within a polymer matrix suitable for 3D printing. The direct printing of these composites allowed for the fabrication of rotors with different thicknesses, facilitating the assessment of TM performance as a function of the surface-to-volume ratio. Comparison of mechanical power curves among AM rotors of different thicknesses reveals that an increase in the rotor surface-to-volume ratio corresponds to higher power peaks.

Additionally, the power peak curves from 3D-printed rotors, in contrast to those of hand-crafted rotors, exhibit a sharp peak near the transition temperature of the alloy used, showing a temperature dependency of the hot source more closely aligned with simulated trends. Results from the 3D-printed AM composites underscore a promising relationship between rotor geometry and TM performance. While the efficiency of these results remains below that achieved with MM rotors, future research will aim to develop methods to increase and homogenize the concentration of active material within the composite and to experiment with new geometries to optimize the surface-to-volume ratio.

Finally, two new HEA alloys with compositions $Fe_{26}Ni_{27}Ga_{14}Mn_{24}Si_9$ and $Fe_{26}Ni_{27}Ga_{12}Mn_{25}Si_{10}$ were synthesized (Section 6.2). Magnetic characterizations identified two second-order magnetic transitions near room temperature, making these alloys interesting for potential MC and TM applications. For this purpose, both the magnetic entropy changes and magnetic works generated in an ideal TM cycle were calculated. The ΔS values are comparable to the highest reported values for rare-earth-free HEAs across the Curie transition. The calculated W_m values are similar to those obtained for NiMn-based Heuslers. Characterizations performed with the TM device show, for the first time, that the synthesized HEAs are promising

candidates for waste energy recovery, adding to the interest in this novel class of functional materials.

The thermomagnetic studies reported in this thesis address a question frequently highlighted in the study of TM materials for energy harvesting of low-grade heat: whether second-order magnetic materials are suitable for this application, given their lower steepness of the magnetic transition compared to first-order counterparts. Considering the results obtained, the studied second-order Heusler and HEAs prove to be highly competitive for this application, outperforming Gd in the most relevant temperature range for TM applications. Furthermore, they enable thermomagnetic conversion even when the actual thermal gradients are significantly lower than the temperature difference of the thermal sources, a situation in which the cyclic response of first-order materials might be severely degraded by the presence of transformation hysteresis.

In conclusion, the experimental work presented in this thesis offers novel and effective solutions for the emerging field of low-grade waste heat conversion, the most abundant type of waste heat, via magnetic effects. This field within materials science is currently under active exploration. These solutions encompass the study and production of functional magnetic materials, traditionally examined primarily for magnetic refrigeration applications, modified here to enable their use in waste heat recovery. Furthermore, TM properties were evaluated under operational conditions, allowing for the direct assessment of the most critical aspects affecting the performance of conversion and thereby narrowing the gap between the functional study of magnetic alloys and their application. This approach provides a straightforward and effective method for future assessments of other magnetic materials.

8 Appendix

8.1 Data acquisition and calibration of the TM tester

The mechanical power, angular velocity, and torque of the thermomagnetic motor were evaluated by measuring the voltage and current output from a custom-designed two-phase electric generator attached to the rotor shaft. Voltage was measured directly at the resistive load, while current was determined by measuring the potential difference across a 100 Ω shunt resistor.

In permanent magnet electric motors or generators, the open-circuit back electromotive force (back-emf), which in this case exhibits a near-sinusoidal waveform, reaches a peak voltage V_{peak} that is directly proportional to the angular speed (ω). This proportionality constant, referred to as the motor speed constant (K_v), is defined in Equation 1.

$$K_v = \frac{\omega}{V_{peak}} \qquad (8.1)$$

Equation 8.11 can be used to estimate the angular speed based on the peak voltage, provided the motor speed constant is known. However, to determine ω at each recorded instant, two windings (labeled A and B) with a 90-degree electrical phase shift are required. Each winding is modeled as an ideal sinusoidal voltage generator that produces a time-dependent signal $V_{idealA,B}(t)$ in series with a resistor equal to the internal resistance of the winding (R_{iA}, R_{iB}). When a load is applied to circuits A and B, the back-emf of each winding as a function of time can be described by Equations 8.2 and 8.3.

$$V_{idealA}(t) = V_{loadA}(t) + R_{iA} \cdot I_{loadA}(t) \qquad (8.2)$$

$$V_{idealB}(t) = V_{loadB}(t) + R_{iB} \cdot I_{loadB}(t) \qquad (8.3)$$

The back-emf is derived from the load voltage corrected for resistive losses in the windings $R_{iA,B} \cdot I_{loadA,B}(t)$. Using Equation 8.1 and assuming a sinusoidal voltage output with angular frequency ω and a purely resistive load, the back-emf of each winding over time can also be represented as in Equations 8.4 and 8.5.

$$V_{idealA}(t) = V_{peakA} \sin(\omega t + \varphi) = \frac{\omega}{K_{vA}} \sin(\omega t + \varphi) \qquad (8.4)$$

$$V_{idealB}(t) = V_{peakB} \cos(\omega t + \varphi) = \frac{\omega}{K_{vB}} \cos(\omega t + \varphi) \qquad (8.5)$$

The angular speed ω(t) at any given instant t can be determined by calculating the quadrature sum of $K_{vA}V_{idealA}(t)$ and $K_{vB}V_{idealB}(t)$, as shown in Equation 8.6.

$$\omega(t) = \sqrt{{K_{vA}}^2 \cdot V_{idealA}^2(t) + {K_{vB}}^2 \cdot V_{idealB}^2(t)}$$
$$= \sqrt{{K_{vA}}^2 \left(\frac{\omega}{K_{vA}}\sin(\omega t + \varphi)\right)^2 + {K_{vB}}^2 \left(\frac{\omega}{K_{vB}}\sin(\omega t + \varphi)\right)^2} =$$
$$= \sqrt{\omega^2 \sin^2(\omega t + \varphi) + \omega^2 \cos^2(\omega t + \varphi)} =$$
$$= \omega\sqrt{\sin^2(\omega t + \varphi) + \cos^2(\omega t + \varphi)} = \omega \qquad (8.6)$$

By substituting Equations 8.2 and 8.3 into Equation 8.6, the angular speed of the shaft can be calculated from the output voltage ($V_{load}(t)$) and current ($I_{load}(t)$) when a load is applied to the generator, as indicated in Equation 8.7.

$$\omega(t) = \sqrt{{K_{vA}}^2 \cdot \left(V_{loadA}(t) + R_{iA} \cdot I_{loadA}(t)\right)^2 + {K_{vB}}^2 \cdot \left(V_{loadB}(t) + R_{iB} \cdot I_{loadB}(t)\right)^2} \qquad (8.7)$$

Each winding has unique motor speed constants (K_{vA} and K_{vB}) and internal resistance values (R_{iA} and R_{iB}) to account for minor discrepancies from manufacturing tolerances in the generator stator. The series resistance of each winding was measured with a digital multimeter, and a calibration process was conducted to accurately determine the speed constants. During calibration, voltage and current readings were recorded while applying a known torque to the generator shaft under various loads. A one-term Fourier series fit was used to obtain both the rotational speed and the voltage amplitude, accounting for internal resistance. With these ω and voltage values, a linear fit was applied to obtain K_v for each winding.

In a similar manner to Equation 8.1, the relationship between peak armature current (I_{peak}) and the torque (τ) generated by the motor or generator is expressed in Equation 8.8,

$$K_\tau = \frac{\tau}{I_{peak}} \qquad (8.8)$$

where K_τ represents the motor torque constant. To minimize detent torque, a 3D-printed ironless stator core was used to support the windings. In a permanent magnet motor or generator with an ironless core, the motor speed constant is the reciprocal of the torque constant when both are expressed in SI units ($K_\tau = \frac{1}{K_v}$)[175]. Thus, the motor torque can be determined as shown in Equation 8.9.

$$\tau = \frac{I}{K_v} \qquad (8.9)$$

This equation enables estimation of the motor torque using the same approach as in Equation 8.7 by measuring the winding current and knowing each winding's speed constant Kv, as detailed in Equation 8.10.

$$\tau(\mathrm{t}) = \sqrt{\frac{I^2{}_{loadA}(t)}{{K_{vA}}^2} + \frac{I^2{}_{loadB}(t)}{{K_{vB}}^2}} \qquad (8.10)$$

During calibration, the difference between the applied known torque and the torque derived from the armature current was calculated to determine the frictional torque from the shaft-supporting ball bearings. Frictional torque was estimated to be approximately 2×10^{-5} Nm, with minimal dependence on ω. If 1 mW of mechanical power is applied to the shaft at a speed of 5 rad s^{-1}, the frictional losses would account for around 10% of the input mechanical power.

The torque data obtained from material testing were corrected for frictional torque to determine the total torque produced by the thermomagnetic motor.

8.2 Mass losses during synthesis

Sample	I melt [%]	II melt [%]	III melt [%]
TM-Sn	0.20	0.42	0.76
TM-In	0.23	0.31	0.45
TM-CuGa	0.90	2.22	3.30
Ni/Mn-x0	0.21	0.52	0.84
Ni/Mn-x2	0.20	0.42	0.76
Ni/Mn-x4	0.17	0.43	0.81
Ni/Mn-x6	0.27	0.33	0.35
Ni/Mn-x8	0.07	0.27	0.34
Sub-Fe0	0.27	0.47	0.59
Sub-Fe2	0.11	0.33	0.49
Sub-Fe4	0.23	0.39	0.82
Sub-Fe6	0.44	0.57	0.63
Sub-Fe8	0.24	0.60	1.02
Sub-Fe10	0.07	0.40	0.96
Add-Pb0	0.30	0.76	0.92
Add-Pb1	0.63	1.58	2.46
Add-Pb2	1.15	2.41	3.75
Add-Pb3	1.16	3.02	4.33
Add-Pb4	1.19	3.4	6.47
HEA-Ga13	0.14	0.58	1.16
HEA-Ga11	0.76	1.51	1.64

***Table 12**: List of samples synthesized and characterized in this thesis and their mass losses. The first column presents the names of the sample, the second, third and fourth columns contain the mass losses of the first, second and third melt respectively.*

8.3 Magnetic characterization methods

In this paragraph, the plots of the temperature-dependent derivatives of magnetic susceptibility and magnetization for a sample, Add-Pb3, are presented as an example. An analogous procedure to that applied in figure 8-1 has been conducted for all samples produced and shown in this thesis. It is through the analysis of these derivatives that key magnetic parameters for material characterization (T_C, $\partial M/\partial T$, ΔM_{4K}) have been obtained.

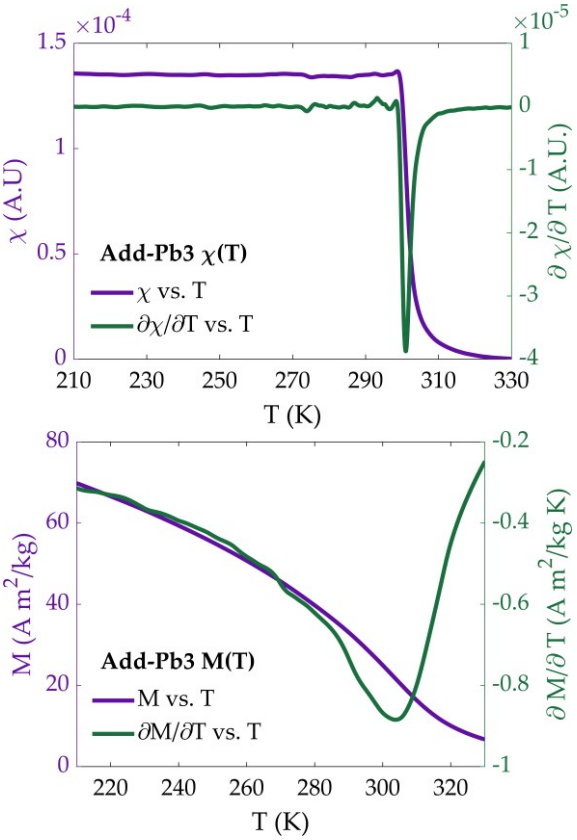

***Figure 8-1**: (a) Comparison between the magnetic susceptibility curve under an applied magnetic field of 1 mT (purple) and its first derivative with respect to temperature (green). The derivative analysis is used to identify TC. (b) Comparison between the isofield magnetization curve at 1 T (purple) and its first derivative with respect to temperature (green). This measurement is used to evaluate dM/dT at T=T_C and to calculate M_{4K}. Both plots refer to the sample Add-Pb3, provided as an example.*

8.4 W_m of ideal TM cycle varying H_{max} and ΔT

This section presents the analyses conducted on the TM-Sn sample, taken as an example, of the magnetic work while varying the magnetic field value (Fig. 8-2 (a)) and the temperature span imposed on the material within the TM cycle (Fig. 8-2 (b)).

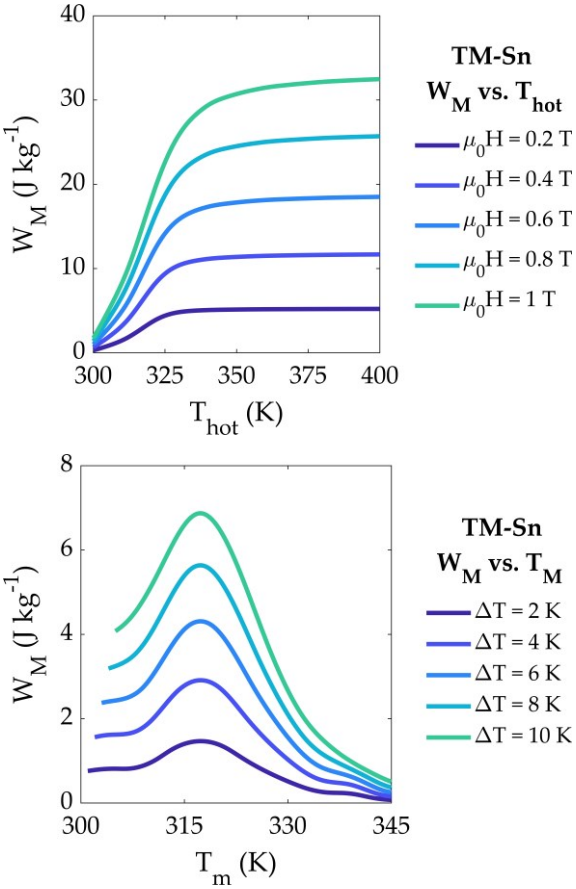

***Figure 8-2**: (a) Comparison of FoM generated by an ideal TM cycle utilizing TM-Sn as a function of the hot cycle temperature T_{hot} at different magnetic field values. (b) Comparison of FoM as a function of the mean cycle temperature T_m of TM-Sn, at different values of temperature difference between T_{hot}^{TM} and T_{cold}^{TM}. The analysis considering a magnetic field of 0.6 T.*

8.5 TM tests of different rotor configurations

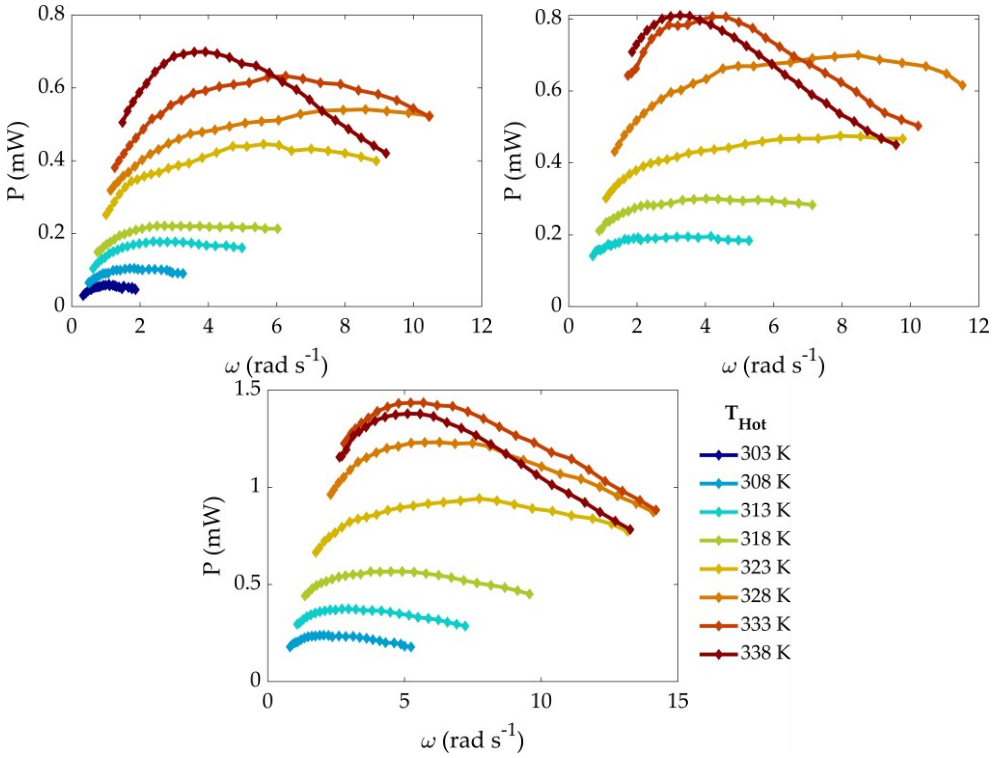

***Figure 8-3**: Mechanical power output of the TM tester as a function of angular speed of the shaft, achieved by adjusting the temperature of the warm source T_{hot} and the external resistive load, using rings made of TM-In-based 1 mm thick rotor (a), 1.5 mm thick (b) and two 1mm thick rotos both connected to the shaft. Each data point represents the average of measurements taken during both increasing and decreasing load sweeps.*

8.6 Electric power generation and efficiency simulations

By understanding the relationship between mechanical power output and angular speed of the thermomagnetic motor, it becomes feasible to model the electric power output and conversion efficiency attainable when the motor is coupled with an electric generator characterized by a known speed constant and internal resistance.

For a two-phase electric generator operating under the assumptions of negligible friction, constant rotational speed, and identical speed constant K_v and internal resistance R_i for both windings, the total power loss from Joule heating within the generator's armatures can be expressed as:

$$P_{loss} = I_{peak}^2 \cdot R_i = \tau^2 \cdot K_v^2 \cdot R_i = \frac{P_{in}^2}{\omega^2} \cdot K_v^2 \cdot R_i \qquad (8.11)$$

where P_{in} represents the mechanical power input, and ω denotes the angular speed.

The overall conversion efficiency η, describing the conversion from mechanical to electrical energy, can then be defined as:

$$\eta = 1 - \frac{P_{loss}}{P_{in}} \qquad (8.12)$$

The generator efficiency η and the net electrical power delivered to the load P_{load} can therefore be evaluated in relation to the mechanical power input, angular speed, and specific construction parameters of the generator:

$$\eta = 1 - \frac{P_{in}}{\omega^2} \cdot K_v^2 \cdot R_i \qquad (13)$$

$$P_{load} = P_{in} \cdot \eta = P_{in}\left(1 - \frac{P_{in}}{\omega^2} \cdot \mathrm{K_v^2} \cdot \mathrm{R_i}\right) \qquad (14)$$

Assuming plausible values of the speed constant K_v = 2 rads^{-1}V^{-1} and winding internal resistance R_i = 1300 Ω for a miniature electric generator optimized for low-rpm operation, we can estimate the electric power output of a thermomagnetic generator using the materials tested in this work. The two-rotor NiMnIn-based configuration of the thermomagnetic motor is expected to give a maximum electric power output of 1.2 mW at an angular speed of 7.3 rads^{-1}, corresponding to a mechanical-to-electric power conversion efficiency of 86%. If we normalize this value to the mass ore the volume of utilized active magnetic material, we obtained an output electric power of 2.6 W/kg or 20.4 mW/cm^3.

8.7 XRD analysis of HEAs

Figure 8-2 presents the X-ray analyses conducted on the HEA-Ga13 (a) and HEA-Ga11 (b) samples.

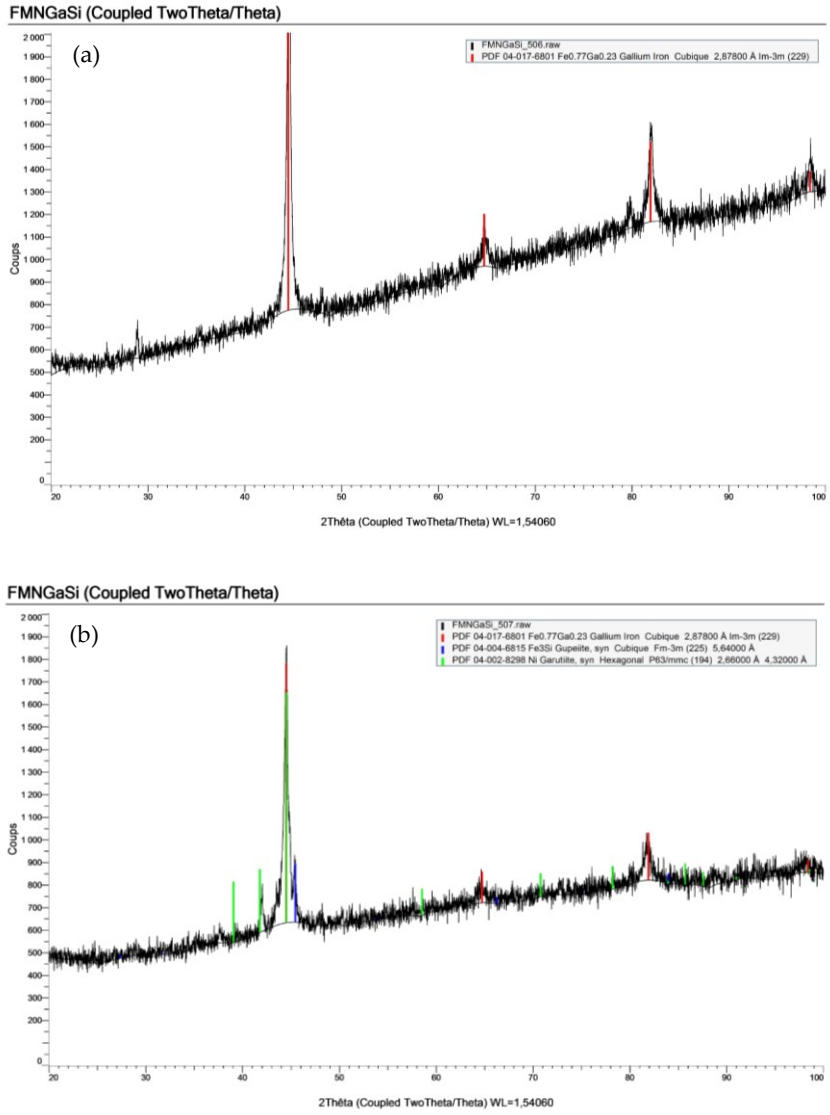

***Figure 8-4**: diffraction patterns of HEA-Ga13 (a) and HEA-Ga11 (b).*

9 List of pubblications and presentations

Papers

- “In-operando test of tunable Heusler alloys for thermomagnetic harvesting of low-grade waste heat.” F. Cugini, L. Gallo, G. Garulli, D. Olivieri, S. Fabbrici, G. Trevisi, F. Albertini, M. Solzi. [Submitted]
- “Ni-Mn-Sn Heusler alloys for thermomagnetic applications” L. Gallo, F. Cugini, S. Fabbrici, M. Solzi, F. Albertini. [in preparation]
- “Fe-Ni-Ga-Mn-Si magnetic High Entropy Alloys for application in the harvesting of low grade waste heat” L. Gallo, F. Cugini, G. Garulli, S. Fabbrici, G. Trevisi, M. Solzi, F. Albertini. [in preparation]
- “Additive manufacturing of NiMn-based Heusler alloys for thermomagnetic applications” L. Gallo, S. Fabbrici, F. Cugini, G. Garulli, M. Solzi, G. Trevisi, J. Y. Law, V. Franco , F. Albertini. [in preparation]

International conferences

- Oral presentation at IEEE Advanced In Magnetism (2023)
- Oral presentation at Joint European Magnetic Symposia (2023)

10 Bibliography

[1] J. L. Holechek, H. M. E. Geli, M. N. Sawalhah, and R. Valdez, "A Global Assessment: Can Renewable Energy Replace Fossil Fuels by 2050?," *Sustainability (Switzerland)*, vol. 14, no. 8, Apr. 2022, doi: 10.3390/su14084792.

[2] G. tho Pesch, A. K. Einarsdóttir, K. J. Dillman, and J. Heinonen, "Energy Consumption and Human Well-Being: A Systematic Review," Sep. 01, 2023, *Multidisciplinary Digital Publishing Institute (MDPI)*. doi: 10.3390/en16186494.

[3] D. I. Stern, "The role of energy in economic growth," *Ann N Y Acad Sci*, vol. 1219, no. 1, pp. 26–51, 2011, doi: 10.1111/j.1749-6632.2010.05921.x.

[4] B. K. Sovacool and M. A. Brown, "Competing dimensions of energy security: An international perspective," *Annu Rev Environ Resour*, vol. 35, pp. 77–108, Nov. 2010, doi: 10.1146/annurev-environ-042509-143035.

[5] R. J. Heffron and D. McCauley, "What is the 'Just Transition'?," *Geoforum*, vol. 88, pp. 74–77, Jan. 2018, doi: 10.1016/j.geoforum.2017.11.016.

[6] REN21. 2020, "Renewables 2020 Global Status Report," *Paris: REN21 Secretariat*, 2020.

[7] United Nations General assembly, "Transforming our world: the 2030 Agenda for Sustainable Development," 2015.

[8] International Renewable Energy Agency, *Innovation landscape for a renewable-power future: solutions to integrate variable renewables*. 2019. [Online]. Available: www.irena.org/publications

[9] C. Forman, I. K. Muritala, R. Pardemann, and B. Meyer, "Estimating the global waste heat potential," May 01, 2016, *Elsevier Ltd*. doi: 10.1016/j.rser.2015.12.192.

[10] U.S: Energy Information Administration, "International Energy Outlook 2023," 2023.

[11] Q. Bian, "Waste heat: the dominating root cause of current global warming," *Environmental Systems Research*, vol. 9, no. 1, Dec. 2020, doi: 10.1186/s40068-020-00169-2.

[12] R. A. Kishore and S. Priya, "A Review on low-grade thermal energy harvesting: Materials, methods and devices," Aug. 14, 2018, *MDPI AG*. doi: 10.3390/ma11081433.

[13] International Energy Agency, "The Future of Cooling Opportunities for energy-efficient air conditioning Together Secure Sustainable," 2018. [Online]. Available: www.iea.org/t&c/

[14] R. Ahmed Memon, D. Y. Leung, and L. Chunho, "A review on the generation, determination and mitigation of Urban Heat Island," *Journal of Environmental Sciences*, vol. 20, pp. 120–128, 2008, doi: 10.1016/S1001-0742(08)60019-4.

[15] V. K. Pecharsky and K. A. Gschneidner, "Giant Magnetocaloric Effect in Gd 5 Si 2 Ge 2," *Phys Rev Lett*, vol. 78(23), pp. 4494–4497, 1997, doi: 10.1103/PhysRevLett.78.4494.

[16] A. Kitanovski, "Energy Applications of Magnetocaloric Materials," *Adv Energy Mater*, vol. 10, no. 10, Mar. 2020, doi: 10.1002/aenm.201903741.

[17] D. Dzekan, A. Waske, K. Nielsch, and S. Fähler, "Efficient and affordable thermomagnetic materials for harvesting low grade waste heat," *APL Mater*, vol. 9, no. 1, Jan. 2021, doi: 10.1063/5.0033970.

[18] T. Gottschall *et al.*, "Magnetocaloric effect of gadolinium in high magnetic fields," *Phys Rev B*, vol. 99, no. 13, Apr. 2019, doi: 10.1103/PhysRevB.99.134429.

[19] F. Cugini *et al.*, "In-operando test of tunable Heusler alloys for thermomagnetic harvesting of low-grade waste heat."

[20] A. Waske, M. E. Gruner, T. Gottschall, and O. Gutfleisch, "Magnetocaloric materials for refrigeration near room temperature," Apr. 01, 2018, *Cambridge University Press*. doi: 10.1557/mrs.2018.69.

[21] T. Gottschall *et al.*, "Making a Cool Choice: The Materials Library of Magnetic Refrigeration," *Adv Energy Mater*, vol. 9, no. 34, Sep. 2019, doi: 10.1002/aenm.201901322.

[22] P. Weiss and A. Piccard, "Le phénomène magnétocalorique," *Journal de Physique Théorique et Appliquée*, vol. 7, no. 1, pp. 103–109, 1917, doi: 10.1051/jphystap:019170070010300.

[23] J. Lyubina, "Magnetocaloric materials for energy efficient cooling," Jan. 05, 2017, *Institute of Physics Publishing*. doi: 10.1088/1361-6463/50/5/053002.

[24] V. Franco, J. S. Blázquez, B. Ingale, and A. Conde, "The magnetocaloric effect and magnetic refrigeration near room temperature: Materials and models," *Annu Rev Mater Res*, vol. 42, pp. 305–342, Aug. 2012, doi: 10.1146/annurev-matsci-062910-100356.

[25] V. K. Pecharsky and K. A. Gschneidner, "Magnetocaloric effect and magnetic refrigeration," *J Magn Magn Mater*, vol. 200, pp. 44–56, 1999, doi: 10.1016/S0304-8853(99)00397-2.

[26] V. K. Pecharsky, V. K. Pecharsky, K. A. Gschneidner, K. A. Gschneidner, A. O. Pecharsky, and A. M. Tishin, "Thermodynamics of the magnetocaloric effect," *Phys Rev B Condens Matter Mater Phys*, vol. 64, no. 14, pp. 1444061–14440613, Oct. 2001, doi: 10.1103/PhysRevB.64.144406.

[27] J. Lyubina, "Magnetocaloric materials," in *Springer Series in Materials Science*, vol. 231, Springer Verlag, 2016, ch. 4, p. 121. doi: 10.1007/978-3-319-26106-5_4.

[28] Tishin M. A. and Spichkin Y. I., "The Magnetocaloric Effect and its Applications," in *Series in Condensed Matter Physics*, 2023, ch. 2.1, p. 31.

[29] K. P. Skokov, V. V. Khovaylo, K. H. Müller, J. D. Moore, J. Liu, and O. Gutfleisch, "Magnetocaloric materials with first-order phase transition: Thermal and magnetic hysteresis in LaFe 11.8Si 1.2 and Ni 2.21Mn 0.77Ga 1.02," *J Appl Phys*, vol. 111, no. 7, Apr. 2012, doi: 10.1063/1.3670987.

[30] G. V. Brown, "Magnetic heat pumping near room temperature," *J Appl Phys*, vol. 47, no. 8, pp. 3673–3680, 1976, doi: 10.1063/1.323176.

[31] S. Y. Dan'kov, A. M. Tishin, V. K. Pecharsky, and K. A. Gschneidner, "Magnetic phase transitions and the magnetothermal properties of gadolinium," *Phys Rev B*, vol. 57, no. 6, pp. 3478–3490, 1998, doi: 10.1103/PhysRevB.57.3478.

[32] J. Lyubina *et al.*, "Magnetic field dependence of the maximum magnetic entropy change," *Phys Rev B Condens Matter Mater Phys*, vol. 83, no. 1, Jan. 2011, doi: 10.1103/PhysRevB.83.012403.

[33] J. Lyubina, O. Gutfleisch, M. D. Kuz'min, and M. Richter, "La(Fe,Si)13-based magnetic refrigerants obtained by novel processing routes," *J Magn Magn Mater*, vol. 321, no. 21, pp. 3571–3577, Nov. 2009, doi: 10.1016/j.jmmm.2008.03.063.

[34] K. P. Skokov *et al.*, "Influence of thermal hysteresis and field cycling on the magnetocaloric effect in LaFe11.6Si1.4," *J Alloys Compd*, vol. 552, pp. 310–317, Mar. 2013, doi: 10.1016/j.jallcom.2012.10.008.

[35] A. Fujita, S. Fujieda, Y. Hasegawa, and K. Fukamichi, "Itinerant-electron metamagnetic transition and large magnetocaloric effects in La(FexSi1-x)13 compounds and their hydrides," *Phys Rev B Condens Matter Mater Phys*, vol. 67, no. 10, pp. 1044161–10441612, Mar. 2003, doi: 10.1103/physrevb.67.104416.

[36] Tegus O., Brück E., Buschow K. H. J., and de Boer F. R., "Transition-metal-based magnetic refrigerants for room-temperature applications," *Letter to Nature*, vol. 415, pp. 150–152, 2002, doi: 10.1038/415150a.

[37] N. H. Dung *et al.*, "Mixed magnetism for refrigeration and energy conversion," *Adv Energy Mater*, vol. 1, no. 6, pp. 1215–1219, Nov. 2011, doi: 10.1002/aenm.201100252.

[38] N. T. Trung, Z. Q. Ou, T. J. Gortenmulder, O. Tegus, K. H. J. Buschow, and E. Brück, "Tunable thermal hysteresis in MnFe(P,Ge) compounds," *Appl Phys Lett*, vol. 94, no. 10, 2009, doi: 10.1063/1.3095597.

[39] F. Guillou, H. Yibole, N. H. Van Dijk, and E. Brück, "Effect of boron substitution on the ferromagnetic transition of MnFe0.95P2/3Si1/3," *J Alloys Compd*, vol. 632, pp. 717–722, May 2015, doi: 10.1016/j.jallcom.2015.01.308.

[40] Graf T., Felser C., and Parkin S. S. P., "T. Graf (2011)," *Progress in Solid State Chemistry*, vol. 39, pp. 1–50, 2011, doi: 10.1016/j.progsolidstchem.2011.02.001.

[41] F. X. Hu, B. G. Shen, and J. R. Sun, "Magnetic entropy change in Ni51.5Mn22.7Ga25.8 alloy," *Appl Phys Lett*, vol. 76, no. 23, pp. 3460–3462, Jun. 2000, doi: 10.1063/1.126677.

[42] M. Acet, L. Mañosa, and A. Planes, "4 - Magnetic-Field-Induced Effects in Martensitic Heusler-Based Magnetic Shape Memory Alloys," 2011, doi: 10.1016/S1567-2719(11)19004-6.

[43] L. Pareti, M. Solzi, F. Albertini, and A. Paoluzi, "Giant entropy change at the co-occurrence of structural and magnetic transitions in the Ni2.19Mn0.81Ga Heusler alloy," *European Physical Journal B*, vol. 32, no. 3, pp. 303–307, 2003, doi: 10.1140/epjb/e2003-00102-y.

[44] S. Singh *et al.*, "Large Magnetization and Reversible Magnetocaloric Effect at the Second-Order Magnetic Transition in Heusler Materials," *Advanced Materials*, vol. 28, no. 17, pp. 3321–3325, May 2016, doi: 10.1002/adma.201505571.

[45] V. Franco, J. S. Blázquez, J. J. Ipus, J. Y. Law, L. M. Moreno-Ramírez, and A. Conde, "Magnetocaloric effect: From materials research to refrigeration devices," Apr. 01, 2018, *Elsevier Ltd*. doi: 10.1016/j.pmatsci.2017.10.005.

[46] R. D. McMichael, J. J. Ritter, and R. D. Shull, "Enhanced magnetocaloric effect in Gd3Ga5-xFe xO12," *J Appl Phys*, vol. 73, no. 10, pp. 6946–6948, 1993, doi: 10.1063/1.352443.

[47] G. V. Brown, "Magnetic heat pumping near room temperature," *J Appl Phys*, vol. 47, no. 8, pp. 3673–3680, 1976, doi: 10.1063/1.323176.

[48] W. A. Steyert, "Rotating Carnot-cycle magnetic refrigerators for use near 2 K," *J Appl Phys*, vol. 49, no. 3, pp. 1227–1231, 1978, doi: 10.1063/1.325010.

[49] L. D. Kirol and M. W. Dacus, "Rotary recuperative magnetic heat pump," *Adv Cryog Eng*, 1988, doi: 10.1007/978-1-4613-9874-5_92.

[50] G. Green, J. Chafe, J. Stevens, and J. Humphrey, "A gadolinium-terbium active regenerator abstract," *Adv Cryog Eng*, vol. 35, 1990, doi: 10.1007/978-1-4613-0639-9_140.

[51] C. Zimm *et al.*, "Description and performance of a near-room temperature magnetic refrigerator," *Adv Cryog Eng*, vol. 43, 1998, doi: 10.1007/978-1-4757-9047-4_222.

[52] A. M. Rowe, "Design of an active magnetic regenerator test apparatus," AIP Publishing, Feb. 2003, pp. 995–1002. doi: 10.1063/1.1472121.

[53] C. Zimm et al., "Rotating bed magnetic apparatus," US 6,526,759 B2, 2003

[54] C. Zimm *et al.*, "Design and performance of a permanent-magnet rotary refrigerator," *International Journal of Refrigeration*, vol. 29, no. 8, pp. 1302–1306, Dec. 2006, doi: 10.1016/j.ijrefrig.2006.07.014.

[55] M. A. Richard, A. M. Rowe, and R. Chahine, "Magnetic refrigeration: Single and multimaterial active magnetic regenerator experiments," *J Appl Phys*, vol. 95, no. 4, pp. 2146–2150, Feb. 2004, doi: 10.1063/1.1643200.

[56] Kitanovski A. and Sari O., "Magnetic refrigerator and/or heat pump using magneto-caloric fluid and process for magnetic heating and/or cooling with such a refrigerator and/or heat pump," EP 1 736 718 A1, 2006

[57] C. Zimm, J. Auringer, A. Boeder, J. Chell, S. Russek, and A. Sternberg, "Design and initial performance of a magnetic refrigerator with a rotating permanent magnet," in *Second IIF-IIR International Conference on Magnetic Refrigeration at Room Temperature*, 2007.

[58] V. D. Buchelnikov, S. V. Taskaev, I. V. Bychkov, I. A. Chernets, and A. N. Denisovskiy, "The prototype of effective device for magnetic refrigeration.," in *Second IIF-IIR International Conference on Magnetic Refrigeration at Room Temperature*, 2007.

[59] S. Bour, J. L. Hamm, H. Michot, and C. Muller, "Experimental and numerical analysis of a reciprocating room temperature active magnetic regenerator," in *Third IIF-IIR International Conference on Magnetic Refrigeration at Room Temperature*, 2009.

[60] Y. Kim and S. Jeong, "Investigation on the room temperature active magnetic regenerative refrigerator with permanet magnet array," in *Third IIF-IIR International Conference on Magnetic Refrigeration at Room Temperature*, 2009.

[61] K. Engelbrecht, C. R. H. Bahl, and K. K. Nielsen, "Experimental results for a magnetic refrigerator using three different types of magnetocaloric material regenerators," *International Journal of Refrigeration*, vol. 34, no. 4, pp. 1132–1140, Jun. 2011, doi: 10.1016/j.ijrefrig.2010.11.014.

[62] Park I., Kim Y., and Jeong S., "Development of the active magnetic regenerative refrigerator for room temperature application," *Journal of the Korean Society of Superconducting and Low Temperature Engineering*, vol. 14, no. 3, 2012, doi: 10.9714/sac.2012.14.3.060.

[63] D. Eriksen *et al.*, "Design and experimental tests of a rotary active magnetic regenerator prototype," *International Journal of Refrigeration*, vol. 58, pp. 14–21, Oct. 2015, doi: 10.1016/j.ijrefrig.2015.05.004.

[64] M. A. Benedict, S. A. Sherif, D. G. Beers, and M. G. Schroeder, "Design and performance of a novel magnetocaloric heat pump," *Sci Technol Built Environ*, vol. 22, no. 5, pp. 520–526, Jul. 2016, doi: 10.1080/23744731.2016.1185889.

[65] C. Aprea, A. Greco, and A. Maiorino, "An application of the artificial neural network to optimise the energy performances of a magnetic refrigerator," *International Journal of Refrigeration*, vol. 82, pp. 238–251, Oct. 2017, doi: 10.1016/j.ijrefrig.2017.06.015.

[66] J. B. Chaudron, C. Muller, M. Hittinger, M. Risser, and S. Lionte, "Performance measurements on a large-scale magnetocaloric cooling application at room temperature," in *Refrigeration Science and Technology*, International Institute of Refrigeration, 2018, pp. 137–142. doi: 10.18462/iir.thermag.2018.0022.

[67] M. Krautz, M. Beyer, C. Jäschke, L. Schinke, A. Waske, and J. Seifert, "A magnetocaloric booster unit for energy-efficient air-conditioning," *Crystals (Basel)*, vol. 9, no. 2, 2019, doi: 10.3390/cryst9020076.

[68] B. Huang *et al.*, "Development of an experimental rotary magnetic refrigerator prototype," *International Journal of Refrigeration*, vol. 104, pp. 42–50, Aug. 2019, doi: 10.1016/j.ijrefrig.2019.04.029.

[69] K. Klinar, J. Y. Law, V. Franco, X. Moya, and A. Kitanovski, "Perspectives and Energy Applications of Magnetocaloric, Pyromagnetic, Electrocaloric, and Pyroelectric Materials," *Adv Energy Mater*, Oct. 2024, doi: 10.1002/aenm.202401739.

[70] M. Wiesheu *et al.*, "How to build the optimal magnet assembly for magnetocaloric cooling: Structural optimization with isogeometric analysis," *International Journal of Refrigeration*, vol. 152, pp. 62–73, Aug. 2023, doi: 10.1016/j.ijrefrig.2023.04.014.

[71] R. Almeida *et al.*, "Rotating magnetocaloric effect in polycrystals—harnessing the demagnetizing effect," *JPhys Energy*, vol. 6, no. 1, Jan. 2024, doi: 10.1088/2515-7655/ad1c61.

[72] D. Benke *et al.*, "Magnetic Refrigeration with Recycled Permanent Magnets and Free Rare-Earth Magnetocaloric La–Fe–Si," *Energy Technology*, vol. 8, no. 7, Jul. 2020, doi: 10.1002/ente.201901025.

[73] L. Schäfer *et al.*, "Design and Qualification of Pr–Fe–Cu–B Alloys for the Additive Manufacturing of Permanent Magnets," *Adv Funct Mater*, vol. 31, no. 33, Aug. 2021, doi: 10.1002/adfm.202102148.

[74] S. Nosan, U. Tomc, J. Klemenc, and A. Kitanovski, "Design and comparison of electro-permanent magnetic field sources for magnetocaloric heat pumps," *J Magn Magn Mater*, vol. 584, Oct. 2023, doi: 10.1016/j.jmmm.2023.171121.

[75] U. Tomc, S. Nosan, K. Klinar, and A. Kitanovski, "Towards powerful magnetocaloric devices with static electro-permanent magnets," *J Adv Res*, vol. 45, pp. 157–181, Mar. 2023, doi: 10.1016/j.jare.2022.05.001.

[76] D. J. Silva, A. M. Pereira, J. O. Ventura, J. P. Araújo, and J. C. R. E. Oliveira, "Thermal switching requirements for solid state magnetic refrigeration," *J Magn Magn Mater*, vol. 533, Sep. 2021, doi: 10.1016/j.jmmm.2021.167979.

[77] C. M. Hung *et al.*, "MnP Films with Desired Magnetic, Magnetocaloric, and Thermoelectric Properties for a Perspective Magneto-Thermo-Electric Cooling Device," *Physica Status Solidi (A) Applications and Materials Science*, vol. 219, no. 3, Feb. 2022, doi: 10.1002/pssa.202100367.

[78] J. M. D. Coey, "Magnetism an magnetic materials," Cambridge University Press, Ed., 2009, ch. 2.5.4, pp. 53–59.

[79] Song Y., Leighton C., and James D. J., "Thermodynamics and energy conversion in Heusler alloys," in *Heusler Alloys Properties, Growth, Applications*, 2016, ch. 11, pp. 269–291. [Online]. Available: http://www.springer.com/series/856

[80] A. Kitanovski, J. Tušek, U. Tomc, U. Plaznik, M. Ožbolt, and A. Poredoš, "Magnetocaloric Energy Conversion From Theory to Applications," in *Green Energy and Technology*, Springer, Ed., 2015, ch. 1, pp. 1–21. [Online]. Available: http://www.springer.com/series/8059

[81] R. A. Kishore and S. Priya, "A review on design and performance of thermomagnetic devices," 2018, *Elsevier Ltd*. doi: 10.1016/j.rser.2017.07.035.

[82] T. Christiaanse and E. Brück, "Proof-of-Concept Static Thermomagnetic Generator Experimental Device," *Metallurgical and Materials Transactions E*, vol. 1, no. 1, pp. 36–40, Mar. 2014, doi: 10.1007/s40553-014-0006-9.

[83] N. Tesla, "Thermomagnetic motor," US396121A, 1889

[84] Edison T. A., "Pyromagnetic motor," US380100A, 1888

[85] Tesla N., "Pyromagnetic electric generator," US428057A, 1890

[86] Edison T. A., "Pyromagnetic generator," US476983A, 1892

[87] V. Srivastava, Y. Song, K. Bhatti, and R. D. James, "The direct conversion of heat to electricity using multiferroic alloys," *Adv Energy Mater*, vol. 1, no. 1, pp. 97–104, Jan. 2011, doi: 10.1002/aenm.201000048.

[88] A. Waske *et al.*, "Energy harvesting near room temperature using a thermomagnetic generator with a pretzel-like magnetic flux topology," *Nat Energy*, vol. 4, no. 1, pp. 68–74, Jan. 2019, doi: 10.1038/s41560-018-0306-x.

[89] M. Gueltig *et al.*, "High-Performance Thermomagnetic Generators Based on Heusler Alloy Films," *Adv Energy Mater*, vol. 7, no. 5, Mar. 2017, doi: 10.1002/aenm.201601879.

[90] J. Chun, H. C. Song, M. G. Kang, H. B. Kang, R. A. Kishore, and S. Priya, "Thermo-Magneto-Electric Generator Arrays for Active Heat Recovery System," *Sci Rep*, vol. 7, Feb. 2017, doi: 10.1038/srep41383.

[91] R. A. Kishore *et al.*, "Energy scavenging from ultra-low temperature gradients," *Energy Environ Sci*, vol. 12, no. 3, pp. 1008–1018, Mar. 2019, doi: 10.1039/c8ee03084g.

[92] Vida N., Wymann D., and Brechbühler J., "Swiss Blue Energy AG," http://swiss-blue-energy.com/en/company.html.

[93] S. Glöser, L. Tercero Espinoza, C. Gandenberger, and M. Faulstich, "Raw material criticality in the context of classical risk assessment," *Resources Policy*, vol. 44, pp. 35–46, Jun. 2015, doi: 10.1016/j.resourpol.2014.12.003.

[94] C. Felser, G. H. Fecher, and B. Balke, "Spintronics: A challenge for materials science and solid-state chemistry," 2007. doi: 10.1002/anie.200601815.

[95] P. G. Van Engen, K. H. J. Buschow, and M. Erman, "Magnetic properties and magneto-optical spectroscopy of heusler alloys based on transition metals and Sn," *J Magn Magn Mater*, vol. 30, pp. 374–382, 1983, doi: 10.1016/0304-8853(83)90079-3.

[96] R. Kainuma *et al.*, "Magnetic-field-induced shape recovery by reverse phase transformation," *Nature*, vol. 439, no. 7079, pp. 957–960, Feb. 2006, doi: 10.1038/nature04493.

[97] T. Krenke *et al.*, "Inverse magnetocaloric effect in ferromagnetic Ni-Mn-Sn alloys," *Nat Mater*, vol. 4, no. 6, pp. 450–454, 2005, doi: 10.1038/nmat1395.

[98] S. Wurmehl, G. H. Fecher, H. C. Kandpal, V. Ksenofontov, C. Felser, and H. J. Lin, "Investigation of Co2FeSi: The Heusler compound with highest Curie temperature and magnetic moment," *Appl Phys Lett*, vol. 88, no. 3, pp. 1–3, 2006, doi: 10.1063/1.2166205.

[99] W. Wang *et al.*, "Coherent tunneling and giant tunneling magnetoresistance in Co2 FeAl/MgO/CoFe magnetic tunneling junctions," *Phys Rev B Condens Matter Mater Phys*, vol. 81, no. 14, Apr. 2010, doi: 10.1103/PhysRevB.81.140402.

[100] Planes A., Mañosa L., and Acet M., "Magnetocaloric effect and its relation to shape-memory properties in ferromagnetic Heusler alloys," *Journal of Physics: Condensed Matter*, vol. 21, no. 233201, 2009, doi: 10.1088/0953-8984/21/23/233201.

[101] J. Liu, T. Gottschall, K. P. Skokov, J. D. Moore, and O. Gutfleisch, "Giant magnetocaloric effect driven by structural transitions," *Nat Mater*, vol. 11, no. 7, pp. 620–626, 2012, doi: 10.1038/nmat3334.

[102] F. Orlandi, S. Fabbrici, F. Albertini, P. Manuel, D. D. Khalyavin, and L. Righi, "Long-range antiferromagnetic interactions in Ni-Co-Mn-Ga metamagnetic Heusler alloys: A two-step ordering studied by neutron diffraction," *Phys Rev B*, vol. 94, no. 14, Oct. 2016, doi: 10.1103/PhysRevB.94.140409.

[103] Ullakko K., Huang J. K., Kokorin V. V., and O'Handley R. C., "Magnetically controlled shape memory effect in Ni2MnGa intermetallics," *Scr Mater*, vol. 36, no. 10, pp. 1133–1138, 1997, doi: 10.1016/S1359-6462(96)00483-6.

[104] T. Krenke *et al.*, "Magnetic superelasticity and inverse magnetocaloric effect in Ni-Mn-In," *Phys Rev B Condens Matter Mater Phys*, vol. 75, no. 10, Mar. 2007, doi: 10.1103/PhysRevB.75.104414.

[105] L. Mañosa *et al.*, "Giant solid-state barocaloric effect in the Ni-Mn-In magnetic shape-memory alloy," *Nat Mater*, vol. 9, no. 6, pp. 478–481, 2010, doi: 10.1038/nmat2731.

[106] F. Albertini, M. Solzi, A. Paoluzi, and L. Righi, "Magnetocaloric properties and magnetic anisotropy by tailoring phase transitions in NiMnGa alloys," *Materials Science Forum*, vol. 583, pp. 169–196, 2008, doi: 10.4028/www.scientific.net/msf.583.169.

[107] S. Aksoy *et al.*, "Tailoring magnetic and magnetocaloric properties of martensitic transitions in ferromagnetic Heusler alloys," *Appl Phys Lett*, vol. 91, no. 24, 2007, doi: 10.1063/1.2825283.

[108] S. Fabbrici *et al.*, "Magnetocaloric properties at the austenitic Curie transition in Cu and Fe substituted Ni-Mn-In Heusler compounds," *J Alloys Compd*, vol. 899, Apr. 2022, doi: 10.1016/j.jallcom.2021.163249.

[109] I. Titov *et al.*, "Hysteresis effects in the inverse magnetocaloric effect in martensitic Ni-Mn-In and Ni-Mn-Sn," *J Appl Phys*, vol. 112, no. 7, Oct. 2012, doi: 10.1063/1.4757425.

[110] S. Fähler, "Caloric Effects in Ferroic Materials: New Concepts for Cooling," Aug. 01, 2018, *Wiley-VCH Verlag*. doi: 10.1002/ente.201800201.

[111] J. Cui *et al.*, "Combinatorial search of thermoelastic shape-memory alloys with extremely small hysteresis width," *Nat Mater*, vol. 5, no. 4, pp. 286–290, Apr. 2006, doi: 10.1038/nmat1593.

[112] Z. Zhang, R. D. James, and S. Müller, "Energy barriers and hysteresis in martensitic phase transformations," *Acta Mater*, vol. 57, no. 15, pp. 4332–4352, Sep. 2009, doi: 10.1016/j.actamat.2009.05.034.

[113] S. Kaufmann *et al.*, "Modulated martensite: Why it forms and why it deforms easily," *New J Phys*, vol. 13, May 2011, doi: 10.1088/1367-2630/13/5/053029.

[114] A. A. Mendonça *et al.*, "Experimentally correlating thermal hysteresis and phase compatibility in multifunctional Heusler alloys," *Phys Rev Mater*, vol. 4, no. 11, Nov. 2020, doi: 10.1103/PhysRevMaterials.4.114403.

[115] O. Gutfleisch *et al.*, "Mastering hysteresis in magnetocaloric materials," *Philosophical Transactions of the Royal Society A: Mathematical, Physical and Engineering Sciences*, vol. 374, no. 2074, Aug. 2016, doi: 10.1098/rsta.2015.0308.

[116] T. Gottschall, K. P. Skokov, B. Frincu, and O. Gutfleisch, "Large reversible magnetocaloric effect in Ni-Mn-In-Co," *Appl Phys Lett*, vol. 106, no. 2, Jan. 2015, doi: 10.1063/1.4905371.

[117] T. Gottschall, E. Stern-Taulats, L. Mañosa, A. Planes, K. P. Skokov, and O. Gutfleisch, "Reversibility of minor hysteresis loops in magnetocaloric Heusler alloys," *Appl Phys Lett*, vol. 110, no. 22, May 2017, doi: 10.1063/1.4984797.

[118] T. Kanomata *et al.*, "Magnetic and crystallographic properties of shape memory alloys Ni 2Mn1+xSn1-x," *Materials Science Forum*, vol. 583, pp. 119–129, 2008, doi: 10.4028/www.scientific.net/msf.583.119.

[119] Q. F. He, Z. Y. Ding, Y. F. Ye, and Y. Yang, "Design of High-Entropy Alloy: A Perspective from Nonideal Mixing," Nov. 01, 2017, *Minerals, Metals and Materials Society*. doi: 10.1007/s11837-017-2452-1.

[120] X. Wang, W. Guo, and Y. Fu, "High-entropy alloys: Emerging materials for advanced functional applications," Jan. 14, 2021, *Royal Society of Chemistry*. doi: 10.1039/d0ta09601f.

[121] J. Y. Law and V. Franco, "Review on magnetocaloric high-entropy alloys: Design and analysis methods," Jan. 14, 2023, *Springer Nature*. doi: 10.1557/s43578-022-00712-0.

[122] M. Acet, "Inducing strong magnetism in Cr20Mn20Fe20Co20Ni20 high-entropy alloys by exploiting its anti-Invar property," *AIP Adv*, vol. 9, no. 9, Sep. 2019, doi: 10.1063/1.5120251.

[123] C. Chen *et al.*, "A novel ultrafine-grained high entropy alloy with excellent combination of mechanical and soft magnetic properties," *J Magn Magn Mater*, vol. 502, May 2020, doi: 10.1016/j.jmmm.2020.166513.

[124] S. M. Na, P. K. Lambert, H. Kim, J. Paglione, and N. J. Jones, "Thermomagnetic properties and magnetocaloric effect of FeCoNiCrAl-type high-entropy alloys," *AIP Adv*, vol. 9, no. 3, Mar. 2019, doi: 10.1063/1.5079394.

[125] D. D. Belyea, M. S. Lucas, E. Michel, J. Horwath, and C. W. Miller, "Tunable magnetocaloric effect in transition metal alloys," *Sci Rep*, vol. 5, Oct. 2015, doi: 10.1038/srep15755.

[126] K. Sarlar, A. Tekgul, and I. Kucuk, "Magnetocaloric properties of rare-earth-free Mn27Cr7Ni33Ge25Si8 High-Entropy Alloy," *IEEE Magn Lett*, vol. 10, 2019, doi: 10.1109/LMAG.2019.2955667.

[127] J. Y. Law and V. Franco, "Pushing the limits of magnetocaloric high-entropy alloys," *APL Mater*, vol. 9, no. 8, Aug. 2021, doi: 10.1063/5.0058388.

[128] L. Han *et al.*, "Multifunctional high-entropy materials," 2024, *Nature Research*. doi: 10.1038/s41578-024-00720-y.

[129] M. S. Lucas *et al.*, "Magnetic and vibrational properties of high-entropy alloys," in *Journal of Applied Physics*, Apr. 2011. doi: 10.1063/1.3538936.

[130] M. S. Lucas *et al.*, "Thermomagnetic analysis of FeCoCrxNi alloys: Magnetic entropy of high-entropy alloys," in *Journal of Applied Physics*, May 2013. doi: 10.1063/1.4798340.

[131] S. M. Na, J. H. Yoo, P. K. Lambert, and N. J. Jones, "Room-temperature ferromagnetic transitions and the temperature dependence of magnetic behaviors in FeCoNiCr-based high-entropy alloys," *AIP Adv*, vol. 8, no. 5, May 2018, doi: 10.1063/1.5007073.

[132] M. Kurniawan, A. Perrin, P. Xu, V. Keylin, and M. McHenry, "Curie Temperature Engineering in High Entropy Alloys for Magnetocaloric Applications," *IEEE Magn Lett*, vol. 7, 2016, doi: 10.1109/LMAG.2016.2592462.

[133] S. Vorobiov *et al.*, "Magnetic properties, magnetoresistive, and magnetocaloric effects of AlCrFeCoNiCu thin-film high-entropy alloys prepared by the co-evaporation technique," *Appl Phys A Mater Sci Process*, vol. 127, no. 3, Mar. 2021, doi: 10.1007/s00339-020-04145-6.

[134] J. Y. Law *et al.*, "MnFeNiGeSi high-entropy alloy with large magnetocaloric effect," *J Alloys Compd*, vol. 855, Feb. 2021, doi: 10.1016/j.jallcom.2020.157424.

[135] Z. Dong *et al.*, "MnxCr0.3Fe0.5Co0.2Ni0.5Al0.3 high entropy alloys for magnetocaloric refrigeration near room temperature," Jul. 20, 2021, *Chinese Society of Metals*. doi: 10.1016/j.jmst.2020.10.071.

[136] K. Sarlar, A. Tekgül, and I. Kucuk, "Magnetocaloric properties in a FeNiGaMnSi high entropy alloy," *Current Applied Physics*, vol. 20, no. 1, pp. 18–22, Jan. 2020, doi: 10.1016/j.cap.2019.09.019.

[137] A. K. Tyagi and R. S. Ningthoujam Editors, "Indian Institute of Metals Series Handbook on Synthesis Strategies for Advanced Materials Volume-I: Techniques and Fundamentals." [Online]. Available: https://link.springer.com/bookseries/15453

[138] J. A. Sillero, D. Ortega, E. Muñoz-Serrano, and E. Casado, "An experimental study of thoriated tungsten cathodes operating at different current intensities in an atmospheric-pressure plasma torch," *J Phys D Appl Phys*, no. 18, p. 185204, 2010, doi: 10.1088/0022-3727/43/18/185204ï.

[139] P. Entel *et al.*, "Properties and Decomposition of Heusler Alloys," *Energy Technology*, vol. 6, no. 8, pp. 1478–1490, Aug. 2018, doi: 10.1002/ente.201800256.

[140] S. Venkatesan *et al.*, "Enhanced Refrigeration Capacity of Rare-Earth-Free Ni-Co-Mn-In-Si Heusler Alloys for Magnetic Refrigerants," *ECS Journal of Solid State Science and Technology*, vol. 10, no. 9, p. 091009, Sep. 2021, doi: 10.1149/2162-8777/ac2323.

[141] A. Taubel *et al.*, "Tailoring magnetocaloric effect in all-d-metal Ni-Co-Mn-Ti Heusler alloys: a combined experimental and theoretical study," *Acta Mater*, vol. 201, pp. 425–434, Dec. 2020, doi: 10.1016/j.actamat.2020.10.013.

[142] M. Gong *et al.*, "Effect of Heat Treatment Temperature on Microstructure and Properties of FeCoNiCuTi High–Entropy Alloy," *Transactions of the Indian Institute of Metals*, vol. 75, no. 8, pp. 1951–1956, Aug. 2022, doi: 10.1007/s12666-022-02665-8.

[143] G. Cavazzini *et al.*, "Multifunctional Ni-Mn-Ga and Ni-Mn-Cu-Ga Heusler particles towards the nanoscale by ball-milling technique," *J Alloys Compd*, vol. 872, Aug. 2021, doi: 10.1016/j.jallcom.2021.159747.

[144] C. Coppi *et al.*, "Graphene-Based Magnetocaloric Composites for Energy Conversion," *Adv Eng Mater*, vol. 25, no. 1, Jan. 2023, doi: 10.1002/adem.202200811.

[145] Díaz-García *et al.*, "Novel procedure for laboratory scale production of composite functional filaments for additive manufacturing," *Mater Today Commun*, vol. 24, Sep. 2020, doi: 10.1016/j.mtcomm.2020.101049.

[146] P. Laurent *et al.*, "An ac susceptometer for the characterization of large, bulk superconducting samples," *Meas Sci Technol*, vol. 19, no. 8, Aug. 2008, doi: 10.1088/0957-0233/19/8/085705.

[147] U. Geological Survey, "Mineral Commodity Summaries 2024," 2024. doi: https://doi.org/10.3133/mcs2024.

[148] W. M. Haynes, David R. Lide, and Thomas J. Bruno, Eds., "Abundance of Elements in the Earth's Crust and in the Sea," in *CRC Handbook of Chemistry and Physics*, 95th ed., 2015, ch. 14, p. 19.

[149] G. Cavazzini *et al.*, "Tuning the magnetic and magnetocaloric properties of austenitic Ni-Mn-(In,Sn)Heuslers," *Scr Mater*, vol. 170, pp. 48–51, Sep. 2019, doi: 10.1016/j.scriptamat.2019.05.027.

[150] T. Kanomata *et al.*, "Magnetic moment of cu-modified Ni2MnGa magnetic shape memory alloys," *Metals (Basel)*, vol. 3, no. 1, pp. 114–122, Mar. 2013, doi: 10.3390/met3010114.

[151] H. F. Wang, J. M. Wang, C. B. Jiang, and H. Bin Xu, "Phase transition and mechanical properties of Ni30Cu20Mn37+xGa13−x (x = 0–4.5) alloys," *Rare Metals*, vol. 33, no. 5, pp. 547–551, Oct. 2014, doi: 10.1007/s12598-013-0103-4.

[152] C. Seguí and E. Cesari, "Ordering mechanism and kinetics in Ni2Mn1−xCuxGa ferromagnetic shape memory alloys," *J Alloys Compd*, vol. 887, Dec. 2021, doi: 10.1016/j.jallcom.2021.161302.

[153] C. Seguí, "Kinetics of Reordering in Quenched Ni2Mn0.8Cu0.2Ga Ferromagnetic Shape Memory Alloys," *Metals (Basel)*, vol. 12, no. 5, May 2022, doi: 10.3390/met12050738.

[154] H. Zhang *et al.*, "Martensite transformation and magnetic properties of Fe-doped Ni-Mn-Sn alloys with dual phases," *J Alloys Compd*, vol. 689, pp. 481–488, 2016, doi: 10.1016/j.jallcom.2016.07.282.

[155] C. Tan, Z. Tai, K. Zhang, X. Tian, and W. Cai, "Simultaneous enhancement of magnetic and mechanical properties in Ni-Mn-Sn alloy by Fe doping," *Sci Rep*, vol. 7, Feb. 2017, doi: 10.1038/srep43387.

[156] P. Lázpita, M. Sasmaz, J. M. Barandiarán, and V. A. Chernenko, "Effect of Fe doping and magnetic field on martensitic transformation of Mn-Ni(Fe)-Sn metamagnetic shape memory alloys," *Acta Mater*, vol. 155, pp. 95–103, Aug. 2018, doi: 10.1016/j.actamat.2018.05.052.

[157] T. Malkoç, M. S. Kanca, E. Işık, and M. Kök, "Impact of electron concentration on the transformation temperature and important physical properties of NiMnSnFe ferromagnetic shape memory alloys," *MRS Commun*, vol. 13, no. 3, pp. 500–506, Jun. 2023, doi: 10.1557/s43579-023-00363-0.

[158] M. F. Toney, C. Tsang, and J. Kent Howard, "Thermal annealing study of exchange-biased NiFe-FeMn films," *J Appl Phys*, vol. 70, no. 10, pp. 6227–6229, 1991, doi: 10.1063/1.350003.

[159] T. Kaneko, H. Yoshida, S. Abe, and K. Kamigaki, "Pressure effect on the Curie point of the Heusler alloys Ni2MnSn and Ni2MnSb," *J Appl Phys*, vol. 52, no. 3, pp. 2046–2048, 1981, doi: 10.1063/1.329610.

[160] J. H. Chen *et al.*, "The effects of Cu-substitution and high-pressure synthesis on phase transitions in Ni2MnGa Heusler alloys," *J Alloys Compd*, vol. 900, Apr. 2022, doi: 10.1016/j.jallcom.2021.163480.

[161] C. Taake, T. Samanta, and L. Caron, "Field-sensitivity and reversibility of the inverse magnetocaloric effect at martensitic transformations," *Appl Phys Lett*, vol. 124, no. 5, Jan. 2024, doi: 10.1063/5.0185552.

[162] T. Krenke, M. Acet, E. F. Wassermann, X. Moya, L. Mañosa, and A. Planes, "Martensitic transitions and the nature of ferromagnetism in the austenitic and martensitic states of Ni-Mn-Sn alloys," *Phys Rev B Condens Matter Mater Phys*, vol. 72, no. 1, 2005, doi: 10.1103/PhysRevB.72.014412.

[163] H. Zheng, W. Wang, S. Xue, Q. Zhai, J. Frenzel, and Z. Luo, "Composition-dependent crystal structure and martensitic transformation in Heusler Ni-Mn-Sn alloys," *Acta Mater*, vol. 61, no. 12, pp. 4648–4656, Jul. 2013, doi: 10.1016/j.actamat.2013.04.035.

[164] X. Liu *et al.*, "High-performance thermomagnetic generator controlled by a magnetocaloric switch," *Nat Commun*, vol. 14, no. 1, Dec. 2023, doi: 10.1038/s41467-023-40634-x.

[165] A. Smith, C. R. H. Bahl, R. Bjork, K. Engelbrecht, K. K. Nielsen, and N. Pryds, "Materials challenges for high performance magnetocaloric refrigeration devices," Nov. 2012. doi: 10.1002/aenm.201200167.

[166] Á. Díaz-García, J. Y. Law, Ł. Żrodowski, B. Morończyk, R. Wróblewski, and V. Franco, "Polymer-based filaments with embedded magnetocaloric Ni-Mn-Ga Heusler alloy particles for additive manufacturing," *Polym Compos*, vol. 45, no. 6, pp. 5333–5345, Apr. 2024, doi: 10.1002/pc.28130.

[167] T. D. Ngo, A. Kashani, G. Imbalzano, K. T. Q. Nguyen, and D. Hui, "Additive manufacturing (3D printing): A review of materials, methods, applications and challenges," Jun. 15, 2018, *Elsevier Ltd*. doi: 10.1016/j.compositesb.2018.02.012.

[168] M. Srivastava, S. Rathee, V. Patel, A. Kumar, and P. G. Koppad, "A review of various materials for additive manufacturing: Recent trends and processing issues," Nov. 01, 2022, *Elsevier Editora Ltda*. doi: 10.1016/j.jmrt.2022.10.015.

[169] X. Wang, M. Jiang, Z. Zhou, J. Gou, and D. Hui, "3D printing of polymer matrix composites: A review and prospective," Feb. 01, 2017, *Elsevier Ltd*. doi: 10.1016/j.compositesb.2016.11.034.

[170] M. Hemath, S. Mavinkere Rangappa, V. Kushvaha, H. N. Dhakal, and S. Siengchin, "A comprehensive review on mechanical, electromagnetic radiation shielding, and thermal conductivity of fibers/inorganic fillers reinforced hybrid polymer composites," Oct. 01, 2020, *John Wiley and Sons Inc*. doi: 10.1002/pc.25703.

[171] J. Kumar and S. Negi, "Development of 3D printable cenosphere-reinforced polyethylene terephthalate glycol (PETG) filaments for lightweight structural applications," *Polym Compos*, vol. 44, no. 10, pp. 7030–7039, Oct. 2023, doi: 10.1002/pc.27616.

[172] G. Cakmak, "Effect of Heat Treatment on the Microstructure, Phase Distribution, and Mechanical Properties of AlCoCuFeMnNi High Entropy Alloy," *Advances in Materials Science and Engineering*, vol. 2017, 2017, doi: 10.1155/2017/1950196.

[173] A. Munitz, L. Meshi, and M. J. Kaufman, "Heat treatments' effects on the microstructure and mechanical properties of an equiatomic Al-Cr-Fe-Mn-Ni high entropy alloy," *Materials Science and Engineering: A*, vol. 689, pp. 384–394, Mar. 2017, doi: 10.1016/j.msea.2017.02.072.

[174] Q. Huaizhi *et al.*, "Effect of heat treatment time on the microstructure and properties of FeCoNiCuTi high-entropy alloy," May 01, 2023, *Elsevier Editora Ltda*. doi: 10.1016/j.jmrt.2023.04.078.

[175] Toliyat A. H. and Kliman B. G., "Handbook of electric motors," in *Electrical an Computer Engineering, A Series of Reference Books and Textbooks*, Second Edition., Thurston M. O., Ed., 2004, ch. 2.3, pp. 58–77.

11 Acknowledgements

These past three years of Ph.D. research have been a defining section in my academic journey, contributing deeply to my professional development and personal growth. This milestone would not have had the same impact without the support and companionship of those who joined me along this challenging yet fulfilling path.

My heartfelt thanks extend to all members of the MatFun Group at IMEM-CNR in Parma (Dr. Franca Albertini, Dr. Simone Fabbrici, Dr. Francesca Casoli, Dr. Riccardo Cabassi, Dr. César de Julian Fernandez, Dr. Matteo Belli and Dr. Milad Takhsha Ghahfarokhi), who offered essential advice and technical assistance, helping me to develop a better understanding of experimental processes and scientific research.

A special thanks goes to Dr. Franca Albertini and Dr. Simone Fabbrici, who not only supervised my doctoral work as my advisors but also greatly contributed to my scientific growth. If, by the end of my Ph.D., my desire to continue in research is even stronger than before, I owe it to them and to their guidance.

I would also like to express my sincere thanks to Dr. Francesco Cugini (SMFI, Unipr) for his constant availability, support, and the invaluable knowledge he has shared since my undergraduate days to the present. I am grateful for the enriching scientific discussions and insights.

A special thanks goes to Professor Massimo Solzi (SMFI, Unipr), who was my supervisor during my master's degree and through whom I discovered a field of research that, even years later, continues to inspire my passion.

I am particularly grateful to Dr. Giovanna Trevisi (IMEM-CNR) for her ongoing and vital assistance with SEM analyses of the numerous powder samples prepared, and for her insightful explanations and suggestions that helped refine my research approach

I am deeply grateful to Dr. Victorino Franco and Dr. Jin Yan Law (University of Sevilla), who hosted me during my visit to the their laboratories, making me feel truly at home and sharing with me a different approach to research that greatly enriched me and that I will carry forward.